

**Pedro Tovar Braga**

**Time-Resolved Optical  
Spectroscopy for Laser Chirp  
Characterization and  
Self-Heterodyne generation of LFM  
and NLFM Microwave Pulses**

**DISSERTAÇÃO DE MESTRADO**

**DEPARTAMENTO DE ENGENHARIA ELÉTRICA**  
Programa de Pós-graduação em Engenharia  
Elétrica

Rio de Janeiro  
July 2018



**Pedro Tovar Braga**

**Time-Resolved Optical Spectroscopy for Laser  
Chirp Characterization and Self-Heterodyne  
generation of LFM and NLFM Microwave  
Pulses**

**Dissertação de Mestrado**

Dissertation presented to the Programa de Pós-graduação em Engenharia Elétrica da PUC-Rio in partial fulfillment of the requirements for the degree of Mestre em Engenharia Elétrica.

Advisor: Prof. Jean Pierre von der Weid

Rio de Janeiro  
July 2018



**Pedro Tovar Braga**

**Time-Resolved Optical Spectroscopy for Laser Chirp  
Characterization and Self-Heterodyne generation of LFM and  
NLFM Microwave Pulses**

Dissertation presented to the Programa de Pós-Graduação em Engenharia Elétrica of PUC-Rio in partial fulfillment of the requirements for the degree of Mestre em Engenharia Elétrica. Approved by the undersigned Examination Committee.

**Prof. Jean Pierre von der Weid**

Advisor

Centro de Estudos em Telecomunicações – PUC-Rio

**Prof. Luis Ernesto Ynoquio Herrera**

Departamento de Engenharia Elétrica – PUC-Rio

**Prof. Marbey Manhães Mosso**

Departamento de Engenharia Elétrica – PUC-Rio

**Prof. Ricardo Marques Ribeiro**

UFF

**Prof. Márcio da Silveira Carvalho**

Vice Dean of Graduate Studies

Centro Técnico Científico – PUC-Rio

Rio de Janeiro, July 24th, 2018

All rights reserved.

### **Pedro Tovar Braga**

Pedro Tovar Braga graduated from the Pontifícia Universidade Católica do Rio de Janeiro (Rio de Janeiro, Brasil) in Electrical Engineering with emphasis on Telecommunications. He is a member and active participant of the Photonics and Optoelectronics Laboratory of the Center for Telecommunication Studies at PUC-Rio.

#### Bibliographic data

Tovar Braga, Pedro

Time-Resolved Optical Spectroscopy for Laser Chirp Characterization and Self-Heterodyne generation of LFM and NLFM Microwave Pulses / Pedro Tovar Braga; advisor: Jean Pierre von der Weid. – Rio de Janeiro: PUC-Rio, Departamento de Engenharia Elétrica, 2018.

v., 89 f: il. color. ; 30 cm

Dissertação (mestrado) - Pontifícia Universidade Católica do Rio de Janeiro, Departamento de Engenharia Elétrica.

Inclui bibliografia

1. Engenharia Elétrica – Teses. 2. Microonda-Fotônica;. 3. Modulação Não-Linear em Frequência;. 4. Pulsos de RF apodizados;. 5. Auto-Heteródino;. 6. Produto Largura de Banda-Tempo;. 7. Radar de Banda Ultra Larga.. I. von der Weid, Jean Pierre. II. Pontifícia Universidade Católica do Rio de Janeiro. Departamento de Engenharia Elétrica. III. Título.

CDD: 621.3

## Acknowledgments

I would like to thank Julia Duarte, my constant source of inspiration for everything I do.

To my advisor Jean Pierre von der Weid, for the teachings and scientific discussions that kindles my curiosity on a regular basis.

To my colleagues and friends of PUC–Rio, specially L. E. Y. Herrera and Felipe Calliari, who were always there to help me on the minimal details.

To Gustavo Amaral, for the friendship, teaching and for bringing me back to the inspiring world of research.

To my mother, for her love and endless support, and to my brother, for being my life example of character. Without them, this work would not have been possible.

To all my family and friends, who directly or indirectly contributed to this work.

I would also like to thank to the brazilian agency CAPES for the financial support.

## Abstract

Tovar Braga, Pedro; von der Weid, Jean Pierre (Advisor). **Time-Resolved Optical Spectroscopy for Laser Chirp Characterization and Self-Heterodyne generation of LFM and NLFM Microwave Pulses**. Rio de Janeiro, 2018. 89p. Dissertação de Mestrado – Departamento de Engenharia Elétrica, Pontifícia Universidade Católica do Rio de Janeiro.

This work reports the photonic generation of both linear and non-linear frequency modulation (LFM and NLFM) microwave pulses through a self-heterodyne scheme. By using low-frequency electronics to drive a distributed feedback laser diode, optical chirping is generated predominantly by thermal effect. Combining laser chirping and self-heterodyning, LFM pulses with high time-bandwidth product (TBWP) were achieved. A different approach is required for generation of NLFM microwave pulses. First, for characterization of the laser diode chirp, it is introduced a technique named Time-Resolved Optical Spectroscopy. Then, by using a step-shaped current stimulus, the laser chirp transfer function  $H(s)$  was obtained. With knowledge on  $H(s)$ , a numerical simulation produced the suitable current stimulus  $i(t)$  needed to generate NLFM microwave pulses through self-heterodyning. Experimental results agreed with the numerical simulations.

## Keywords

Microwave-Photonics; Non-Linear Frequency Modulation; RF pulse apodization; Self-Heterodyne; Time-Bandwidth Product; Ultra-Wideband Radar.

## Resumo

Tovar Braga, Pedro; von der Weid, Jean Pierre (Orientador). **Espectroscopia Óptica Resolvida no Tempo para Caracterização do Chirp de Lasers e geração Auto-Heteródina de Pulsos de Microondas LFM e NLFM**. Rio de Janeiro, 2018. 89p. Dissertação de Mestrado – Departamento de Engenharia Elétrica, Pontifícia Universidade Católica do Rio de Janeiro.

Este trabalho apresenta a geração de pulsos de microondas linearmente e não-linearmente modulados em frequência (LFM e NLFM) através da técnica fotônica de auto-heterodinagem. Ao utilizar eletrônica de baixa frequência para modular um diodo laser de feedback distribuído, a variação da portadora óptica no tempo (chirp) é observada, o que é causado predominantemente por efeito térmico. Este efeito, combinado com batimento auto-heteródino, foi capaz de produzir pulsos LFM com alto produto largura de banda-tempo (TBWP). Uma outra abordagem é necessária para geração de pulsos NLFM. Primeiro, é introduzida a técnica Espectroscopia Óptica Resolvida no Tempo para caracterização do chirp de um diodo laser. Em seguida, um estímulo de corrente em formato de função degrau é aplicado ao diodo laser para aquisição da função de transferência de seu chirp,  $H(s)$ . Com a posse de  $H(s)$ , uma simulação numérica foi usada para descobrir o estímulo necessário de corrente  $i(t)$  para obtenção de pulsos de microondas NLFM através da técnica de auto-heterodinagem. Os resultados experimentais coincidem com a simulação.

## Palavras-chave

Microonda-Fotônica; Modulação Não-Linear em Frequência; Pulsos de RF apodizados; Auto-Heteródino; Produto Largura de Banda-Tempo; Radar de Banda Ultra Larga.

## Table of contents

1	Introduction	15
2	Theoretical Review	20
2.1	Radar Waveforms	20
2.1.1	Matched Filter	21
2.1.2	Range resolution and SNR	23
2.1.3	Pulse Compression and LFM	24
2.1.4	NLFM	30
2.2	Optical Phenomena	33
2.2.1	Lasers and Optical Chirp	34
2.2.2	Thermal Chirp	36
2.2.3	Dynamic Chirp	38
2.2.4	Semiconductor Optical Amplifiers	39
2.2.5	Optical Interference	40
2.2.6	Interferometers	42
2.3	Generation of Chirped Microwave Pulses	43
2.3.1	Review of Photonic techniques for Microwave Generation	44
2.3.2	RF Linear Chirp	46
2.3.3	The Self-Heterodyning technique for microwave generation	47
2.3.4	Tradeoff and optimization of bandwidth and TBWP	50
3	Photonic Generation of LFM pulses	52
3.1	Experimental Setup	52
3.2	Spectrum-scanning chirp measurement technique	55
3.3	Experimental Results	57
3.3.1	Electrical Harmonic Distortions and Phase Noise	57
3.3.2	Optimization of TBWP and BW	59
3.3.3	Generation and Tuning of Microwave Pulses	60
3.3.4	RF Chirp Linearization	63
4	Photonic Generation of NLFM pulses	66
4.1	Experimental Setup	67
4.2	Time-Resolved Optical Spectroscopy	68
4.3	Laser chirp modelling	71
4.4	System Simulation	73
4.5	Experimental results	79
5	Conclusions	82
	Bibliography	84

## List of figures

Figure 1.1	Number of publications (article, conference paper, article review, conference review and article in press) with the words "photonic", "generation" and "microwave" present in the title, abstract or key-words (source: <i>www.scopus.com</i> ).	16
Figure 2.1	Transmitted ( $s(t)$ ) and detected ( $r(t)$ ) sinusoidal pulses in a radar system at two different stages: before (top) and after (bottom) the matched filter.	23
Figure 2.2	Linear Frequency Modulation (LFM) pulse for a central frequency $f_0 = 5$ GHz, bandwidth $\Delta f = 10$ GHz, constant amplitude of 1 V, and time duration $T = 5$ ns.	26
Figure 2.3	Transmitted LFM and compressed pulses for a central frequency $f_0 = 3$ MHz, bandwidth $\Delta f = 2$ MHz, constant amplitude of 1 V, time duration $T = 2 \mu\text{s}$ and a round-trip time $T_M = 10 \mu\text{s}$ .	27
Figure 2.4	Output of matched filter (absolute value) for an LFM transmitted waveform. (a) TBWP = 10. (b) TBWP = 100. The dotted line is the output envelope of a matched filter for a simple sinusoidal pulse of the same duration [1].	29
Figure 2.5	Neighbouring target masked by the sidelobes of the main target [1].	30
Figure 2.6	Expanded view of the central portion of Fig. 2.4b [1].	31
Figure 2.7	PSLR comparison between LFM and NLFM microwave pulses [2].	32
Figure 2.8	Typical shape of the frequency chirp (a) and energy spectral density (b) of an NLFM pulse [3].	33
Figure 2.9	Cause and effect diagram of the main components responsible for the overall optical chirp phenomenon: thermal and dynamic chirp.	36
Figure 2.10	Measured output frequency of a DBF-LD for different input bias currents.	37
Figure 2.11	Thermal chirp transitory simulation of a DFB-LD for four different modulation frequencies.	38
Figure 2.12	Simulated modulation response of a semiconductor laser to 500 ps rectangular pulses. Solid curve shows the pulse shape and the dashed curve shows the dynamic chirp imposed on the pulse [4].	39
Figure 2.13	Schematic of a Semiconductor Optical Amplifier.	40
Figure 2.14	(a) Mach-Zehnder interferometer, (b) Michelson interferometer and (c) Sagnac interferometer. An input wave $U_0$ shown in red is split into two waves $U_1$ and $U_2$ , shown separately in dark and light red for ease of visualization, but are actually congruent [5].	43
Figure 2.15	Replicas of optical frequency modulated pulses.	50

Figure 3.1	Experimental setup. Picture of back-to-back configuration (top) and diagram (bottom).	53
Figure 3.2	AFG1 and AFG2 waveforms for full bandwidth microwave pulse generation (a) and spectrum-scanning chirp measurement (b).	56
Figure 3.3	Harmonic Distortion measurement of the RF microwave pulse.	58
Figure 3.4	DFB-LD linewidth (left) and the inset detail (right). Black curve corresponds to the effective measurement; red curve to the Lorentzian fit.	59
Figure 3.5	The BW (left) and TBWP (right) of the output beating signal as a function of the delay $\tau$ normalized by the time duration $W$ of the modulating current waveform ( $\tau/W$ ).	60
Figure 3.6	Chirped microwave signals in different radar bands. The band is selected by changing the chop time $W_C$ and delay $\delta$ .	61
Figure 3.7	Microwave waveform signal (2–3.5 GHz) generated for a short $W_C$ .	62
Figure 3.8	Photonic generated microwave spectrum corresponding to 74000 of TBWP.	63
Figure 3.9	Chirp measurement of a non-linearized chirped microwave signal through spectrum-scanning technique before and after transmission along 41 km standard singlemode fiber.	64
Figure 3.10	Chirp measurement of a linearized chirped microwave signal through spectrum-scanning technique before and after transmission along 41 km standard singlemode fiber.	64
Figure 3.11	Linearized beating frequency chirp before (B2B) and after transmission along 25 and 41 km standard single-mode fiber.	65
Figure 4.1	The self-heterodyne experimental setup.	67
Figure 4.2	Optical spectrum-time scanning setup for Time-Resolved Optical Spectroscopy by using a High Resolution Optical Spectrum Analyzer.	68
Figure 4.3	Optical spectrum-time scanning acquisition for a step input current feeding a DFB-LD. Top panel: input current and chop windows; Bottom panel: normalized optical power measured at high-resolution optical spectrum analyzer.	69
Figure 4.4	DFB-LD Frequency response to a step modulation current. The in-set shows a detailed optical frequency shifts near the pulse step edge.	70
Figure 4.5	Comparison between the thermal chirp and the chirp measured at the end of a 100 $\mu$ s pulse with a repetition rate of 0.33 kHz.	71
Figure 4.6	Comparison between two instantaneous frequency drift originated from two different step input modulation currents: $\Delta i = 60$ mA (blue); $\Delta i = 30$ mA (red).	73

- Figure 4.7 Simulation results of the obtained current inputs (b) required for the parabolic optical chirp outputs (a). As the self-heterodyne beating ( $\tau = 1.5\mu\text{s}$ ) of parabolic optical chirp signals originates LFM microwave waveforms with chirp rate depending on the parabola slope, four chirp rates ( $\propto$  parabola slope) were analysed: 1, 2, 5 and 10 GHz/ $\mu\text{s}$ . 75
- Figure 4.8 Simulation results of the obtained current inputs (b) required for the linear optical chirp outputs (a). As the self-heterodyne beating ( $\tau = 1.5\mu\text{s}$ ) of linear optical chirp signals originates microwave tones, four microwave tones were analysed: 1, 2, 5 and 10 GHz. 76
- Figure 4.9 Simulation results for photonic generation of an apodized microwave pulse. First panel: input current variations above 20 mA. Second panel: output optical frequency in the two arms of an unbalanced interferometer. Third panel: frequency of the generated microwave. 78
- Figure 4.10 Measurement of the input modulation current with a repetition rate of 0.33 kHz. 79
- Figure 4.11 Photonic generated NLFM microwave pulses: (a) Microwave power spectrum; (b) Comparison between the simulated and measured time dependent frequency  $f_{RF}(t)$  of NLFM microwave pulses. 80

## List of tables

Table 1.1	Radar Bands	16
Table 3.1	Experimental Equipment	55

## List of Abbreviations

AFG – Arbitrary Function Generator  
B2B – Back-to-Back  
BW – Bandwidth  
CW – Continuous Wave  
DC – Direct Current  
DFB-LD – Distributed Feedback Laser Diode  
DST – Direct Space-to-Time  
ED – Electronic Driver  
EDFA – Erbium-Doped Fiber Amplifier  
ESA – Electrical Spectrum Analyzer  
FM – Frequency Modulation  
FPGA – Field Programmable Gate Array  
FWHM – Full Width Half Maximum  
FWM – Four-Wave Mixing  
GPIB – General Purpose Interface Bus  
HD – Harmonic Distortion  
HNLFM – Hybrid Non-Linear Frequency Modulation  
HR-OSA – High Resolution Optical Spectrum Analyzer  
IFM – Instantaneous Frequency Measurement  
LBS – Laser Bias Source  
LD – Laser Diode  
LFM – Linear Frequency Modulation  
LTI – Linear Time-Invariant  
MPD – Microwave Phase Discriminator  
MZI – Mach-Zehnder Interferometer  
MZM – Mach-Zehnder Modulator  
NLFM – Non-Linear Frequency Modulation  
PAT – Power Amplifier Transmitter  
PC – Polarization Controller  
PCR – Pulse Compression Ratio  
PD – Photodiode  
POT – Power Oscillator Transmitter  
PSLR – Peak-to-Sidelobe Ratio

RF – Radio Frequency  
SAW – Surface Acoustic Wave  
SG-DBR – Sampled-Grating Distributed Bragg Reflector  
SMF – Single Mode Fiber  
SNR – Signal-to-Noise Ratio  
SOA – Semiconductor Optical Amplifier  
SS-CMT – Spectrum-Scanning Chirp Measurement Technique  
SS-WTT – Spectral-Shaping and Wavelength-to-Time  
TBWP – Time-Bandwidth Product  
TW – Travelling-Wave  
VCO – Voltage Controlled Oscillators  
VOA – Variable Optical Attenuator

*Imagination is more important than knowledge. Knowledge is limited.*

**Albert Einstein.**

# 1 Introduction

The word *Microwave* is often a source of confusion among beginner students of telecommunication engineering. Although the name suggests that it refers to electromagnetic waves with wavelengths in the order of micrometers, its wavelengths are actually in the range of 1 mm to 1 m (300 GHz – 300 MHz). The purpose of the prefix "micro" was to differentiate this kind of waves from radio waves, as the former has a smaller wavelength than the latter. A wide range of applications is found for microwaves, to name a few: wireless communications, satellite and spacecraft communication, cancer treatment, remote sensing, particle accelerators, keyless entry systems, mechanical heating, cooking and radar systems.

Among the applications above, radar systems are of particular interest for this work. These systems operate in a portion of the microwave spectrum, ranging from 1 to 110 GHz (30 – 0.27 cm), where nine radar bands are defined - see table 1.1. To generate an electromagnetic wave in a radar band was a big challenge in the beginning of the twentieth century. In 1921, the invention of the Magnetron tube, by Albert Wallace Hull, emerged as a first efficient solution for the problem. The Magnetron tube is a microwave oscillator that, when keyed by a high power direct current (DC) pulse, produces microwave pulses suitable for radar systems. This type of transmitting system and others that use microwave tube technology were later called Power Oscillator Transmitters (POT).

Over the years, Power Amplifier Transmitters (PAT) have been taking the place of POTs. The transmitting pulse in PAT systems is produced by waveform generators based on solid-state technology, which permits generating predefined waveforms by setting the amplitude, frequency and phase of the microwave signals. However, as the microwave power plays an important role in radar systems, microwave tube technology continues to offer advantages over some solid-state technology waveform generators.

Despite the improved capacity that solid-state technology provides for microwave generation, due to the ever increasing demand of performance in radar systems, and to the limited speed of the currently available electronic circuits, other techniques were required for that task. Probably the most

Table 1.1: Radar Bands

Radar Band	Frequency range [GHz]	Wavelength range [cm]
L band	1 – 2	30 – 15
S band	2 – 4	15 – 7.5
C band	4 – 8	7.5 – 3.75
X band	8 – 12	3.75 – 2.5
Ku band	12 – 18	2.5 – 1.67
K band	18 – 27	1.67 – 1.11
Ka band	27 – 40	1.11 – 0.75
V band	40 – 75	0.75 – 0.4
W band	75 – 110	0.4 – 0.27

studied alternative for microwave generation in the recent years is through photonic techniques, which not only provides wide and high bandwidth, but also have the advantages of low loss, lightweight, and immunity to electromagnetic interference. To provide solid data of how much photonic techniques have been recently investigated for microwave generation, Fig. 1.1 brings the number of publications with the words "photonic", "generation" and "microwave" present in the publication title, abstract or key-words over the past 20 years - obtained through Scopus<sup>®</sup> database.

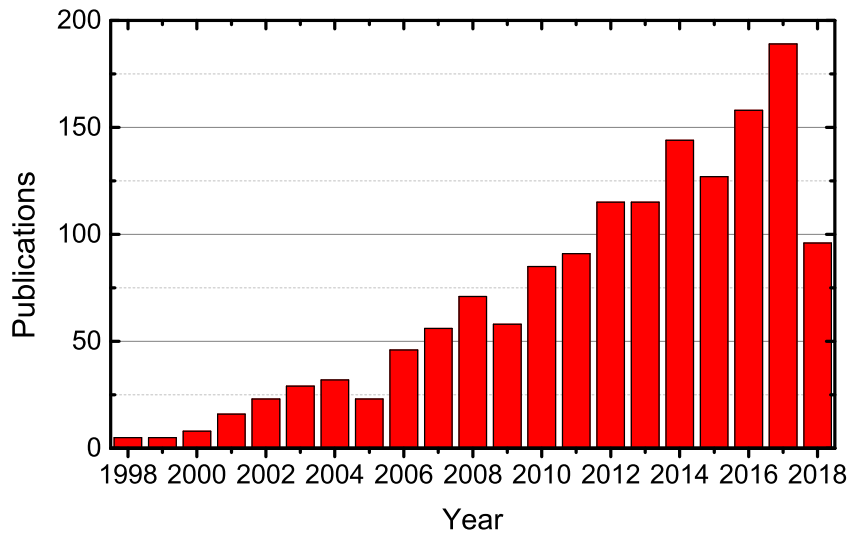


Figure 1.1: Number of publications (article, conference paper, article review, conference review and article in press) with the words "photonic", "generation" and "microwave" present in the title, abstract or key-words (source: *www.scopus.com*).

Among the search result of 1492 publications involving photonic generation of microwave signals, there is a lot of interest in the generation of a special

microwave waveform that improves radars' resolution range. This special microwave waveform is known as linearly chirped microwave pulses, or linear frequency modulation (LFM) pulses. Between the several photonic techniques that can generate LFM pulses, the optical self-heterodyning technique attracts particular attention as it can produce long time-duration LFM pulses, which is a desired characteristic for high signal-to-noise ratio (SNR) at the radar's receiving station.

Although LFM pulses considerably improve the range resolution in radar systems, they might not be enough to distinguish two targets that are too close because of target masking effect. In this situations, even better resolutions can be achieved with Non-Linear Frequency Modulation (NLFM) pulses. Even though some photonic techniques are theoretically capable of producing arbitrary microwave waveforms, such as: direct space-to-time (DST) mapping; spectral-shaping and wavelength-to-time mapping (SS-WTT); temporal pulse shapping; and photonic microwave delay-line filter, none of these have been experimentally used to obtain long-time duration pulses due to the high complexity and cost. An alternative technique that can offer long-time duration NLFM microwave pulses is the self-heterodyning technique. In this way, the photonic generation of NLFM pulses through the self-heterodyning technique combines improved range resolution with high SNR, thus, it became the main motivation for this work.

This work is organized as follows. A brief historical overview of the important technological advancements that enabled this work comes after this introduction section. In chapter 2, the theoretical basis of radar waveforms and optical generation of microwave pulses is reviewed. Then, two experiments are presented. The first shows the theory and implementation of the self-heterodyning technique for generation of LFM microwave pulses, provided in chapter 3. The concepts and results of this experiment are of paramount importance for the photonic generation of NLFM pulses, which is the second experiment and central point of this work, provided in chapter 4. Though the setups of the two experiments are very similar, the NLFM generation required a profound analysis of the optical chirp phenomenon, given rise to the time-resolved optical spectroscopy technique, which, allied with a numeric simulation, have shown remarkable experimental results for NLFM microwave pulses generation. Conclusions regarding the two experiments are commented in chapter 5.

## Historical Overview

The capacity to generate microwave signals for radar systems from self-heterodyne beating is a consequence of an accumulation of discoveries and developments of many scientists throughout several years. The most important milestone events for both radar technologies and optical systems, which enabled this work, are listed below in a chronological order.

### Radar milestones

- 1865: James Clerk Maxwell presented the theory of electromagnetic waves, stating that electric and magnetic fields travel through space at light speed.
- 1900: The idea that a moving target could be detected by the reflection of electromagnetic waves was first suggested by Nicola Tesla.
- 1921: Albert Wallace Hull invented the Magnetron tube, an efficient way for microwave generation.
- 1930: An aircraft is located through electromagnetic waves for the first time by Lawrence A. Hyland, member of the Naval Research Laboratory (USA). The theory behind the experiment was not fully understood though, which lead to unstable target location.
- 1931: In Britain, the first design of a radar system is proposed by William A. S. Butement and P. E. Pollard, who equipped a ship with radar technology.
- 1935: A complete theory for aircraft detection was elucidated by Robert Watson-Watt, who is considered by many as the inventor of radar. A memorial plaque is dedicated to Watson-Watt at Daventry, UK, the site where the first successful experiment was accomplished.
- 1940: USA, Russia, Germany, France and Japan starts developing radar systems driven by the events of World War II.
- 1943: D. O. North describes the principles of a matched filter in an RCA report (Radio Corporation of America).
- 1945: Linear frequency modulation pulses are conceived on both sides of the Atlantic, as can be deduced from German, British, and U.S. patents.
- 1950: Yakov Shirman made public the development of LFM pulses, what rendered him the IEE Pioneer Award in 2009.
- 1964: Fowle carries out the stationary phase study for NLFM pulses.

- 1970: Radar's resolution improvement in terms of peak to side lobe ratio is proposed in R. E. Milleit's paper entitled "A Matched-Filter Pulse-Compression System Using a Nonlinear FM Waveform". The generation of NLFM pulses has been a focus of several studies ever since.

### **Optical milestones**

- 1887: Heinrich Hertz discovers the photoelectric effect.
- 1892: Ludwig Mach and Ludwig Zehnder contribute independently to the invention of the Mach-Zehnder interferometer.
- 1905: Einstein, in his miracle year, explains the photoelectric effect.
- 1917: In the paper "On the Quantum Theory of Radiation", Einstein establishes the theoretical basis for lasers and masers, the phenomenon known as Stimulated Emission Radiation.
- 1928: The stimulated emission radiation phenomenon is experimentally confirmed by Rudolf W. Ladenburg.
- 1953: The first maser is produced by Charles Hard Townes. This work was the basis for the construction of oscillators and amplifiers based on maser-laser principle, which rendered him, Nikolay Basov and Aleksandr Prokhorov the shared Nobel Prize in Physics, in 1964.
- 1959: The acronym LASER is first published in the paper "The LASER, Light Amplification by Stimulated Emission of Radiation", by Gordon Gould.
- 1960: Theodore H. Maiman produces the first functional laser by using a solid-state flashlamp-pumped synthetic ruby crystal to produce red laser light, at 694 nm wavelength.
- 1962: The first semiconductor laser diode, made of GaAs, is developed by Robert N. Hall.
- 1973: Though the first semiconductor optical amplifier (SOA) studies were reported shortly after 1962, Zeilder and Personick were the ones responsible for pioneering work with SOAs in 1973, driven by the advantages of heterojunction devices.
- 1982: L. Goldberg, J. F. Weller and H. F. Taylor reported the optical self-heterodyning technique for microwave generation.
- 2007: G. Kovacs and T. Berceli proposed a novel approach for microwave generation utilizing distributed feedback laser diodes wavelength chirp.
- 2015: Photonic generation of linearly chirped microwave waveforms is proposed in the paper of Olympio L. Coutinho, Jiejun Zhang and Jianping Yao.

## 2

### Theoretical Review

As the optical phenomena that support microwave generation through self-heterodyning differ drastically from the theoretical basis of radar systems, the two first sections of this chapter can be read independently. Section 2.1 describes the basic theory of radar systems, and go through the importance of NLFM pulses for better radar performances. Section 2.2 presents the optical phenomena that are the basis of the self-heterodyning technique. This chapter also contains experimental results exposed to provide a better comprehension of the theoretical basis used throughout this work. Finally, section 2.3 provides a review of photonic techniques used for microwave generation, and details the concepts of the self-heterodyning technique, which uses optical phenomena (section 2.2) for generation of microwave waveforms applicable to radar systems (section 2.1).

#### 2.1

##### Radar Waveforms

The term RADAR is an acronym for RAdio Detection And Ranging or RAdio Direction And Ranging, and it has been introduced in 1940 by the United States Navy. Soon after the World War II, the term gain popularity and lost capitalization, giving rise to the noun *radar*. The fundamental principle of radar technology is simple: an electromagnetic wave is transmitted by an antenna TX, and, when it encounters a difference in dielectric constant between the propagation medium and any surface, the wave will be reflected or scattered; the reflected/scattered wave (echo) is detected by a receiving antenna RX, which is usually the same as the transmitting one. Considering the air as the propagation medium, then, apart from atmospheric and weather conditions, the electromagnetic wave travels in a straight line and at a constant speed of  $\sim 3 \times 10^8$  m/s, thus, by measuring the time that the wave takes to output TX and reach RX, it is possible to identify the distance from the reflecting object (target).

For a better estimation of the reflecting object's position, and for an improved capacity to distinguish two objects that are close to each other, a filter is placed at the output of RX. The importance of this filter, its main

characteristics, and the transmitted LFM and NLFM waveforms that allow a better performance of the radar system will be presented throughout this section.

### 2.1.1

#### Matched Filter

Though continuous wave (CW) radars can be implemented for measurement of the instantaneous rate of change of a target's range by direct measurement of the Doppler shift [6], these cannot estimate a target's position. For position estimation, a pulsed waveform is mandatory. The simplest pulsed waveform that a radar antenna can transmit is a sinusoidal pulse. It can be defined simply by a sine function truncated with a rectangular function. Equation 2-1 [3] shows the definition of a generic sinusoidal pulse written in the complex form with amplitude  $A$ , carrier frequency  $f_0$ , time duration  $T$ , and starting at  $t = 0$ .

$$s(t) = \begin{cases} A \exp(j2\pi f_0 t) & \text{if } 0 \leq t \leq T \\ 0 & \text{otherwise} \end{cases} \quad (2-1)$$

By transmitting the pulsed waveform defined above, then the reflected pulse will have the same shape of  $s(t)$ , but it will arrive at the detector attenuated, time-shifted and carrying the noise imposed by the transmission medium. Actually, if the target is moving with relation to TX, then the Doppler effect would impact on the shape of the reflected signal, but this situation is not the focus of this work, and, thus, will not be covered. Assuming that the attenuation factor is  $K$ , the reflected pulse arrives at the detector at a time  $T_M$ , and the noise is white and Gaussian denoted by  $B(t)$ , it is possible to write the reflected signal detected at RX by:

$$r(t) = \begin{cases} KA \exp(j2\pi f_0(t - T_M)) + B(t) & \text{if } T_M \leq t \leq T_M + T \\ B(t) & \text{otherwise} \end{cases} \quad (2-2)$$

Depending on the value of  $K$ , and on the magnitude of  $B(t)$ , the information of the target's position, present in the term  $KA \exp(j2\pi f_0(t - t_0))$ , might be lost under the noise floor. It is evident that the magnitude  $A$  could be amplified to mitigate this possibility, however, since the received power declines with the fourth power of the distance (according to the radar equation [7]), a high amount of power could be necessary to reach targets in a relatively short distance.

A great alternative to minimize noise effects at the receiving antenna of a radar system is a bandpass filter with bandwidth equal to or greater than that of the transmitted signal. As the shape of the reflected signal is known to be the same of the transmitted signal, the probability of target detection is related to the signal to noise ratio (SNR) rather than to the exact waveform of the received signal. Thus, a filter receiver which has a frequency response  $H(\omega)$  that maximizes the SNR is of paramount interest.

To find the filter's transfer function that maximizes the SNR, let  $y(t)$  be the filter's output signal, and  $x(t)$  an arbitrary transmitted microwave. One can write the filter's transfer function as  $H(\omega) = Y(\omega)/X(\omega)$  [1], where  $Y(\omega)$  and  $X(\omega)$  are the Fourier transforms of  $y(t)$  and  $x(t)$ , respectively. Assuming that the noise is white and Gaussian, it is possible to calculate the SNR at a time  $T_M$ , and, moreover, to find the filter's impulse response  $h(t)$  that maximizes the SNR at the chosen time. The mathematical procedure to find  $H(\omega)$  and  $h(t)$  is detailed in [1], and results in:

$$H(\omega) = \alpha X^*(\omega) e^{-j\omega T_M} \quad (2-3)$$

$$h(t) = \alpha x^*(T_M - t), \quad (2-4)$$

where  $\alpha$  is an arbitrary constant. The filter described by Equations 2-3 and 2-4 is called *matched filter*, and it is widely used in almost every radar applications by means of hardware or software. Its name origin comes from the fact that the filter is "matched" with the input signal waveform  $x(t)$ . Note that  $h(t)$  is obtained by conjugating and time-reversing  $x(t)$ , and then convolving it with a Dirac delta function. A convolution between a signal and a time-reversed conjugated version of another is known as *cross-correlation*.

The cross-correlation operation can be understood as a measure of similarity between two signals as a function of the displacement from one to the other. In the case of the transmitted sinusoidal pulse  $s(t)$ , and the detected signal  $r(t)$ , then the cross-correlation between  $s(t)$  and  $r(t)$ , written as  $(s \star r)(t)$ , would be:

$$(s \star r)(t) = \int_{-\infty}^{\infty} s^*(\tau) r(t + \tau) d\tau$$

$$(s \star r)(t) = K A^2 \text{tri} \left( \frac{t - T'_M}{T} \right) \exp(j2\pi f_0(t - T'_M)) + B'(t), \quad (2-5)$$

where  $B'(t)$  is the result of the cross-correlation between the noise and the transmitted signal,  $\text{tri}$  is the triangular function, and  $T'_M = T_M + (T/2)$ , when the cross correlation reaches its maximum value.

Equation 2-5 shows that the envelope of the output signal is a triangular

function whenever a sinusoidal pulse is transmitted. This outcome is of great convenience since a peak power at  $T'_M$  corresponds in theory to an infinitesimal time which can be used for a precise estimation of the target's position. Thus, a matched filter that outputs a signal with maximum power at its center is specially useful. A comparison between a transmitted sinusoidal pulse  $s(t)$ , the detected signal  $r(t)$  (input of the filter), and the output of the matched filter is provided in Fig. 2.1 for a simulation with  $f_0 = 3$  MHz,  $T = 2\mu\text{s}$ ,  $T_M = 10\mu\text{s}$ ,  $A = 1$  V,  $K = 0.8$  V/V, and, for better visualization,  $B(t) = 0$  V.

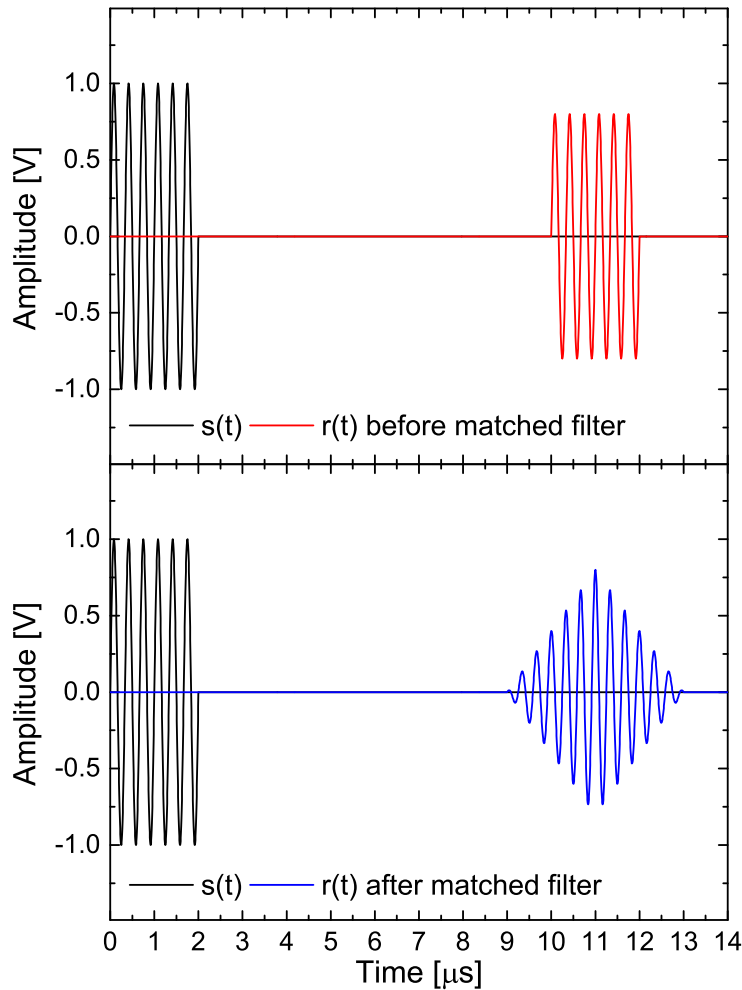


Figure 2.1: Transmitted ( $s(t)$ ) and detected ( $r(t)$ ) sinusoidal pulses in a radar system at two different stages: before (top) and after (bottom) the matched filter.

### 2.1.2

#### Range resolution and SNR

As discussed in the last section, the estimated position of a single target could be determined by transmitting a sinusoidal pulse and obtaining a signal with a triangular envelope after the matched filter. If a second target is close

to the first one, it might be difficult to distinguish their positions. This occurs because, after the matched filter, the peak of the signal reflected at the second target at time  $T'_{M2}$  can be lower than the amplitude of the signal reflected at the first target at the same time. The ability to distinguish targets that are very close to each other is called *range resolution*.

Range resolution is one of the key elements for the design of any radar system. Some radar applications, such as Fire-control radars [8], require great range resolution, and should be able to distinguish between targets that are less than one meter apart. It is clear that the range resolution must depend on the time duration  $T$  of the transmitted pulse, and, the shorter  $T$ , the better (lower) the resolution. In this way, in a radar system that a single antenna is responsible for transmission and detection, the round trip time for a transmitted pulse corresponds to the double of the distance from the antenna to the target. Thus, if  $c_0$  is the pulse speed in the propagation medium, then the range resolution  $R_r$  can be calculated from:

$$R_r = \frac{c_0 T}{2}. \quad (2-6)$$

Another crucial factor for the design of radar systems is the SNR. In the previous section the matched filter was defined in order to maximize the received SNR. The SNR can be easily calculated if the energy of the detected signal and the noise energy are known. For the transmitted pulse  $s(t)$  defined in Equation 2-1, and for a white Gaussian noise with energy  $N_0$ , then:

$$SNR = \frac{\int_{-\infty}^{\infty} |r(t)|^2 dt}{N_0} = \frac{K^2 A^2 T}{N_0} \quad (2-7)$$

By analyzing Equations 2-6 and 2-7, a tradeoff is observed between SNR and range resolution. As  $T$  reduces, the resolution improves (gets lower), and the SNR decreases. This is a major issue since both SNR and range resolution are essential elements in a radar system design. To overcome this problem, specially designed waveforms are used, and they are the focus of the following sections.

### 2.1.3 Pulse Compression and LFM

The SNR and range resolution are said to be coupled because of their unfortunate dependence of the pulse time duration. To decouple SNR and range resolution, a technique known as *pulse compression* is employed. The technique lies in transmitting a pulse long enough to result in a satisfactory SNR, but also that produces a cross-correlated signal (after the matched

filter) much smaller (compressed) than the one obtained from a sinusoidal pulse. Thus, pulse compression technique offers the high energy of a long pulse width along with the high resolution of a short pulse width.

To generate a pulse that attends to the requirements of the pulse compression technique, some changes have to be made in the pulse parameters, which are only:  $A$ ,  $T$  and  $f_0$ . Since most modern radars operate saturated [1], i.e., they keep  $A$  maximum to have the largest SNR, and  $T$  must remain long enough for a satisfactory SNR, then the changes must be made to  $f_0$ . Yakov Shirman was one of the firsts to realize this condition, and, in 1950s he made public the development of *Linear Frequency Modulation* (LFM) pulses, which rendered him the IEEE Pioneer Award in 2009 "For the independent discovery of matched filtering, adaptive filtering, and high-resolution pulse compression for an entire generation of Russian and Ukrainian radars" [9].

An LFM or linearly chirped pulse is a pulsed signal whose frequency varies linearly with time. The instantaneous frequency of an LFM pulse is presented in Equation 2-8 for a total frequency band of  $\Delta f$  around the center frequency  $f_0$ . The phase of the LFM pulse, as well as the LFM pulse itself are defined in Equations 2-9 and 2-10, respectively. Figure 2.2 displays an example of LFM pulse simulated with  $f_0 = 5$  GHz,  $\Delta f = 10$  GHz,  $A = 1$  V and  $T = 5$  ns.

$$f_{LFM}(t) = \alpha + \beta t = \left(f_0 - \frac{\Delta f}{2}\right) + \left(\frac{\Delta f}{T}\right)t \quad (2-8)$$

$$\phi_{LFM}(t) = 2\pi \int_0^t f_{LFM}(u) du = 2\pi \left( \left(f_0 - \frac{\Delta f}{2}\right)t + \frac{\Delta f}{2T}t^2 \right) \quad (2-9)$$

$$s_{LFM}(t) = \begin{cases} A \exp\left(j2\pi \left( \left(f_0 - \frac{\Delta f}{2}\right)t + \frac{\Delta f}{2T}t^2 \right)\right) & \text{if } 0 \leq t \leq T \\ 0 & \text{otherwise} \end{cases} \quad (2-10)$$

In Equation 2-8,  $f_{LFM}(t)$  was first defined in terms of the arbitrary constants  $\alpha$  and  $\beta$ , which were chosen to generate a linearly chirped pulse from  $f_0 - \Delta f/2$  to  $f_0 + \Delta f/2$ . However, despite  $f_{LFM}$  only admits positive frequencies,  $\beta$  can assume positive or negative values, resulting in an *upchirp* or *downchirp* LFM pulse, respectively. Also, as shown in Fig. 2.2, during  $T$ , every time instant corresponds to a unique frequency, which means that the frequencies present in the LFM pulse can be separated and integrated into a shorter pulse through proper filtering. Using the matched filter defined in section 2.1.1, the cross-correlation between the transmitted  $s_{LFM}(t)$  and the received  $r_{LFM}(t)$  pulses is:

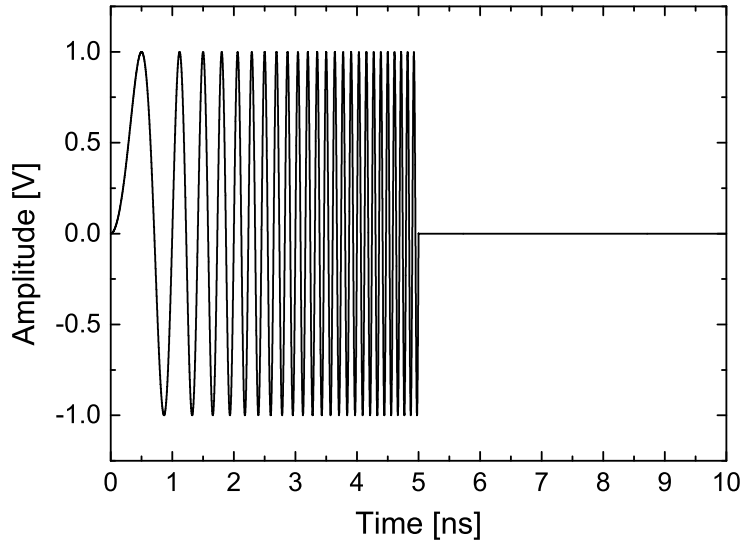


Figure 2.2: Linear Frequency Modulation (LFM) pulse for a central frequency  $f_0 = 5$  GHz, bandwidth  $\Delta f = 10$  GHz, constant amplitude of 1 V, and time duration  $T = 5$  ns.

$$\begin{aligned}
 (s_{LFM} \star r_{LFM})(t) &= \int_{-\infty}^{\infty} s_{LFM}^*(\tau) r_{LFM}(t + \tau) d\tau \\
 &= K A^2 T \operatorname{tri}\left(\frac{t - T'_M}{T}\right) \operatorname{sinc}\left[\Delta f (t - T'_M) \operatorname{tri}\left(\frac{t - T'_M}{T}\right)\right] \\
 &\quad \exp(i2\pi f_0(t - T'_M)) + B'(t), \tag{2-11}
 \end{aligned}$$

where  $r_{LFM}$  is defined by:

$$r_{LFM}(t) = \begin{cases} K A \exp(j2\pi\phi_{LFM}(t - T_M)) + B(t) & \text{if } T_M \leq t \leq T_M + T \\ 0 & \text{otherwise} \end{cases} \tag{2-12}$$

Equations 2-10 and 2-11 were used to simulate an LFM pulse and the correspondent compressed signal after the matched filter. The transmitted pulse was simulated with the same parameters that generated Fig. 2.1, but adding a frequency variation  $\Delta f$  of 2 MHz. Fig. 2.3 displays the simulation result.

From Equation 2-11 and Fig. 2.3, one can easily realize that the envelope of the matched filter output signal (compressed pulse) is governed by a sinc function, which is, by definition,  $\sin(\pi x)/(\pi x)$ . As the  $-3$  dB temporal width of a sinc function can be approximated by  $1/\Delta f$ , then the range resolution

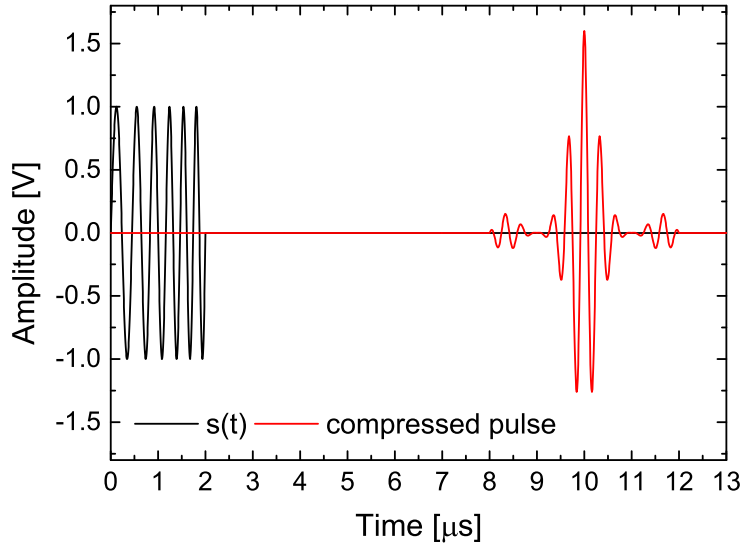


Figure 2.3: Transmitted LFM and compressed pulses for a central frequency  $f_0 = 3$  MHz, bandwidth  $\Delta f = 2$  MHz, constant amplitude of 1 V, time duration  $T = 2 \mu s$  and a round-trip time  $T_M = 10 \mu s$ .

defined in Equation 2-6 can be recalculated for a compressed pulse by [7].

$$R_{r \text{ chirp}} = \frac{c_0 \left( \frac{1}{\Delta f} \right)}{2} = \frac{c_0}{2\Delta f} \quad (2-13)$$

By comparing Equations 2-6 and 2-13, one can note that, different from the conventional case of a sinusoidal pulse, the range resolution for a compressed pulse does not depend on the pulse duration  $T$ , therefore,  $T$  can be chosen large enough to result in a satisfactory SNR whilst a large  $\Delta f$  guarantees a good range resolution. Thus, the use of LFM pulses combined with matched filters represents a great improvement in radar performance, which is analyzed in detail in [10].

The measurement of how much the range resolution is improved with pulse compression when compared to unmodulated pulses is named *pulse compression ratio* (PCR). The notation  $A:1$  is commonly used to express a system's PCR, for instance, a PCR of 100:1 means that the range resolution is reduced by 1/100 of the conventional sinusoidal pulse. From 2-6 and 2-13, the PCR can be written as:

$$PCR = \frac{R_r}{R_{r \text{ chirp}}} = \frac{\frac{c_0 T}{2}}{\frac{c_0}{2\Delta f}} = T \cdot \Delta f \quad (2-14)$$

The result  $T \cdot \Delta f$  is known as the *Time-Bandwidth Product* (TBWP).

This parameter is widely used to characterize a radar system since a high TBWP pulse represents a better performance than a low TBWP pulse. The generation of radio frequency (RF) microwave pulses with high TBWP is currently of great interest in the scientific community [11], and a photonic technique to generate such signals will be discussed in chapter 3. The TBWP impact on the range resolution is provided in Fig. 2.4, which shows the absolute value of the matched filter output for two different TBWPs: 10 (Fig. 2.4a) and 100 (Fig. 2.4b).

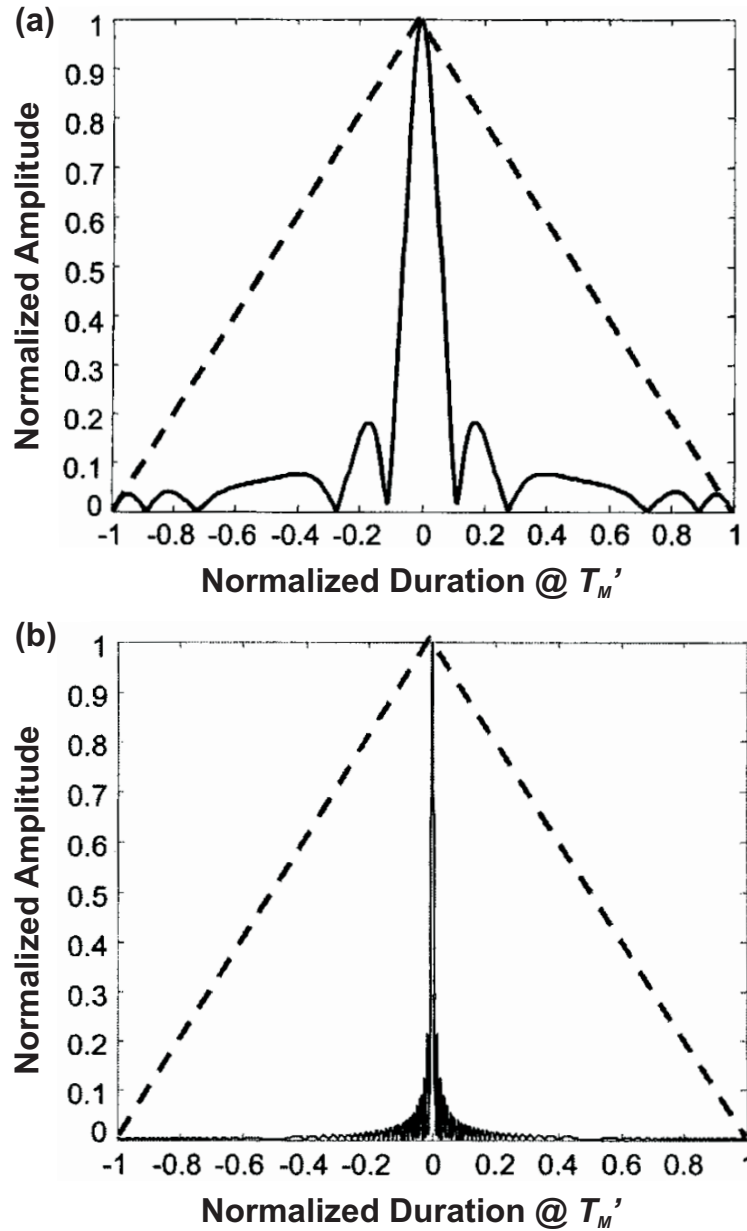


Figure 2.4: Output of matched filter (absolute value) for an LFM transmitted waveform. (a)  $TBWP = 10$ . (b)  $TBWP = 100$ . The dotted line is the output envelope of a matched filter for a simple sinusoidal pulse of the same duration [1].

### 2.1.4 NLFM

At this point, it is evident that the SNR and range resolution can be decoupled through the use of pulse compression technique. However, depending on the amplitude of the sidelobes of a given compressed pulse, weaker neighbouring targets can be masked by a high sidelobe of a stronger target, thus compromising the range resolution. Therefore the ratio between the main-lobe and the sidelobes amplitude, or peak-to-sidelobe ratio (PSLR), must be maximized to obtain better range resolutions. Fig. 2.5 shows an example of a neighbouring target masked by the sidelobes of a main target.

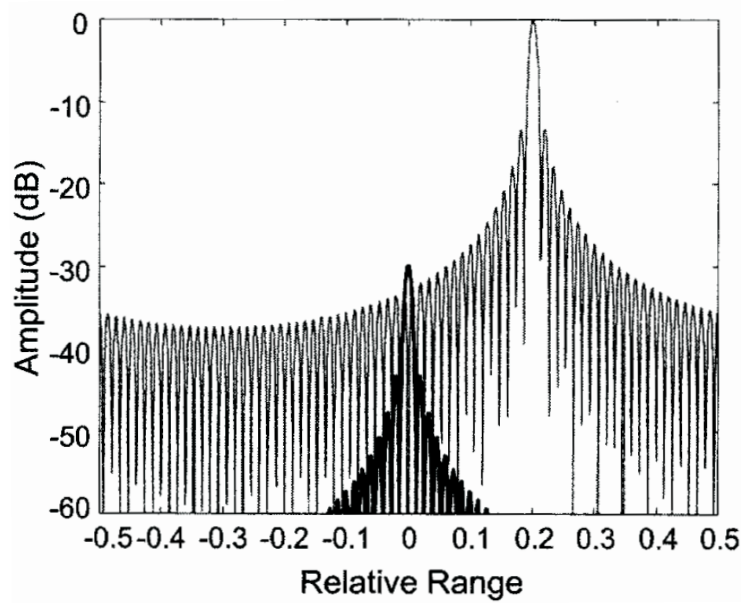


Figure 2.5: Neighbouring target masked by the sidelobes of the main target [1].

One could argue that, to improve the PSLR, hence, the range resolution, a higher TBWP pulse could be used. Unfortunately, although the TBWP has a high impact on the range resolution, it does not affect much the PSLR [1]. This effect can be observed by comparing the PSLR of Fig. 2.4a with the one of Fig. 2.6, which shows a zoom of the central portion of Fig. 2.4b. Thus, a different approach is necessary to maximize the PSLR.

There have been several studies focusing on the design of a radar system with an improvement of PSLR [12–16]. A straightforward solution presented in [15, 16] is the use of sidelobe-suppression filters in the reception. However, these filters add losses in SNR, which can be an impediment for their use. An alternative approach is to reduce the energy carried in the edges of the rectangularly-shaped spectrum of an LFM pulse. In this way, more power

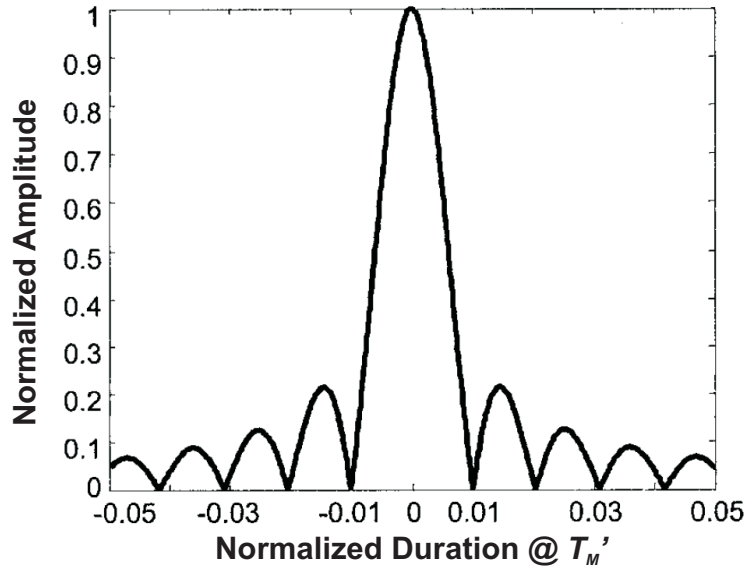


Figure 2.6: Expanded view of the central portion of Fig. 2.4b [1].

is designated to the center of the pulse spectrum, hence, the sidelobes are diminished.

The theoretical basis to design such pulses lies on the simple *stationary-phase concept*. It says that "the energy spectral density at a given instantaneous frequency  $f_k$  is relatively large if the rate of change of the frequency at that time is relatively small". This is an intuitive statement because the longer a pulse remains in a certain frequency, more power will be carried by it; in the other hand, frequencies that are rapidly swept would carry less power. The relationship between energy spectral density of a wave with complex envelope  $u(t) = g(t) \exp(j\phi(t))$  and rate of frequency change can be approximated by [3]:

$$|U(f_k)|^2 \approx 2\pi \frac{g^2(t_k)}{|\phi''(t_k)|}, \quad (2-15)$$

where  $U(f)$  is the Fourier transform of  $u(t)$ , and  $\phi''(t_k)$  is the second derivative of the phase  $\phi(t_k)$ , i.e., it is proportional to the frequency rate of change.

According to 2-15, there are three ways to reduce the energy for frequencies at the edges of an LFM pulse. The first is to lower the signal amplitude  $g(t_k)$  at the pulse edges while keeping a constant sweep rate  $\phi''(t_k)$ . Though, this technique becomes less attractive since a reduction of the amplitude of a transmitted pulse causes an SNR decay (see Equation 2-7). The second more promising way is to use a faster sweep rate at the pulse edges while keeping the amplitude constant. This approach is known as *Nonlinear Frequency Modulation* (NLFM) and it is of paramount importance in this work. The third way

is a combination of the two firsts, so both the amplitude and the frequency are modulated. This technique is named Hybrid-NLFM (HNLFM), and it is further detailed in [12], yet the unmaximized SNR still remains as a transmission issue.

To provide an example that quantifies the PSLR improvement when NLFM pulses are used, Fig. 2.7, presented in the work of Ghavamirad [2], compares the detection of LFM with NLFM pulses. In this particular case, a PSLR of less than 15 dB is found for LFM pulses, whereas a PSLR of  $\sim 35$  dB is obtained when NLFM pulses are used. This 20 dB difference is of expressive importance for avoiding target masking effects, though larger PSLRs can be achieved depending on the shape of NLFM pulses.

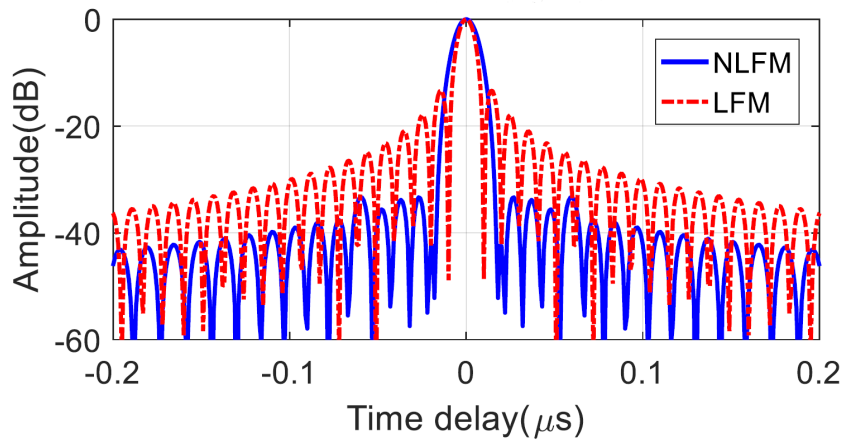


Figure 2.7: PSLR comparison between LFM and NLFM microwave pulses [2].

A typical shape of the frequency variations of an NLFM pulse is shown in Fig. 2.8a, while Fig. 2.8b displays the correspondent energy spectral density [3]. Note that, at the pulse edges, the frequency varies rapidly, hence, corresponding to a lower energy spectral density as expected by the stationary-phase concept. Frequencies at the center of the pulse have a lower rate of change, thus, a higher energy spectral density.

Due to the great advantages of NLFM pulses in radar systems, their generation, through photonic techniques, was the major motivation for the experiments presented in chapter 4. In the following section, the theoretical basis that supports the photonic techniques used in these experiments is presented.

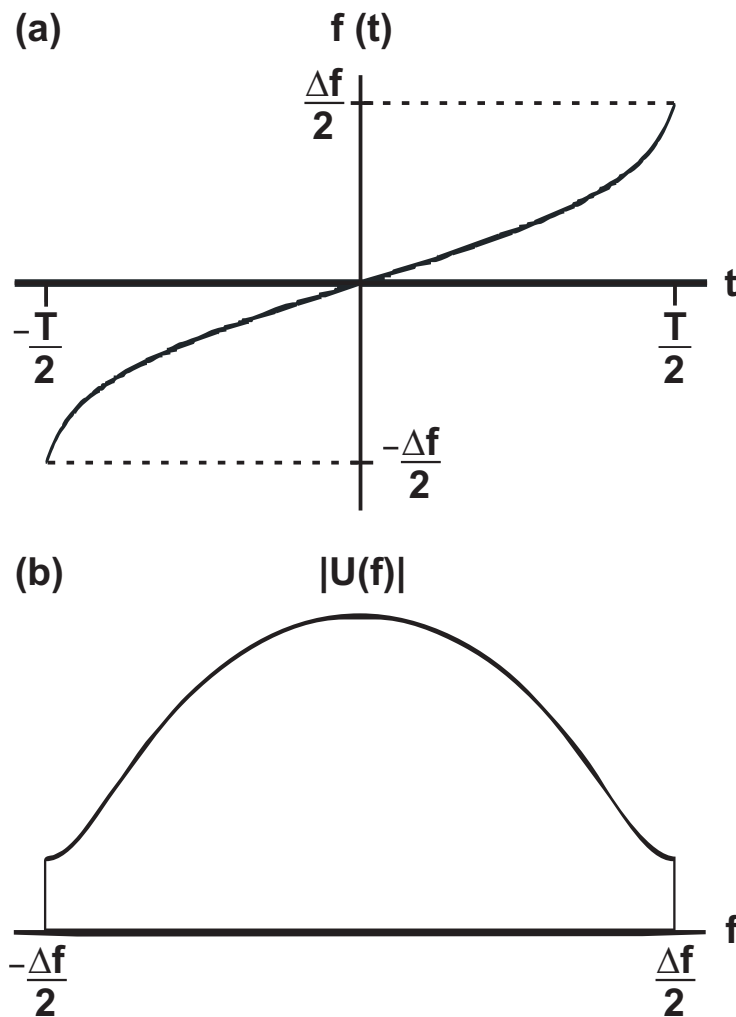


Figure 2.8: Typical shape of the frequency chirp (a) and energy spectral density (b) of an NLFM pulse [3].

## 2.2 Optical Phenomena

The central emitting frequency of semiconductor laser diodes varies with the modulation current applied directly in the light source. This phenomenon is known as *optical chirp*. Although sometimes it comes unfortunate, as it can broaden a pulse duration, hence, contributing to a greater dispersion and adding limitations on a communication bit rate [4], one can take advantage of its properties to generate microwave pulses through optical beating [11].

Though the optical chirp is the central optical effect backing the experiments presented in chapters 3 and 4, it is fundamental to understand elementary concepts as optical interference, coherence time and of the operation of semiconductor optical amplifiers (SOAs) as well as a Mach-Zehnder Interferometer (MZI). Thus, this section is divided in four parts: the first one explains the physical effect behind the laser chirp phenomenon, and presents experimental measurements that validates the theory (sections 2.2.1 - 2.2.3). The

second part comments about the working principle of SOAs, and how they can be used as optical chopper devices (section 2.2.4). The third part presents the theory of optical interference/beating (section 2.2.5), while the fourth part defines the working principle of interferometers. These four parts constitute the theoretical basis for section 2.3, which unifies the concepts here discussed by presenting the self-heterodyning technique for generation of chirped microwave pulses.

### 2.2.1

#### **Lasers and Optical Chirp**

Lasers are optical oscillators that comprise, inside an optical resonant cavity, an amplification system whose output is fed back to the input with matching phase. The lasing process can start with a small optical signal (could be even optical noise) at the input of the amplification system if the optical signal has frequency components lying within the bandwidth of the amplifier. Optical amplification is achieved through stimulated emission radiation, which is only possible if the condition of population inversion is guaranteed.

As the output of the amplification system is fed back to its input, it goes over another amplification cycle, and this process continues until gain saturation is achieved. At this point, a large output optical signal is produced and the system reaches steady state condition. However, to obtain amplified oscillation, two conditions must be satisfied: first, the amplifier gain should be greater than the losses in the resonant cavity, and second, the total phase shift in a single round trip must be a multiple of  $2\pi$ , which is necessary for phase matching between the original input and the one fed back to the amplifier. These are known as the gain and phase conditions for laser oscillation.

If gain and phase condition are satisfied, oscillation occurs, and the optical power inside the cavity increases until the amplifier reaches saturation. As mentioned, a steady state condition is achieved when gain saturation takes place. At this condition, the amplifier gain decreases and it equals the losses in the cavity, when steady-state oscillation prevails. In order to use the produced optical power, one of the mirrors of the optical resonant cavity is made partially reflective, so a portion of the optical power is constantly extracted from the cavity.

Semiconductor Laser Diodes (LD) are known to have a threshold bias current,  $I_{th}$ , from which gain condition is satisfied, thus, light is emitted in a coherent way. Every increase in the bias current above  $I_{th}$  corresponds to a linear increase of carrier density in the active region, resulting in a higher photon flux, thus, a higher optical power. This linear relation occurs till a

saturation point, where a current increase will no longer correspond to an optical power increase.

In the linear operation region of LDs, a change in the carrier density leads not only to an optical power change, but also to a change of refractive index in the active region [17]. Any change in the refractive index alters the effective length of the laser cavity, and, as this length determines the emitted wavelength [5], thus a change in carrier density (bias current) modifies the emitting wavelength. Due to the fast nature of this phenomenon it is referred as *dynamic chirp* [18].

Another important effect on the emitting wavelength occurs also as a consequence of a change in the bias current. As the bias current increases, the temperature of the active region also increases, leading to thermal expansion of the laser cavity, therefore, a change in the emitting wavelength. This phenomenon will be referred here as *thermal chirp*. For an abrupt change in the bias current (up to few nanoseconds), which can be achieved by biasing the laser with a pulsed current source, the dynamic chirp governs the variation of the emitting wavelength; after long time periods (tens of nanoseconds) the thermal chirp dominates these variations. The cause and effect diagram of Fig. 2.9 summarizes these two coexistent effects.

Thermal chirp and dynamic chirp are the two main components of the overall optical chirp observed in semiconductor lasers. The two following sections are dedicated for the individual study of these two components.

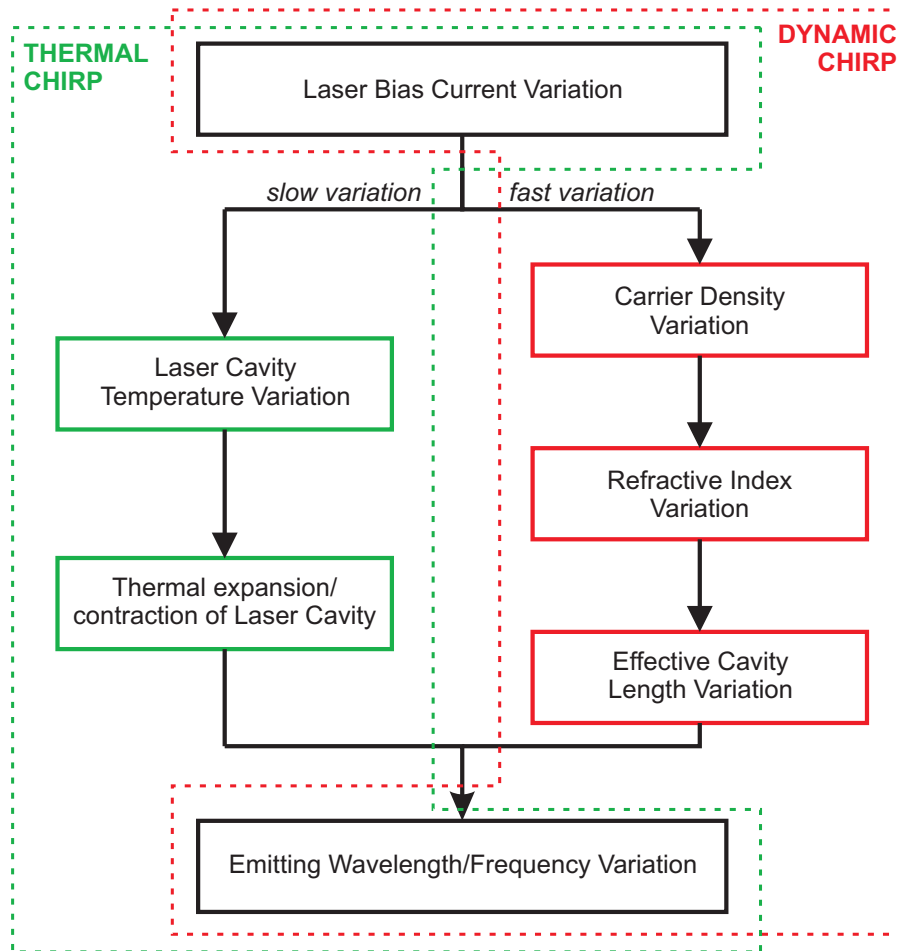


Figure 2.9: Cause and effect diagram of the main components responsible for the overall optical chirp phenomenon: thermal and dynamic chirp.

### 2.2.2 Thermal Chirp

To verify the effect of the predominant thermal chirp in a Distributed Feedback LD (DFB-LD), a measurement of its central emitting wavelengths/frequencies for different bias currents was performed. The DFB-LD used in the experiment was a Mitsubishi FU-68PDF-5 [19]. To avoid external heat/cold sources, the Newport 3040 Temperature Controller [20] was used. The bias currents were selected by the 505 Laser Diode Driver [21], and the Optical Spectrum Analyzer model MS9740A [22] was chosen for the measurement of the central frequencies. Fig. 2.10 shows the measurement result.

The chirp measurement presented in Fig. 2.10 shows a red shift when the current bias increases. Considering the approximately linear part of the curve (bias currents above the 18 mA threshold) it was possible to calculate a frequency variation of  $\sim 0.9$  GHz/mA. This value is known to be the average chirp parameter  $\alpha_{ch}$ , or chirp coefficient [11], and it will be further discussed

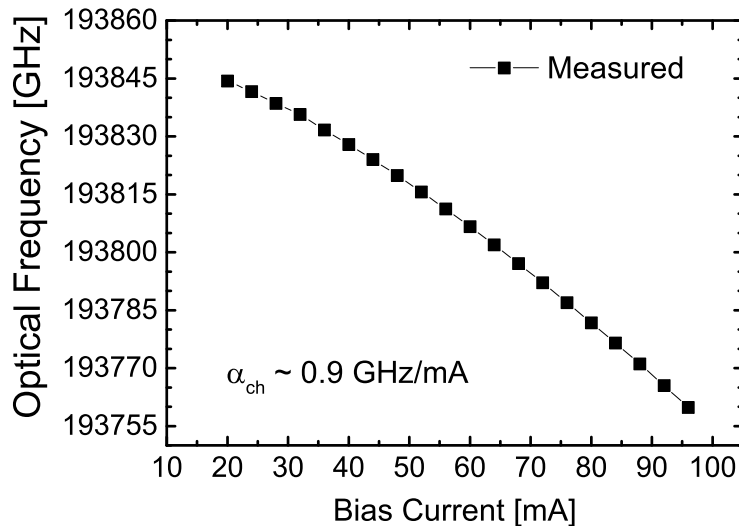


Figure 2.10: Measured output frequency of a DBF-LD for different input bias currents.

in section 2.3.

The result of Fig. 2.10 shows that, after a long time period, the emitting frequency remains fixed for every bias current. As this period is long enough for temperature stabilization, then it is possible to affirm that the measurement is taken in the permanent regime. A different measurement that takes into account the transient regime of the same effect is here named as the thermal chirp transitory measurement. It can be performed by modulating the bias current with a sinusoidal function of constant amplitude for several different frequencies. For low modulation frequencies there will be more time for the temperature to respond to the current changes in a single modulation period, thus, a larger temperature variation should be observed, hence, leading to a larger chirp. Since the thermal chirp is a slow effect, as the modulation frequency increases, the total chirp should decrease, as there is less time for the temperature to respond to the same current variation.

An thermal chirp transitory measurement was performed for the same Mitsubishi FU-68PDF-5 DBF-LD. In this experiment the central frequency sweeps across a larger or lower bandwidth, depending on the modulation frequency. This bandwidth represents the total chirp and can be measured through the Max Hold auxiliary mode of the OSA. The measurement result is presented in Fig. 2.11 for a constant modulation amplitude of 20 mA, a fixed bias current of 50 mA (bandwidths centered at  $\sim 193817GHz$  according to Fig. 2.10), and four different modulation frequencies: 1 Hz, 100 Hz, 10 kHz and 100 kHz. As expected, the bandwidths are larger for lower modulation frequencies. Also, higher powers were measured for lower optical frequencies, which agrees with the theory since higher bias currents correspond to lower

emitting frequencies (Fig. 2.10) and also to higher optical powers.

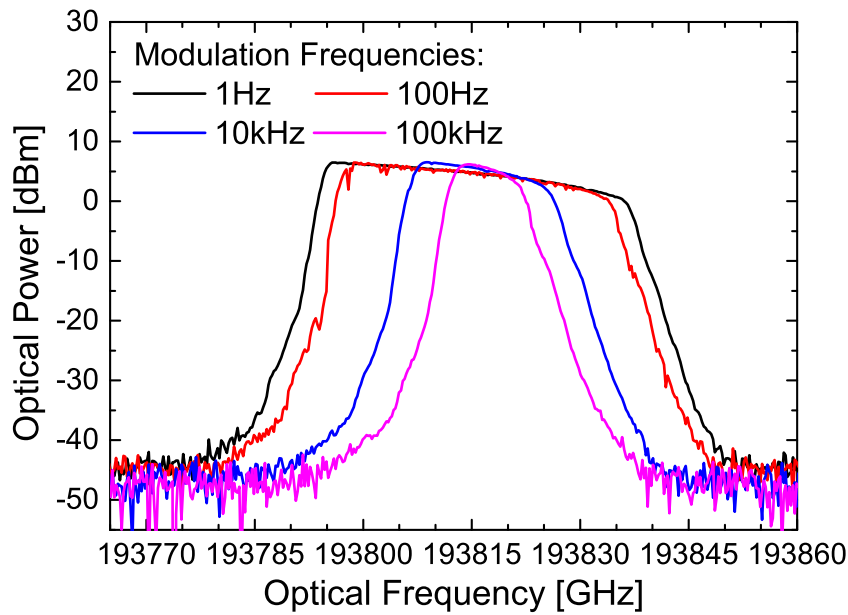


Figure 2.11: Thermal chirp transitory simulation of a DFB-LD for four different modulation frequencies.

### 2.2.3

#### Dynamic Chirp

Different from the thermal chirp, the dynamic chirp phenomenon demands sophisticated apparatus for its measurement, as it occurs in extremely short periods of time (picoseconds). Therefore, to measure rapid frequency changes, dynamic chirp is usually studied for short optical pulses, referred as chirped pulses. For instance, Wiesenfeld, Tucker and Downey measured the dynamic chirp in gain-switched single-mode injection lasers with a resolution of 0.5 ps [23]. More studies on this phenomenon are reported in [24–28], from which it has been observed that the frequency chirp depends on the shape and the width of the optical pulse. For rectangular pulses, the dynamic chirp is observed near the pulse edges: a blue shift occurs at the leading edge, while a red shift at the trailing edge. Note that this behaviour is exactly the opposite of the thermal chirp.

Fig. 2.12 [4] shows the dynamic chirp for rectangular current pulses of 500 ps duration. The solid curve corresponds to the simulated optical power, while the dashed curve represents the simulated dynamic chirp. In the simulation, the laser was biased with a current ten percent higher than the threshold current ( $I_b = 1.1I_{th}$ ), and the modulation pulse amplitude was set to the same value of the threshold current ( $I_m = I_{th}$ ). The rise time and fall time were  $\sim 100$ ps

and  $\sim 300$ ps, respectively. The shift toward the blue at the leading edge, and toward the red at the trailing edge can be observed.

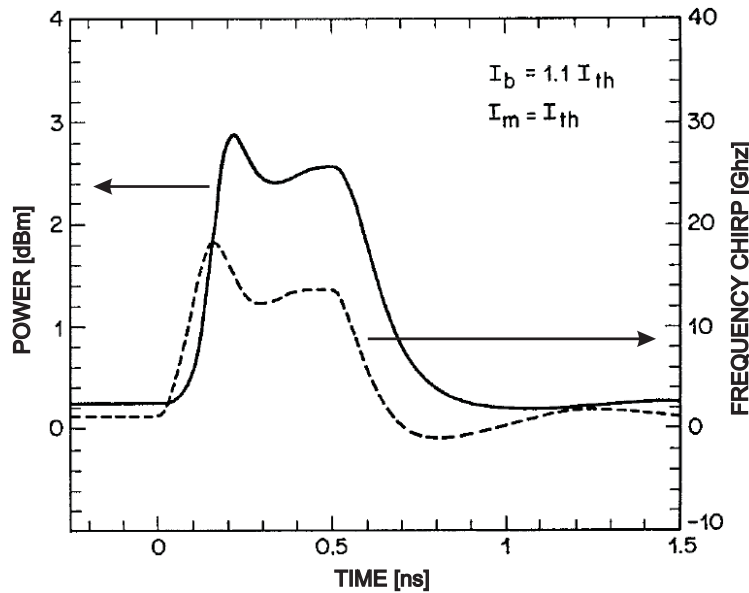


Figure 2.12: Simulated modulation response of a semiconductor laser to 500 ps rectangular pulses. Solid curve shows the pulse shape and the dashed curve shows the dynamic chirp imposed on the pulse [4].

An interesting effect can be observed by comparing Figs. 2.10 and 2.12. For an abrupt increase in the bias current, for instance, from 40 to 60 mA in few nanoseconds, a blue shift will occur at first, consequence of the dynamic chirp. However, after several nanoseconds, the thermal chirp prevails, which will lead the emitting frequency toward the red. Therefore, the dynamic and thermal are said to be opposite effects, as they shift the optical frequency in opposite directions. Both thermal and dynamic chirps are central phenomena for the main experiment of this work, which is further presented in chapter 4.

#### 2.2.4 Semiconductor Optical Amplifiers

The same mechanism that is used for light amplification in laser diodes is responsible for amplification in optical amplifiers. Actually, an optical amplifier can be thought of as a laser but without the feedback to the amplification system, which is minimized by the use of anti-reflection coatings.

A semiconductor optical amplifier (SOA) is simply an optical amplifier with a semiconductor-based gain medium. A typical schematic of an SOA is provided in Fig. 2.13. SOAs can be categorized as travelling-wave (TW) amplifiers, which emphasizes the fact that the amplified signal is not fed back to the amplifier, i.e., it travels only in the forward direction. A considerably

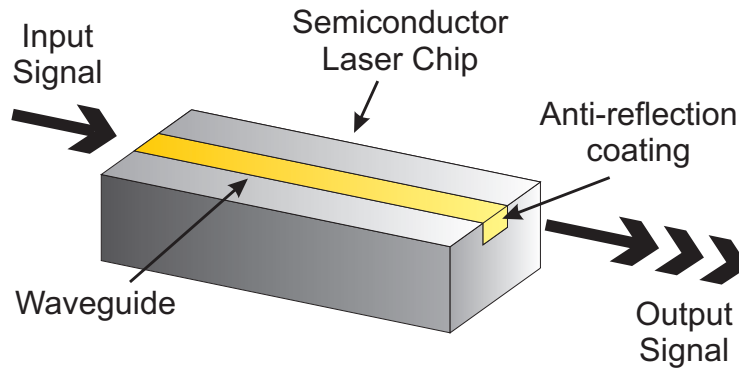


Figure 2.13: Schematic of a Semiconductor Optical Amplifier.

large undesired feedback is noted for SOAs, as the semiconductor's cleaved facets have a natural reflectivity of around 32 %, what only reinforces the need of anti-reflection coatings. In fact, the reflectivity of SOAs must be lower than 0.1 % for an operation as a TW amplifier [4]. Also, to provide an amplification gain of 30 dB, the facets reflectivity must be such that  $\sqrt{R_1 R_2} < 1.7 \times 10^{-4}$ , where  $R_1$  and  $R_2$  are the reflectivities of both facets.

An interesting feature that can be taken advantage of when using SOAs is the possibility to use them to work as on-off switches, enabling or not the transmission of light. Since the amplification mechanism is the same of a laser, that is, it demands the population inversion condition for amplification, then, if this condition is not satisfied, the semiconductor would work as an absorber, and no light will be measured at the output. For instance, if the SOA pumping system is driven by electric pulses, then an incoming continuous wave (CW) light will be amplified and chopped by the semiconductor amplifier, resulting in optical pulses at the output.

This characteristic of SOAs is of great importance for selecting appropriate portions of a chirped input optical signal. More on this topic will be discussed in section 3.3.

### 2.2.5 Optical Interference

Two or more optical waves are said to interfere with each other if they are simultaneously present in the same region of space and time. It follows that the resulting wave is the sum of the individual waves, and the phase relationship between the superposed waves is the capital factor for the resulting wave intensity. This last statement can be better understood by looking at the *interference equation*. A derivation of the interference equation start by defining a generic monochromatic waveform as [5]:

$$u(r, t) = a(r) \cos(2\pi\nu t + \varphi(r)), \quad (2-16)$$

where  $a(r)$  is the amplitude,  $\nu$  is the linear frequency and  $\varphi$  is the phase.

A convenient complex representation of  $u(t)$  is given by:

$$U(r, t) = a(r) \exp[j\varphi(r)] \exp[j2\pi\nu t], \quad (2-17)$$

where  $u(r, t)$  is the real part of  $U(r, t)$ . For a fixed position  $r$ , the position dependent terms  $a(r)$  and  $\varphi(r)$  can be replaced by  $A$  and  $\phi$ , respectively, leading to the time dependent complex wavefunction:

$$U(t) = A \exp[j2\pi\nu t + \phi] \quad (2-18)$$

As the optical intensity is defined as the absolute square of the complex waveform, i.e.,  $I(t) = |U(t)|^2$ , then, for simplicity, assuming a constant intensity,  $A$  will be henceforth replaced by  $\sqrt{I}$ . Now, it is possible to consider two waves,  $U_1(t)$  and  $U_2(t)$ , which coexist at the same region and at the same time:

$$\begin{aligned} U_1(t) &= \sqrt{I_1} \exp[j(2\pi\nu_1 t + \phi_1)] \\ U_2(t) &= \sqrt{I_2} \exp[j(2\pi\nu_2 t + \phi_2)] \end{aligned}$$

The resulting wavefunction  $U_r(t)$  is given by the sum of  $U_1(t)$  and  $U_2(t)$ , while the overall optical intensity is  $I_r(t) = |U_r(t)|^2$ . Thus, the interference equation [4, 5] is defined as:

$$\begin{aligned} I_r(t) &= |U_r(t)|^2 = |U_1 + U_2|^2 = |U_1|^2 + |U_2|^2 + U_1^* U_2 + U_1 U_2^* \\ I_r(t) &= I_1 + I_2 + 2\sqrt{I_1 I_2} \cos(2\pi\nu_{IF} t + \phi) \end{aligned} \quad (2-19)$$

The frequency  $\nu_{IF}$  is known as the *intermediate frequency*, and it corresponds to the frequency difference between  $\nu_1$  and  $\nu_2$ , while  $\phi = \phi_1 - \phi_2$  is a constant phase term.

At this moment, it is important to define the phenomenon of optical beating, and to highlight its difference from optical interference. Whenever two optical waves are superposed, for instance, in an optical fiber, they will coexist and interfere throughout the entire waveguide. However, if a photodetector is placed at the end of the fiber, the photons will be absorbed and the detected photocurrent will be proportional to the overall optical intensity. Thus, the photocurrent frequency will be  $\nu_{IF}$ , and it is said that the optical waves have beaten, giving rise to the name *optical beating*.

Coherent lightwave systems make use of optical beating for homodyne and heterodyne detection [4]. In section 2.3, optical beating of two chirped

pulses is used for generation of linearly chirped microwave pulses.

### 2.2.6 Interferometers

Interferometers are optical devices that splits a lightwave in two or more less power waves, and then recombines them after unequal optical paths. Thus, the output of an interferometer is a superposition of the split waves, which will interfere as stated in section 2.2.5. Depending on the optical path difference between the split waves, any interference scenario is possible, from constructive to destructive interference.

The three most famous interferometers are the Michelson interferometer, the Sagnac interferometer, and the Mach-Zehnder interferometer. Fig. 2.14 displays the schematic of these three interferometers in an open path situation. The same setups can be easily assembled with optical fibers, but the open path case provides a better visualization of the path that light travels through. In the three shown interferometers, a light wave  $U_0$  is split by beamsplitters, which add a phase difference of  $\pi/2$  between the transmitted and reflected waves, then, mirrors are responsible to direct the transmitted and reflected waves to another (or the same) beamsplitter, where light recombination is performed.

In the Sagnac interferometer, though the split waves travel in opposite directions, they travel the same distance, which sometimes is an unwanted feature. Also, it is evident from Fig. 2.14 that the mirrors' position in the Michelson interferometer can be chosen arbitrarily to impose a different distance for each split wave. However, if an optical isolator is not properly placed at the input of this interferometer, there might be a considerable parcel of light coming back to the emitting source, which can cause it permanent damage depending on the working optical power. In this way, a Mach-Zehnder interferometer has two characteristics that made it the premier choice for the experiments presented in chapters 3 and 4: possibility of arbitrary path difference between the split waves, and no back propagated light at the input (apart from Rayleigh back scattering [4]).

Although it may not be clear from Fig. 2.14, the path difference can be arbitrary selected in Mach-Zehnder interferometers assembled with optical fibers. This will be clear in the schematic experimental setups presented in sections 3.1 and 4.1.

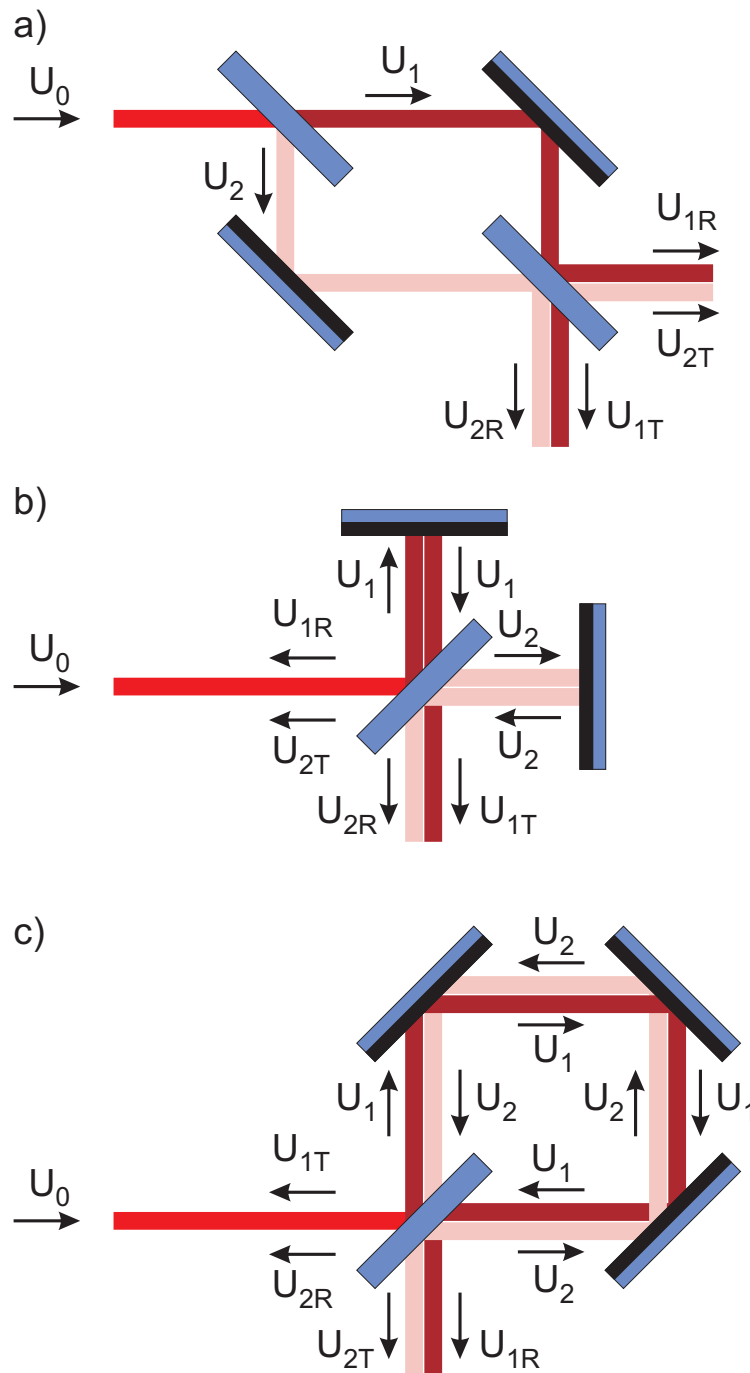


Figure 2.14: (a) Mach-Zehnder interferometer, (b) Michelson interferometer and (c) Sagnac interferometer. An input wave  $U_0$  shown in red is split into two waves  $U_1$  and  $U_2$ , shown separately in dark and light red for ease of visualization, but are actually congruent [5].

### 2.3 Generation of Chirped Microwave Pulses

The importance of LFM pulses (or linearly chirped pulses) with high TBWP for radar systems was discussed in section 2.1.3. Traditionally, microwave chirped pulses have been electrically generated, usually employing

voltage controlled oscillators (VCOs), digital synthesizers, surface acoustic wave (SAW) devices [29] and high-speed large gate-count Field Programmable Gate Array (FPGA) [30]. Nevertheless, due to the electronic limitations, other techniques are required to generate higher frequencies and bandwidths.

After the advent of semiconductor lasers, fast photodiodes, low loss optical fibers, etc., the use of photonic techniques to generate, process, transmit and receive microwave chirped signals became a research subject that has raised a lot of interest. There are many advantages in generating and processing microwave chirped signals in the optical domain: higher instantaneous ultra-wideband, easy and large spectral tuning range, compactness of the circuits, light weight components, better immunity to electromagnetic interference and compatibility with radioover-fiber technology [31–36].

In this section, the concepts of laser chirp and optical beating discussed in section 2.2 are used to establish the theoretical basis for photonic generation of chirped microwave pulses with high TBWP in a self-heterodyne scheme. The section is divided as follows: first, it is presented in section 2.3.1 a review of the main photonic techniques used for microwave generation. Then, to support the comprehension of the self-heterodyning technique, section 2.3.2 defines the generated RF linearly chirped signal in a simple mathematical approach. The self-heterodyning technique used for microwave generation is explained in section 2.3.3. Last, a theoretical study on the TBWP optimization is provided in section 2.3.4.

### 2.3.1

#### Review of Photonic techniques for Microwave Generation

Due to the increasing number of research dedicated to photonic generation of microwave waveforms, six categories [31, 37] were elected to divide the main works in the area: 1) Direct space-to-time (DST) mapping; 2) Spectral-shaping and wavelength-to-time (SS-WTT) mapping; 3) External modulation technique; 4) Microwave delay-line filter; 5) Dual-wavelength single-longitudinal-mode; and 6) Self-heterodyning. This section presents an overview of techniques 1 to 5. The following sections are exclusively dedicated to the self-heterodyning technique.

**1) Direct space-to-time mapping.** In DST mapping, a pulsed optical source is directed to an optical pulse shaper, which establishes a desired pulse burst for opto-electric conversion at a limited bandwidth photodiode. As the 3 dB time duration of optical pulses from a pulsed source is usually around few femtoseconds, high frequency components are carried on the optical pulses. Thus, the limited bandwidth photodiode performs two functions, first, opto-

electric conversion of the pulse burst sequence, and second, smoothing of isolated optical pulses. The result is a microwave waveform at the output of the photodiode. Note that, by linearly increasing the pulse spacing at the optical pulse shaper, an LFM microwave waveform is generated. A mode locked laser with 40 MHz repetition rate was used in [38] to generate a 48 GHz microwave tone at the output of a 50 GHz bandwidth photodetector through DST mapping.

**2) Spectral-shaping and wavelength-to-time mapping.** The technique consists in filtering a wide optical spectrum of a pulsed optical source, and then using a dispersive device followed by a high-speed photodiode for microwave generation. The optical filter is responsible for turning a wide spectrum into a pulse-shaped spectrum. The dispersive medium, usually a single mode fiber, maps the wavelength spectrum into a time domain signal. The high-speed photodiode converts the optical signal into a microwave waveform. Linearly chirped microwave pulses centred at 15 GHz with a  $\sim 27$  GHz bandwidth were obtained in [39], where two superimposed chirped fiber bragg gratings were used for optical filtering. The full width half maximum (FWHM) of the pulse envelope was around 1.25 ns, leading to a TBWP of 37.5.

**3) External modulation technique.** By biasing an external intensity modulator in phase, the frequency modulation is doubled in the optical domain. In this case, a high quality electrical microwave generator is necessary to obtain a stable microwave with the frequency-doubled. Although this method needs an agile frequency sweeper to generate LFM waveforms, it has the advantage of being one of the simplest methods for high frequency microwave generation. An intensity Mach-Zehnder Modulator (MZM) was used in [40] to achieve a 36 GHz microwave tone from a 18 GHz modulation signal.

**4) Microwave delay-line filter.** Photonic microwave delay-line filters can be easily employed for the generation of linearly chirped microwave signals. In case a chirp-free pulse is applied to a photonic microwave delay-line filter with a linearly increased or decreased group delay response, then a linearly chirped microwave signal is obtained at a photodiode. On the other hand, the implementation of arbitrary microwave waveforms is rather complicated by this method, as the filter must not have a linearly increased group delay. However, Yao and Dai have successfully overcome this problem by using delay-line structures with non-uniformly spaced taps [41].

**5) Dual-wavelength single-longitudinal-mode.** A microwave tone can be photonically generated with an individual laser source. However, to obtain an intermediate beat frequency at a photodetector from an individual laser, it must have a single wavelength with dual longitudinal modes, or

dual wavelengths operating in a single longitudinal mode. A fiber ring laser with dual wavelength operating in a single longitudinal mode is theoretically proposed and experimentally verified in the work of Chen and co-workers [42], where microwave tones of 6.95, 18.68, 40.95 GHz were generated.

### 2.3.2 RF Linear Chirp

As mentioned in section 2.2.1, semiconductor LDs, when driven by time-varying currents, suffer central optical frequency variations within a certain limited range, which can reach several tens of GHz. This laser chirp phenomenon can be used to generate microwave signals by using several photonic techniques [31, 35]. The instantaneous center optical frequency  $\nu(t)$  emitted by the LD can be calculated by taking into account the chirp coefficient  $\alpha_{ch}$  [GHz/mA]. This coefficient is dependent on various fundamental dynamic parameters like complex index of refraction, carrier density, carrier lifetime, modulated power, junction temperature and, in general, should be experimentally obtained [23, 43]. The basic relationship between  $\nu(t)$  and  $\alpha_{ch}$  can be written as [18, 44]:

$$\nu(t) = \nu_0 + \alpha_{ch}(t) \cdot i_{LD}(t), \quad (2-20)$$

where  $\nu_0$  stands for the LD optical frequency when driven only by the bias current  $I_b$ , and  $i_{LD}(t)$  is the laser diode modulating current. Following 2-20, the instantaneous optical frequency deviation from  $\nu_0$  can be written as:

$$\Delta\nu(t) = \alpha_{ch}(t) \cdot i_{LD}(t) \quad (2-21)$$

The differences between optical frequencies, sampled in different instants of time, result in RF frequencies  $f_{RF}(t)$  (few MHz to hundreds of GHz), and is given by:

$$f_{RF}(t) = \nu(t + t_0) - \nu(t), \quad (2-22)$$

where  $t_0$  is the time difference between samples. Rewriting 2-22 in terms of the instantaneous modulating current, the RF frequency is:

$$f_{RF}(t) = \alpha_{ch}(t + t_0) \cdot i_{LD}(t + t_0) - \alpha_{ch}(t) \cdot i_{LD}(t) \quad (2-23)$$

For a small interval  $t_0$ , the chirp coefficient can be assumed approximately constant and, with the differential current considered around its instantaneous point, the above equation can be written as:

$$f_{RF}(t) = \alpha_{ch} t_0 \frac{di_{LD}(t)}{dt} \quad (2-24)$$

Assuming  $i(t) \propto t^2$ , then 2-24 leads to linear frequency dependence, i.e.  $f_{RF}(t) \propto t$ , named as RF linear chirp. However, the chirp parameter usually is not constant with the instantaneous current, thus resulting in nonlinearity of the RF frequency shift. Hence, the resulting  $f_{RF}(t)$  can be handled by changing either:  $\alpha_{ch}$ , i.e. using a different LD;  $t_0$ , by choosing different time interval; or the current function  $i_{LD}(t)$ .

### 2.3.3

#### The Self-Heterodyning technique for microwave generation

The self-heterodyning technique for microwave signal generation was first reported in 1982 by Goldberg, Weller and Taylor [45]. The technique consists in interfering the light from a laser with light from the same laser emitted earlier at a different frequency, and then, beating the superposed waves in a photodetector. Goldberg and co-workers have used an unbalanced MZI with a fiber length difference of 1.1 km to impose a  $5.5 \mu\text{s}$  retard for the delayed-interference. Also, a square wave was chosen to modulate the injection current of a GaAlAs laser diode above a bias current of  $I_b \sim 1.25 I_{th}$ . As the changes in the intensity are proportional to the frequency changes (see Fig. 2.12), the frequency correspondent to the high amplitude of the square wave beats with the frequency correspondent to the low amplitude of the square wave, therefore, generating a microwave signal.

After 1982, other modulation schemes using the self-heterodyning concept were developed to generate microwave waveforms. In 2007, Kovács and Bercei used the self-heterodyning technique to generate microwave signals by direct modulating a DFB laser diode with low frequency triangular and rectangular injection current waveforms [18]. An optical frequency difference, defined by the MZI delay, beats in a photodiode, thus, generating microwave signals. In this way, the time delay at the MZI and the injected current waveform are the key parameter to define the frequency of the generated microwave.

A year after Kovács work, Bernacil and co-workers have used a fast wavelength switching Sampled-grating Distributed Bragg Reflector (SG-DBR) tunable laser in a self-heterodyne scheme for microwave generation [37]. The phase section of the SG-DBR was modulated with a square wave current, and the MZI time delay was chosen to correspond to half of the modulation period. In this way, a constant optical frequency difference was obtained at the output of the interferometer, hence, generating microwave signals at a photodiode. Experimental measurements have proven the generation of microwave signals up to 12 GHz.

Coutinho, Zhang and Yao used long ( $4 \mu\text{s}$ ) parabolic pulses to generate

a linearly chirped microwave waveform in a self-heterodyne scheme [44]. In the experiment, the optical power of higher microwave frequencies is higher than that of lower microwave frequencies, because higher currents (right edge of an increasing current parabola) correspond to higher optical powers. To overcome this problem, an MZM acting as a synchronized attenuator was introduced before the MZI in order to equalize the optical powers of the generated linearly chirped microwave. Beyond power equalization, the MZM also works as a chopper device by allowing only a certain portion of the parabolic pulse to pass toward the MZI, yielding in a generated microwave with a desired bandwidth and time width. Thus, Coutinho and co-workers achieved a nearly flat-top microwave pulse with a large TBWP of 4200 (4.2 GHz bandwidth  $\times$  1  $\mu$ s duration after pulse chop).

A TBWP extension to  $\sim 35000$  and further to  $\sim 74000$  has been achieved by using the same technique but with a different procedure for power equalization and pulse chop, which will be detailed in chapter 3 [11, 46]. Even higher values of TBWP were already reported elsewhere using other techniques. J. Yao and co-workers reported 80000 using coded modulation [47]. The latter figure was also obtained by Weiner and co-workers with frequencies up to 20 GHz using a modified pulse shaping plus frequency-to-time mapping scheme [32]. Additionally, a TBWP of  $1.2 \times 10^5$  is achieved by controlling the optical injection strength of a semiconductor laser [33].

One of the great advantages of the self-heterodyning technique for microwave generation is its simplicity, which is due to the straightforward setup. It only requires an unbalanced MZI and a single laser emitting an optical power  $P_L(t)$  from the corresponding electric field [48]:

$$E_{in}(t) = \sqrt{P_L(t)} \exp[j(2\pi\nu(t)t + \varphi(t))] \quad (2-25)$$

By imposing a time delay  $\tau$  in one of the unbalanced interferometer's arms, the output field will be the superposition of the input and its delayed replica as follows:

$$E_{out}(t) = \sqrt{\frac{P_L(t)}{2}} \exp[j(2\pi\nu(t)t + \varphi(t))] + \sqrt{\frac{P_L(t + \tau)}{2}} \exp[j(2\pi\nu(t + \tau)(t + \tau) + \varphi(t + \tau))] \quad (2-26)$$

The superposed optical signal  $E_{out}(t)$  beats in a fast photodiode, thus generating an RF photocurrent given by:

$$i_{RF}(t) = \Re P_{out}(t), \quad (2-27)$$

where  $\mathfrak{R}$  is the photodiode responsivity and  $P_{out}(t) = |E_{out}(t)|^2$ . Assuming a constant optical power, which can be achieved through power equalization as in [44], i.e,  $P_L(t) = P_L(t + \tau) = P_L$ , then the term  $P_{out}(t)$  in equation 2-27 can be rewritten as:

$$P_{out}(t) = |E_{out}(t)|^2 = P_L [1 + \cos(\phi_2 - \phi_1)], \quad (2-28)$$

$$\text{where: } \phi_1 = (2\pi\nu(t)t + \varphi(t))$$

$$\phi_2 = (2\pi\nu(t + \tau)(t + \tau) + \varphi(t + \tau))$$

According to equations 2-27 and 2-28, the phase difference  $\phi_2 - \phi_1$  governs the behavior of  $i_{RF}(t)$ . From this phase difference arise four terms:

$$\phi_2 - \phi_1 = 2\pi[\nu(t + \tau) - \nu(t)]t + 2\pi\nu(t + \tau)\tau + \varphi(t + \tau) - \varphi(t) \quad (2-29)$$

As mentioned by Kovács in [18], the emitting wavelengths  $\lambda$  must be much smaller than the fiber length difference  $\Delta L$  of the MZI ( $\lambda \ll \Delta L$ ), otherwise, the MZI would behave as a standard interferometer. In other words, the time delay  $\tau$  imposed in one of the interferometer's arms must be much greater than the laser's coherence time  $\tau_c$  [48], so the resulting phase will not cause a constructive or destructive interference. That being said, for  $\tau \gg \tau_c$ , the phase difference  $\varphi(t + \tau) - \varphi(t)$  in equation 2-29 can be neglected. Also, the first term,  $2\pi[\nu(t + \tau) - \nu(t)]t$ , is much smaller than the second,  $2\pi\nu(t + \tau)\tau$ , thus, one can write the generated photocurrent as [11]:

$$i_{RF}(t) = \mathfrak{R} P_L [1 + \cos(2\pi\nu(t + \tau)\tau)] \quad (2-30)$$

If the LD optical frequency varies according to 2-20, the term inside the cosine of equation 2-30 becomes  $\phi = 2\pi\nu_0\tau + 2\pi\alpha_{ch}i_{LD}(t + \tau)\tau$ . As  $i_{LD}(t + \tau)$  varies in the same way of  $i_{LD}(t)$ , one can omit the  $\tau$  without loss of generality. Thus, the first term of  $\phi$  is only a constant phase, but the second term results in an oscillating frequency of:

$$f_{RF}(t) = \frac{1}{2\pi} \frac{d\phi(t)}{dt} = \alpha_{ch}\tau \frac{di_{LD}(t)}{dt} \quad (2-31)$$

By comparing 2-31 with 2-24, the equivalence between  $t_0$  and  $\tau$  is observed, and, in the self-heterodyning technique,  $\tau$  is generated by using an unbalanced interferometer.

If a linear RF chirp is desired, assuming  $\alpha_{ch}$  constant, a quadratic dependence on the laser current must be imposed:

$$i_{LD}(t) = at^2 + bt + I_b, \quad (2-32)$$

where  $a$  and  $b$  stand for modulation current parameters. By performing the time derivative, a linearly chirped radio frequency is achieved, given by:

$$f_{RF}(t) = \alpha_{ch}\tau[2at + b] \quad (2-33)$$

### 2.3.4

#### Tradeoff and optimization of bandwidth and TBWP

It has been observed [46] that there is a tradeoff between the bandwidth (BW) and TBWP parameters. Therefore, this section investigates the conditions for maximum achievable TBWP or, alternatively, maximum BW, by assuming a parabolic shape for the LD modulating current as described by 2-32 with  $b = 0$ .

Fig. 2.15 shows two delayed replicas of the LD optical output frequency  $\nu(t)$ . Because the replicas follow the parabolic shape with  $W$  pulse width, the beating time width,  $W_B$ , is given by:

$$W_B = W - \tau \quad (2-34)$$

As a result, the instantaneous electrical current difference replicas, with  $b = 0$  in 2-32, is given by:

$$\Delta I(t) = a(2\tau t - \tau^2) \quad (2-35)$$

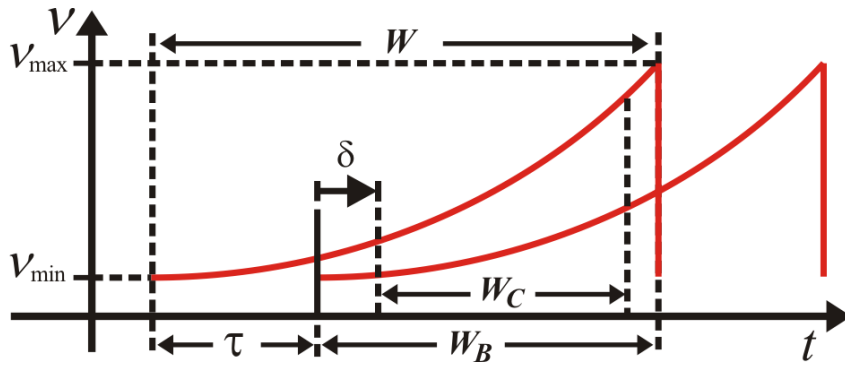


Figure 2.15: Replicas of optical frequency modulated pulses.

From Fig. 2.15, the minimum and maximum differences between currents are obtained at  $t = \tau$  and  $t = W$ , respectively:  $\Delta I_{min} = a\tau^2$  and  $\Delta I_{max} = a(2\tau W - \tau^2)$ . The maximum bandwidth is obtained by the difference between the maximum and the minimum electrical current excursion inside the beating time window:

$$\Delta I_B = \Delta I_{max} - \Delta I_{min} = 2a\tau(W - \tau) \quad (2-36)$$

Because the optical beating occurs in the photodiode, the bandwidth can be calculated from  $BW = \alpha_{ch}\Delta I_B$ , and with the aid of 2-36, it can be written

as:

$$\text{BW}(\tau) = 2a\alpha_{ch}\tau(W - \tau) \quad (2-37)$$

The condition for maximum bandwidth BW can be easily calculated from 2-37, and is given by:

$$\tau = W/2 \quad (2-38)$$

On the other hand TBWP is simply defined as the product of the bandwidth BW with  $W_B$ , which can be written with the aid of 2-34 and 2-37 as:

$$\text{TBWP}(\tau) = \text{BW}(\tau)W_B = 2a\alpha_{ch}\tau(W - \tau)^2 \quad (2-39)$$

The condition for maximum TBWP can also be easily calculated from 2-39, and is given by:

$$\tau = W/3 \quad (2-40)$$

In order to manage the time width of the microwave pulses, it is possible to select an arbitrary slice of  $W_B$  named as chop time  $W_C$ . Once  $W_C < W_B$ , the beating time  $W_B$  in 2-39 should be replaced by  $W_C$ . To maximize BW and TBWP, the condition  $W_C = W_B$  must be fulfilled. Furthermore, an additional time delay  $\delta$  can be added to  $\tau$  with the purpose of placing  $W_C$  within  $W_B$ , hence defining the start and stop frequencies of the microwave pulse. The experimental setup that provides ways to select values of  $W_C$  and  $\delta$ , as well as all other parameters discussed in this section is detailed in chapter 3.

### 3

## Photonic Generation of LFM pulses

The theoretical basis for photonic generation of LFM pulses with high TBWP was discussed in the previous chapter. Here, the conventional self-heterodyning technique is experimentally tested but introducing a delay-optimized interferometer combined with saturated optical amplification to obtain nearly flattened ( $\pm 3$  dB) microwave linearly chirped pulses of up to  $\sim 3.0$   $\mu\text{s}$  duration over a wide range of frequencies (2.0 - 25.2 GHz), with TBWP of  $\sim 68440$ . A spectral-scanning chirp measurement technique is introduced with the major benefit of using the same experimental setup, allowing the DFB-LD chirp characterization. The resulting measurements led to a simple adjustment of the original parabolic modulation waveform by adding a cubic term  $\propto t^3$ , which ensured almost perfectly linear RF chirped pulses within the entire broad spectrum. By adjusting some experimental parameters, an extension to 28.4 GHz with TBWP of  $\sim 74000$  was accomplished, although without chirp linearization. The latter bandwidth (2.0 – 28.4 GHz) encompasses virtually the microwave radar bands S to K. Furthermore, transmission over  $\sim 41$  km long standard optical fiber links is presented without significant distortions.

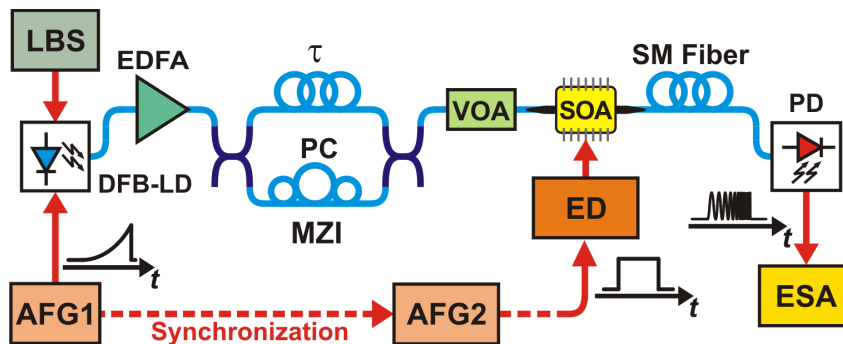
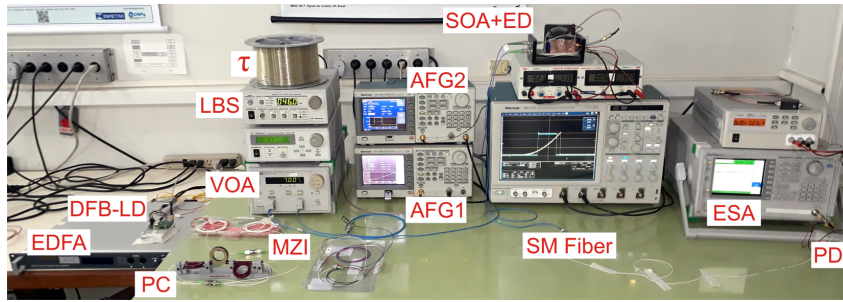
This experiment is of fundamental relevance for the comprehension of the main experiment of this work, which is presented in chapter 4. This chapter is divided as follows. Section 3.1 describes the setup used in the experiment, where a novel form of pulse chop is explained. The spectrum-scanning chirp measurement technique is introduced in section 3.2, while section 3.3 presents the experimental results.

### 3.1

#### Experimental Setup

Fig. 2 shows the experimental self-heterodyning setup, assembled to generate and characterize the chirped microwave pulses in back-to-back (B2B) and after fiber transmission. Parabolic pulses with a low repetition rate (2 kHz) modulate a 1550nm DFB-LD. This modulation is done by an arbitrary function generator (AFG1), which produces voltage pulses with variable amplitude [V] and temporal width  $W$  [ $\mu\text{s}$ ], resulting in a proportional modulating current entering in the laser circuit (20 mA/V for 50  $\Omega$  laser circuit input impedance).

A laser bias source (LBS [21]) guarantees the LD modulation above the threshold, i.e. in its linear regime.



**AFG:** Arbitrary Function Generator, **DFB-LD:** Distributed Feedback Laser Diode  
**ED:** Electronic Driver, **EDFA:** Erbium-Doped Fiber Amplifier, **ESA:** Electrical Spectrum Analyzer, **LBS:** Laser Bias Source, **MZI:** Mach-Zehnder Interferometer,  **$\tau$ :** Optical Fiber Delay Line, **PC:** Polarization Controller, **PD:** Photodiode, **SOA:** Semiconductor Optical Amplifier, **VOA:** Variable Optical Attenuator

Figure 3.1: Experimental setup. Picture of back-to-back configuration (top) and diagram (bottom).

The modulation current duty cycle is kept below 2.0 %, low enough to let laser frequency stabilization before the next modulation pulse. It should be pointed out that the thermal stabilization time for InP based LD was theoretically estimated to be  $\sim 91 \mu\text{s}$  [49]. This information suffices for the purpose of this experiment, but a deeper study on the thermal time constants of the same DFB-LD are discussed in chapter 4. Even so,  $91 \mu\text{s}$  corresponds to a repetition rate of 11 KHz, which is greater than the 2 KHz used in the experiments.

The modulated laser signal is amplified by an erbium-doped fiber amplifier (EDFA), which is running close to saturation so that the main effect of the modulation signal is to control the laser optical frequency while its optical power output is equalized by the amplifier saturation. Although this technique requires a high input power ( $\sim 4 \text{ dBm}$ ) in the EDFA to achieve its saturation, it is much simpler than using a MZM acting as an attenuator as reported in [44], because no synchronism is required for the EDFA,

An unbalanced MZI splits its input optical signal, sets a time delay  $\tau$  in one of the arms, and combines this with the reference arm at its output. A polarization controller (PC) allows maximum beating power generation.

An SOA triggered by AFG2, enables light transmission windows,  $W_C$ , in the 40 ns – 3.1  $\mu$ s range, limited by the available electronic driver (ED). The latter translates square voltage pulses into square current pulses of about 667 mA amplitude, turning the SOA to be both a chopper and a non-saturated amplifier. The transmission windows are synchronized by AFG2 after a time delay equal to  $\tau + \delta$  (see Fig. 2.15). In this way, a desired  $W_C$  within  $W_B$  can be selected. To avoid SOA's nonlinear effects due to high input powers, such as four-wave mixing (FWM) [50], a variable optical attenuator (VOA) must be placed before the amplifier. More on this non-linear effect will be discussed in section 3.3.1.

Note that, however the saturated EDFA represents a clever solution for power equalization and amplification for long distance transmission, an SOA had to be used for chopping the proper portion of the optical pulse, while in [44], the MZM substitutes these two devices, but in a more complex configuration. Nevertheless, it will be seen in section 3.2 that the SOA is the key element for the spectrum-scanning chirp measurement technique, thus, it represents much more than just acting as a chopper device and providing non-saturated amplification.

A standard single-mode fiber (SMF) up to  $\sim 41$  km length is placed linking the SOA output to a 22 GHz @ -3 dB bandwidth photodiode, where the optical beating is performed. Finally, the resulting microwave pulses are conducted to an electrical spectrum analyzer (ESA). All equipment used in the experiment are listed in table 3.1.

Table 3.1: Experimental Equipment

Label on Fig. 3.1	Equipment
AFG1	Arbitrary Function Generators 3251 [51]
AFG2	Arbitrary Function Generators 3021B [51]
DFB-LD	FU-68PDF-5 DFB-LD [19]
ED	Electronic Driver developed at CETUC facilities
EDFA	Erbium Doped Fiber Amplifier 1550nm [52]
ESA	MS2668C Spectrum Analyzer 9kHz-40GHz [53]
LBS	Laser Diode Driver Model 505 [21]
PD	DSC 30S PIN Diodes [54]
SOA	Semiconductor Optical Amplifier - SOA1013SXS [55]
VOA	MN9610B Programmable Optical Attenuator [56]

### 3.2

#### Spectrum-scanning chirp measurement technique

Once generated the microwave pulses, the power flatness can be immediately observed at the ESA. However, a clever measurement method is necessary to determine how the microwave frequency varies with time. Thus, it is essential to relate each generated frequency with a certain time instant,  $f_{RF}(t)$ , in order to measure the linearity of the chirp.

A typical chirp measurement of a microwave pulse can be performed through the Instantaneous Frequency Measurement (IFM) method [57]. A power splitter is used to direct two replicas of the microwave to two transmission lines with different lengths. The transmission lines are connected to a microwave phase discriminator (MPD), which directs the phase difference result to a computer. As the phase difference between the two transmission lines depends on the microwave frequency, it is possible to evaluate the instantaneous frequency from the computed phase differences.

Although the IFM method have shown accurate experimental results for chirp measurements [57], it demands an extra experimental setup composed by a power splitter, transmission lines, high frequency band MPD, and a computer assisted by an analog-to-digital converter (A/D). A clever way to measure the chirp of the microwave generated by the setup of Fig. 3.1 that requires no additional measurement apparatus is presented as follows.

Driving the SOA chopper with narrow pulses gives rise to short microwave pulses with small bandwidths, whereas by widening the pulse width, it broadens both the microwave pulse duration and spectrum. Thus, by narrowing the chopper pulse to its minimum value,  $W_C = 40$  ns, and varying

the chop delay  $\delta$ , it is possible to associate each generated frequency with a correspondent time instant, hence measuring the chirped frequency temporal dependence. This method is here named as *spectrum-scanning chirp measurement technique* (SS-CMT).

Fig. 3.2 shows examples of AFG1 and AFG2 waveforms used in the experiment for LFM microwave waveform generation. On Fig. 3.2a, a large  $W_C$  is used to generate a microwave pulse with large bandwidth. On Fig. 3.2b,  $W_C$  is set to the minimum value of 40 ns for spectrum-scanning chirp measurement.

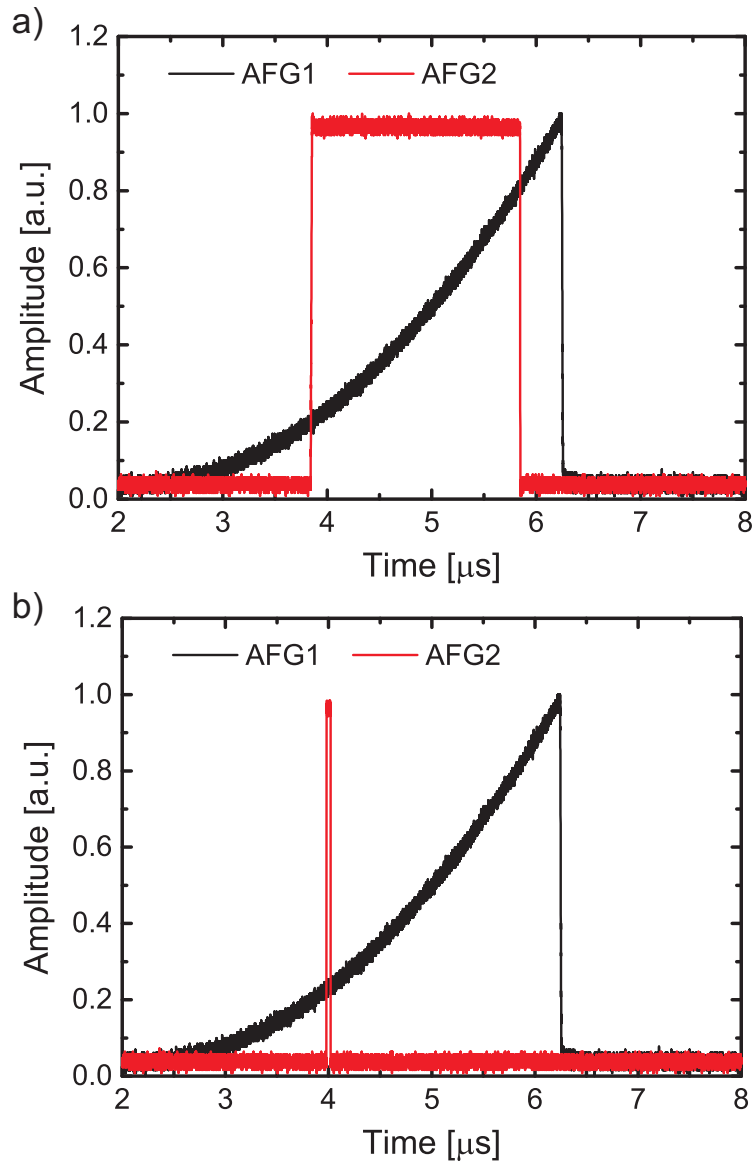


Figure 3.2: AFG1 and AFG2 waveforms for full bandwidth microwave pulse generation (a) and spectrum-scanning chirp measurement (b).

### 3.3

#### Experimental Results

The main parameters of the experiment were set aiming to generate linearly chirped RF pulses. Thus, a quadratic time dependence was imposed by AFG1, generating  $i_{LD}(t) = at^2$ , where "a" is a factor to adjust the peak modulation current ( $\Delta I_{peak}$ ), which was initially set to 183 mA. This value is reached when time  $t = W = 4.60 \mu\text{s}$ . The static bias current, adjusted by LBS, was set to 46 mA, resulting in an effective current excursion from 46 to 229 mA. The delay produced by 308 m fiber length within the MZI corresponds to  $\tau = 1.54 \mu\text{s}$ , causing a maximum beat time of  $W_B = 3.06 \mu\text{s}$ , which is very close to the maximum allowed  $W_C$ . These setup values, however, may vary along the following experiments.

#### 3.3.1

##### Electrical Harmonic Distortions and Phase Noise

A great concern about microwave generation is the spectral purity. As mentioned in section 3.1, optical nonlinearities due to FWM is a consequence of high input powers in the SOA. FWM in the optical domain translates into harmonic distortions (HD) in the resulting RF chirped microwave pulse. Thereby, before analyzing the maximum BW or TBWP that can be achieved with the technique, it is crucial to determine the quality of the generated signals in terms of HD.

By setting  $W_C = 100 \text{ ns}$  and  $\delta = 0.25 \mu\text{s}$ , 500 MHz bandwidth microwave pulses centered around 3.1 GHz are obtained as shown in Fig. 3.3 (top). This spectrum clearly shows a second and third HD for SOA's optical input power of +0.5 dBm. As the optical power decreases the distortions are observed to reduce.

It should be observed that even for the worst case, where  $P_{in} = +0.5 \text{ dBm}$ , the second harmonic component is  $\sim 17.5 \text{ dB}$  ( $< 2\%$ ) below the fundamental. Fig. 3.3 (bottom) shows the power difference between the fundamental and the harmonics as a function of the SOA's optical input power. It is clear that, for -12.5 dBm, only the fundamental frequency is present and it is 30.5 dB above ESA noise level (3 MHz resolution bandwidth). This issue constrains the maximum SOA input mean power at -12.5 dBm, and this value is kept along the experiments. Moreover, the measured SOA output power, corrected by the duty cycle, was 6.5 dBm which demonstrates that the SOA not only acts as a chopper (for full bandwidth pulse generation and chirp measurement), but also as an amplifier with 19 dB gain.

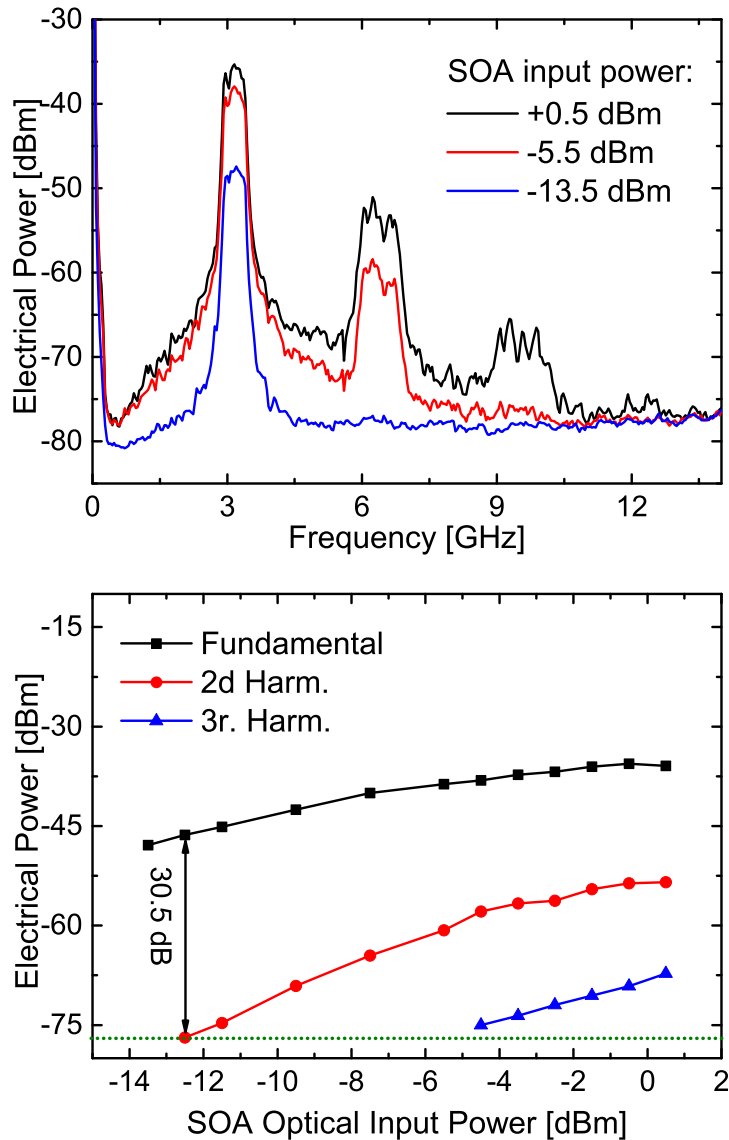


Figure 3.3: Harmonic Distortion measurement of the RF microwave pulse.

Another issue regarding chirped microwave waveforms for radar applications is the required low phase noise, since phase fluctuations result in lower or wider correlation peaks. The linewidth of the DFB-LD used in the experiments has also been characterized. Fig. 3.4 shows the acquired continuous wavelength DFB-LD linewidth, of about 7.9 MHz, employing a delayed self-heterodyning technique (150 MHz beat tone) [48]. Since the same unbalanced (308 m) MZI was used, this characterization also includes the minor phase fluctuation contribution due to environmental interference. However, to circumvent this problem, a narrower linewidth DFB-LD along with techniques to reduce its phase noise in chirping operation [10] could be used for more demanding radar applications.

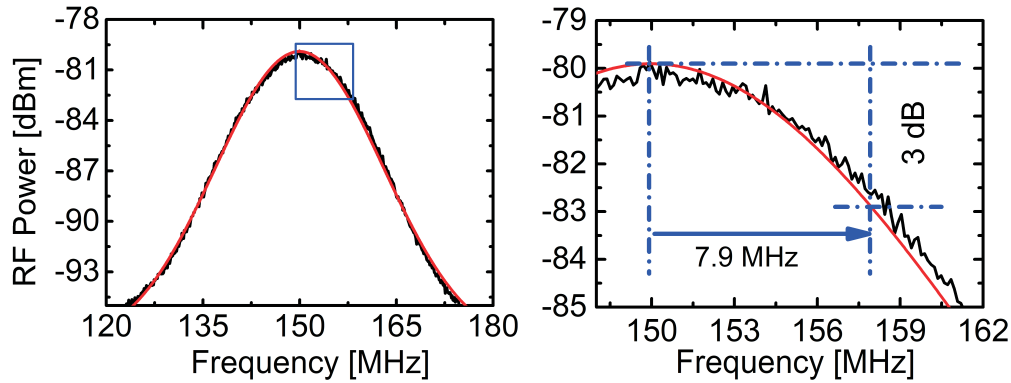


Figure 3.4: DFB-LD linewidth (left) and the inset detail (right). Black curve corresponds to the effective measurement; red curve to the Lorentzian fit.

### 3.3.2 Optimization of TBWP and BW

In order to experimentally verify the theoretical BW and TBWP optimizations outlined in section 2.3.4, a set of different fiber delays ( $\tau$ ) were placed in one of the MZI arms. It should be pointed out that only for this verification, the experimental setup was modified in order not to surpass the photodiode maximum frequency response, nominally around 22 GHz. At first,  $\Delta I_{peak}$  was reduced from 183 mA to 140 mA, with  $I_b = 35$  mA. Second, in order to measure the maximum allowed bandwidth, the condition  $W_C = W_B$  has to be guaranteed. Then, to ensure a sampled beating time  $W_B = W - \tau$  for a limiting case when  $\tau = 0$ , the largest  $W_B$  should be equal to  $W$ . Since  $W_C$  is limited by the ED to  $\sim 3.1 \mu\text{s}$ , the duration of the modulating current waveform pulse was reduced to  $W = 3.1 \mu\text{s}$ . Because of these constraints, a maximum BW of 17 GHz was obtained in this case.

Fig. 3.5 presents the plots of BW and TBWP where a "delay scanning" normalized to  $W$  was performed. In all experimental data points corresponding to each fiber delay, the BW (GHz) and  $W_B$  ( $\mu\text{s}$ ) were measured. In fact, the maximum BW and TBWP could be achieved very close to the theoretical predicted values of  $\tau/W = 0.5$  and 0.33, respectively. Indeed, longer values of  $W$  may lead to wider BWs and larger TBWPs (see equations 2-37 and 2-39). However, for maximum BW or TBWP,  $\tau$  should be re-optimized according to equations 2-38 and 2-40.

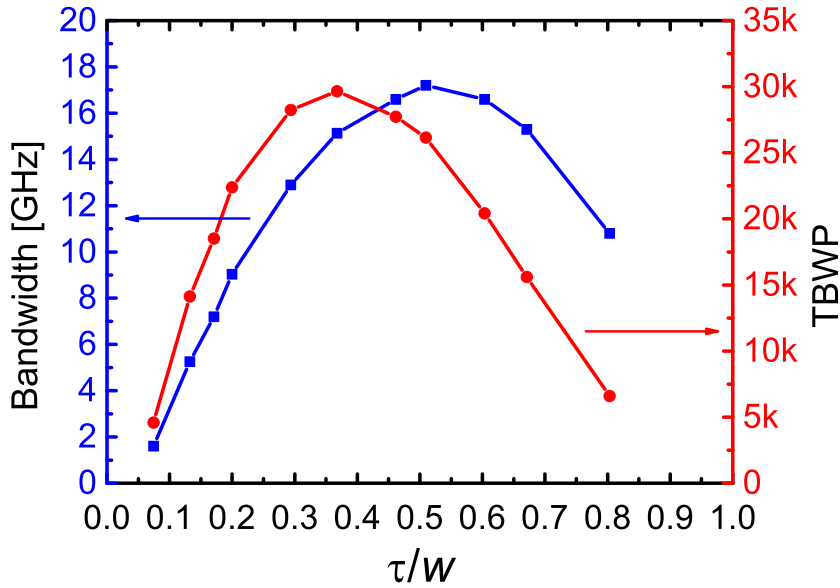


Figure 3.5: The BW (left) and TBWP (right) of the output beating signal as a function of the delay  $\tau$  normalized by the time duration  $W$  of the modulating current waveform ( $\tau/W$ ).

### 3.3.3 Generation and Tuning of Microwave Pulses

As mentioned before, the photodiode used in the experiments has a bandwidth of 22 GHz @ -3 dB, which turns out to be a bottleneck to generate higher RF frequencies. Nevertheless, by keeping the same parameters defined in the introduction of section 3.3 and setting  $W_C$  and  $\delta$  to 2.95 and 0.055  $\mu\text{s}$ , respectively, a 23.2 GHz bandwidth chirped microwave pulse (2 – 25.2 GHz) was generated. These parameters values were used to avoid the edges of the parabolic shaped modulation current. The achieved TBWP is 2.95  $\mu\text{s}$   $\times$  23.2 GHz = 68440.

The versatility of the proposed method allows to select an arbitrary band within the total generated microwave bandwidth. This flexibility is shown in Fig. 3.6, where the standard radar bands S, C, X, Ku and K were selected. About 30 dB signal to noise ratio (SNR) could be measured, which is compatible with the result shown in Fig. 3.3.

Radar band tuning, however, depends on four parameters:  $W$ ,  $\delta$ ,  $W_C$  and  $\Delta I_{peak}$  ( $\tau$  is fixed by the MZI fiber length delay). Therefore, any band and pulse width can be theoretically achieved. Nonetheless, experimental restrictions limit the maximum  $W_C$  to 3.1  $\mu\text{s}$  and the highest  $\Delta I_{peak}$  to 200 mA (available from AFG1). For instance, assuming  $W$  and  $\Delta I_{peak}$  fixed, the bandwidth, central frequency and pulse duration can be selected by means of  $\delta$  and  $W_C$ . In this case, which was used to obtain Fig. 3.6,  $\delta$  defines the initial frequency and

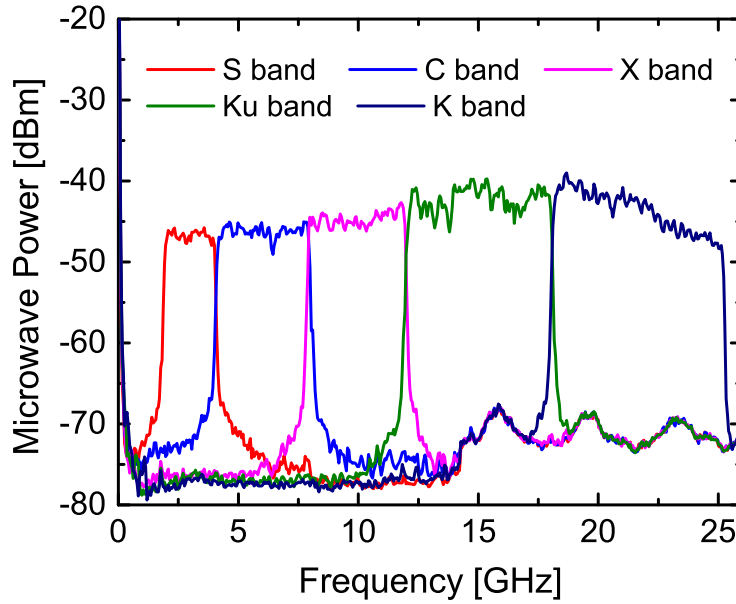


Figure 3.6: Chirped microwave signals in different radar bands. The band is selected by changing the chop time  $W_C$  and delay  $\delta$ .

$W_C$ , which turns to be the pulse width itself, sets the final frequency, hence the bandwidth. Additionally, variations of  $W$  and  $\Delta I_{peak}$  can also be set. A greater  $W$ , although allowing wider  $W_C$  values, also reduces the maximum achievable bandwidth for the same  $\Delta I_{peak}$ . Finally, lower values of  $\Delta I_{peak}$  also reduce the maximum bandwidth, but this has no impact on the pulse width.

Spectrum flatness for S, C and X bands is better than  $\pm 1$ dB, whereas for the Ku and K bands it is limited to  $\pm 3$ dB, which is the flatness of the full spectrum. This power variation can be partly attributed to the incomplete saturation of the EDFA, which is responsible for the power increase along the 2 - 20 GHz range; and the bandwidth-limited response of the photodiode above 22 GHz. Note that the noise floor in Ku and K bands is 25 dB below the microwave signal, so that its fluctuations has no influence over the spectrum flatness.

An example of a microwave waveform is shown in Fig. 3.7. In this case an RF signal with pulse width of  $0.270 \mu\text{s}$  ( $W_C$ ) was generated. Due to the available oscilloscope bandwidth (3.5 GHz) the band was limited to 2 - 3.5 GHz range.

Exploring the maximum conditions achievable with the experimental setup,  $\Delta I_{peak}$  was increased to 200 mA, whereas  $I_b$  was decreased to 31 mA whilst keeping  $W$  and  $\tau$  unchanged. Since the frequency spectrum reached beyond the -3dB detector bandwidth,  $W_C$  was slightly shortened to  $2.8 \mu\text{s}$  in order to keep the detected SNR above 15 dB. Fig. 3.8 shows the resulting

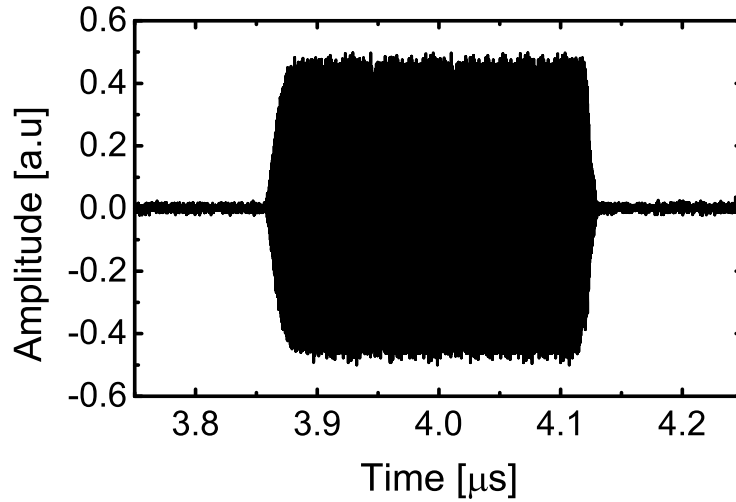


Figure 3.7: Microwave waveform signal (2–3.5 GHz) generated for a short  $W_C$ .

output spectrum where the TBWP is  $26.4 \text{ GHz} \times 2.8 \text{ } \mu\text{s} \approx 74000$ . This is a twofold improvement over the best TBWP obtained with the self-heterodyning technique [46].

As mentioned in section 2.1.3, a high TBWP value is interesting for radars systems because it represents the equipment's pulse compression ratio. The range resolution for a chirped signal defined in equation 2-13 can be rewritten as a function of the TBWP by:

$$R_{r \text{ chirp}} = \frac{c_0}{2\Delta f} = \frac{c_0 \cdot T}{2 \text{TBWP}} \quad (3-1)$$

As the range resolution of a chirped pulse is inversely proportional to the TBWP, it can be made virtually very small. For the improved TBWP case of 74000, a theoretical range resolution of 5.7 mm was found. However, microwave electronics circuitry limits practical implementations for such large bandwidths and pulse compression. Dual-band techniques (or eventually multi-band) proposed for radar systems [58] can be used to manage such kind of chirped pulses.

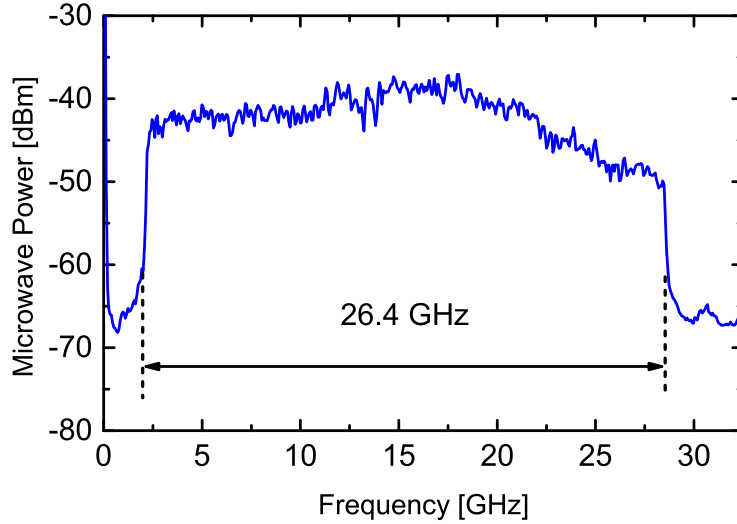


Figure 3.8: Photonic generated microwave spectrum corresponding to 74000 of TBWP.

### 3.3.4 RF Chirp Linearization

For RF chirp analysis, the 2 to 25.2 GHz bandwidth case was considered. To observe the frequency chirp,  $W_C$  was reduced to 100 ns and the central frequency of the generated microwave pulse was then measured as the chop delay  $\delta$  was increased along the beat time  $W_B$ , i.e., the spectral-scanning chirp measurement technique was employed. The result is displayed in Fig. 3.9 for B2B and after transmission through  $\sim 41$  km of SMF, where an approximate linearity may be assumed within bandwidths lower than 4 GHz, but fails in wider bandwidths. This demonstrates that the LD chirp parameter,  $\alpha_{ch}$ , is not constant for large amplitude modulation currents, so that some correction must be applied in the modulation function to impose microwave chirp linearity.

By fitting the frequency dependence with a second order polynomial function, we conclude that a third order correction in  $i_{LD}(t)$  would be the simplest solution to reduce the nonlinearity. The modulation function was then empirically adjusted with a third order term,  $i_{LD}(t) = a(t^2 - 0.07t^3)$ . This new function, however, produces a different bandwidth, because the negative correction term reflects in a smoother increase compared to the single quadratic term. Therefore, to keep the 2 to 25.2 GHz bandwidth,  $\Delta I_{peak}$  was adjusted from 183 to 192 mA and the bias current to 31 mA. The practically linear chirp obtained is displayed in Fig. 3.10. It also shows that even after  $\sim 41$  km fiber propagation, the chirp dependence of the signal is kept unchanged despite the linearization adjustment.

From Fig. 3.10, an average chirp rate of 7.8 GHz/ $\mu$ s can be evaluated. Thus, for 192 mA current variation, an average chirp parameter of  $\sim 0.13$

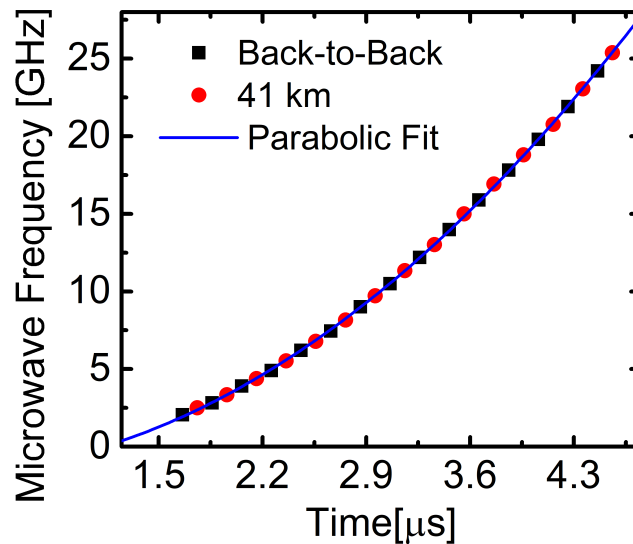


Figure 3.9: Chirp measurement of a non-linearized chirped microwave signal through spectrum-scanning technique before and after transmission along 41 km standard singlemode fiber.

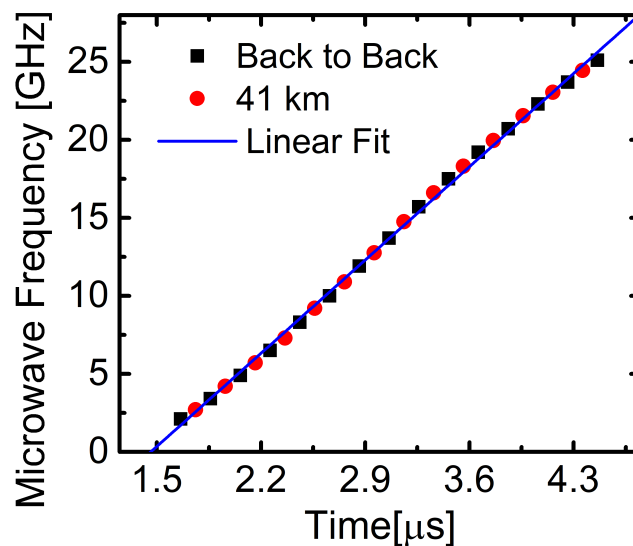


Figure 3.10: Chirp measurement of a linearized chirped microwave signal through spectrum-scanning technique before and after transmission along 41 km standard singlemode fiber.

GHz/mA could be calculated, and is compatible with the 0.9 GHz/mA measured for the same laser diode but in the static regime (thermal chirp measurement).

To acquire the linearized spectrum, the SOA chopper pulse was again widened to 2.95  $\mu$ s. The resulting microwave pulse spectrum is shown in Fig. 3.11, before (B2B) and after propagation through 25 and 41 km of SMF. Note that the TBWP is kept on 68440.

Since the noise floor is at -80 dBm level, a reduction in the SNR is observed when transmitting through several kilometers of fiber. Therefore, the

only impact caused by fiber inclusion is power decay, proportional to the fiber and connector losses. Fiber dispersion, however, has to be analyzed. By using the widest spectrum width of  $\Delta f = 26.4$  GHz as given by our measurement result in Fig. 3.8, the corresponding wavelength band of  $\Delta\lambda = 0.21$  nm is calculated for a central wavelength of  $\lambda_C = 1546$  nm. Assuming the chromatic dispersion parameter  $D = 17$  ps/nm·km, and the optical fiber length  $L = 41$  km, yields  $\Delta T = 146$  ps, a negligible value when compared to the  $4.6 \mu\text{s}$  time width of the light pulses.

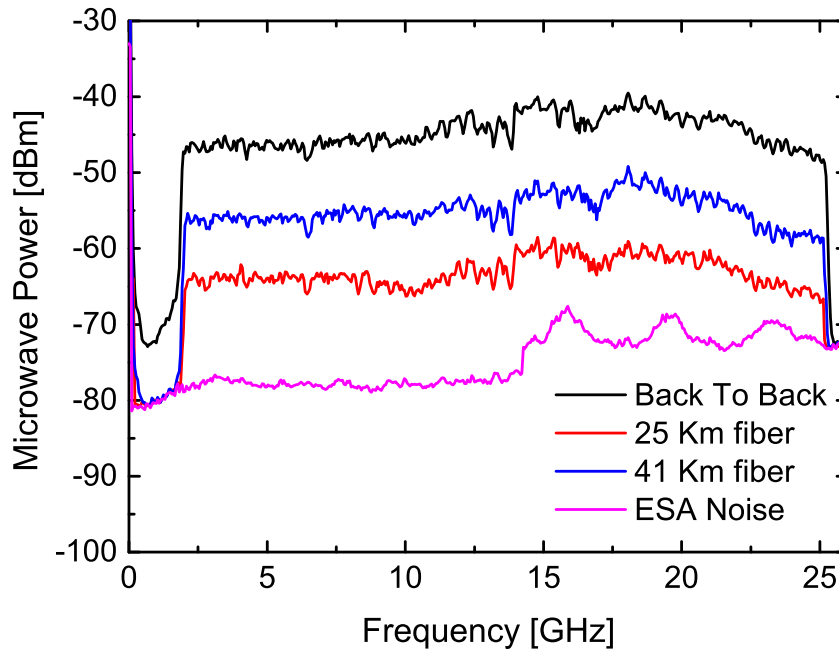


Figure 3.11: Linearized beating frequency chirp before (B2B) and after transmission along 25 and 41 km standard single-mode fiber.

## 4

### Photonic Generation of NLFM pulses

Last chapter has shown the use of self-heterodyning technique to generate highly linear microwave chirped pulses with large TBWP. As well founded in section 2.1, LFM pulses with high TBWP yield better resolution for radar systems, though almost no change is observed in terms of PSLR when compared to low TBWP pulses. To improve the peak to side lobe ratio, NLFM pulses should be used.

The challenge at this point is to generate NLFM pulses by means of the self-heterodyning technique. To the author's best knowledge, there has been no attempt to do so, which augments the level of the challenge and serves as a huge motivation for the work. One could argue that to obtain an NLFM pulse through self-heterodyning technique it suffices to know the function that governs the time-dependence of the frequency for the desired NLFM pulse, for instance the one shown in Fig. 2.8a, then use the integral of this function to modulate the DFB-LD. In such a way, after a fiber time delay  $\tau$  and optical beating at the photodetector, the NLFM pulse would be generated. Unfortunately, this simple approach does not lead to NLFM pulses because the relation between the injected current in the DFB-LD and the emitting optical frequency is not linear. This phenomenon was observed in section 3.3.4, where a current correction by a cubic term was necessary for chirp linearization.

The idea to approach the problem of a non-linear relation between the DFB-LD injected current and the emitting optical frequency was to characterize the DFB-LD chirp as a Linear Time-Invariant (LTI) system, where the injected current  $i(t)$  is the input, and the emitting optical frequency  $\nu(t)$  is the output. Note that a non-linear relation between two quantities, say  $x(t)$  and  $y(t)$ , means that  $y(t)$  cannot be written as  $\alpha x(t)$ , where  $\alpha \in \mathbb{R}$ ; but it does not mean that there is not a linear mapping between the spaces  $X$  and  $Y$ , where  $x(t)$  and  $y(t)$  are inserted, respectively.

By cleverly measuring  $\nu(t)$  for a simple current input, one could calculate the LTI system's transfer function and hence, with the aid of a numerical simulation, discover the current input necessary to generate the desired  $\nu(t)$  that will result in an NLFM pulse after delayed self-heterodyning. In fact, any arbitrary chirped microwave could be generated in theory, but it will be seen

in this chapter that the technique has some physical limitations that preclude the generation of certain types of chirped microwave waveforms.

This chapter details the aforementioned method and it is organized as follows. Section 4.1 describes the experimental setup used for generation of NLFM pulses. Next, it is introduced in section 4.2 the time-resolved optical spectroscopy technique, which was used to measure the instantaneous emitting optical frequency as a function of time,  $\nu(t)$ , for a simple step current input. The mathematical modelling of the DFB-LD chirp as an LTI system, as well as the validation of the linearity and time invariance requirements are described in section 4.3. The numerical simulation developed after the mathematical modelling, its results and the limitations of the technique are presented in section 4.4, while section 4.5 shows the experimental results.

#### 4.1 Experimental Setup

Fig. 4.1 shows schematically the experimental setup assembled for the generation and characterization of time dependent frequency  $f_{RF}(t)$  of arbitrary shaped microwave pulses using the self-heterodyning technique. This setup is very similar to the one presented in Fig. 3.1, though two minor differences are observed: the format of the pulses generated by AFG1 is not parabolic any more; and the transmission through a 41 km fiber is not present since it is out of the scope of this experiment.

The specially shaped voltage pulses with duration  $W$  (few  $\mu\text{s}$ ) are generated with a low repetition rate of 0.33 kHz by AFG1, resulting in a proportional modulating current driving the 1550 nm DFB-LD circuit. Aside from AFG1, the other components DFB-LD, LBS, AFG2, EDFA, SOA, ED, ESA perform in the same way as described in sections 3.1 and 3.2, and also, the same exact equipment were used in this experiment, so table 3.1 is still valid for equipment reference.

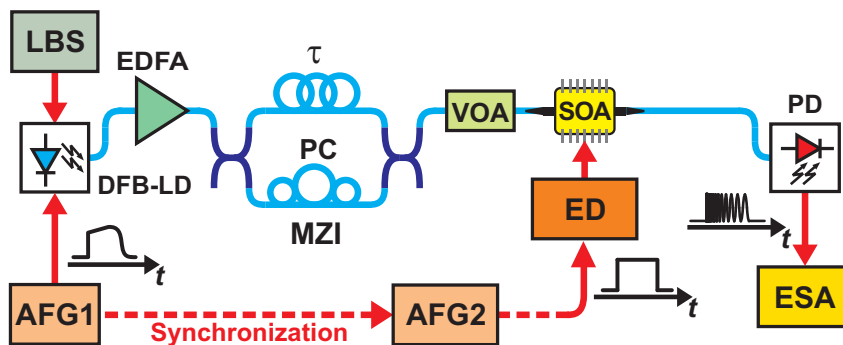


Figure 4.1: The self-heterodyne experimental setup.

The experimental setup of Fig. 4.1 does not add novel information regarding the self-heterodyning technique. However, as will be discussed in the following sections, the specially shaped voltage pulses from AFG1 that modulate the DFB-LD in this experimental setup will be the major responsible for generating NLFM microwave pulses.

## 4.2 Time-Resolved Optical Spectroscopy

Although the setup of Fig. 4.1 shows useful for generation and characterization of the NLFM pulses, a different setup is necessary to measure the emitting optical frequency as a function of time, i.e., to measure  $\nu(t)$ . Fig. 4.2 shows the optical spectrum-scanning setup to characterize the optical frequency response as a function of current variation. This configuration uses the same concept of SS-CMT as explained in section 3.2, but instead of using an ESA to measure the electrical frequency, a high resolution (0.16 pm) optical spectrum analyser (HR-OSA) [59] measures the optical frequency.

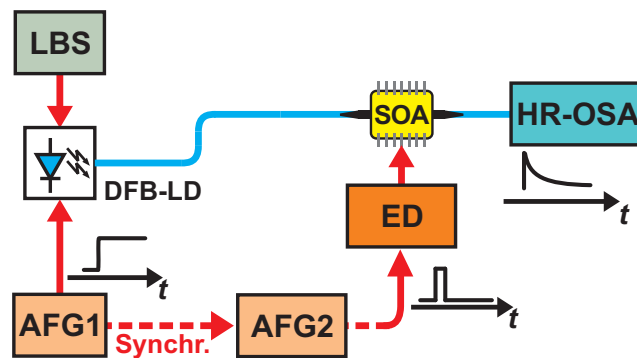


Figure 4.2: Optical spectrum-time scanning setup for Time-Resolved Optical Spectroscopy by using a High Resolution Optical Spectrum Analyzer.

The optical spectrum scanning depends on  $W_C$ . Note that the same  $W_C$  will produce different spectral bands depending on the optical frequency variation rate, i.e., a fast optical frequency variation will produce wider bands within the same  $W_C$ , whereas a slow variation will produce a narrower band. This is shown in Fig. 4.3 where the DFB-LD frequency response to a step modulation current is performed. The choice of a step function is further explained in section 4.3.

Fig. 4.3 (top) and (bottom) shows four time delayed chop windows synchronized along a current step and their corresponding measured spectral bands, respectively. It should be pointed out that 100  $\mu$ s square current pulses with a low repetition rate (0.33 kHz) were used instead of an ideal step current. However, the low modulation duty cycle of 3.3% is low enough to let the laser

frequency stabilize before the next modulation pulse ( $\sim 91 \mu\text{s}$  for thermal stabilization according to section 3.1).

The expected time dependence of the optical frequency to an input current step is an almost immediate ( $\sim$  tens of ps) blue shift arising from the carrier density effect (dynamic chirp), followed by a much slower red shift due to thermal effects (thermal chirp). Hence, proper characterization of the time dependent optical frequency requires a proficient method for data acquisition, knowing that the minimum chop window is about 40 ns.

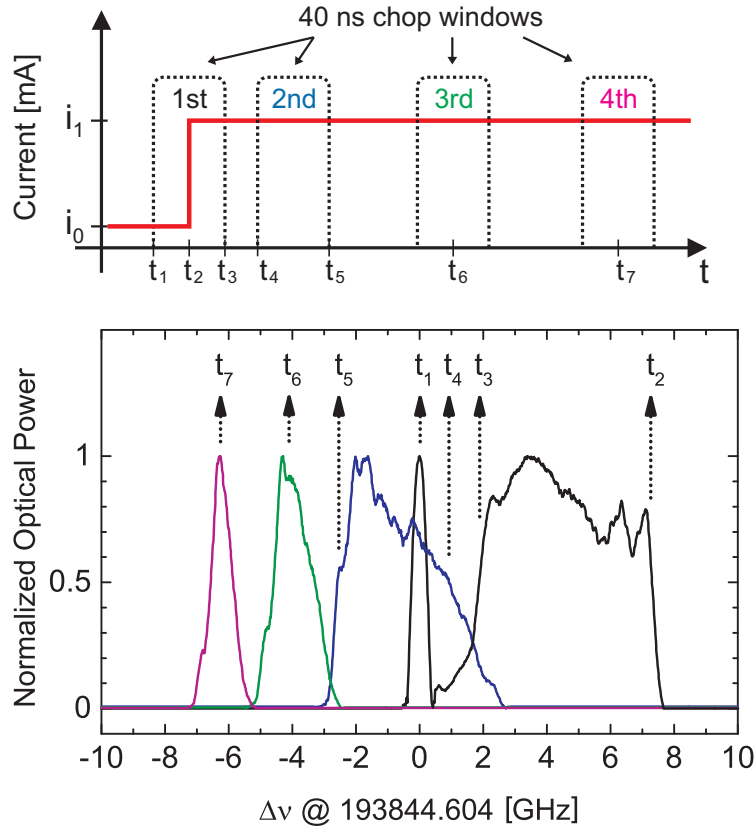


Figure 4.3: Optical spectrum-time scanning acquisition for a step input current feeding a DFB-LD. Top panel: input current and chop windows; Bottom panel: normalized optical power measured at high-resolution optical spectrum analyzer.

The frequency response acquisition is done as follows. The measurement starts by delaying the chop window  $W_C$  such that the current step occurs at the window midpoint  $t_2$ . During the first half of the chop window the initial optical frequency is  $\nu_0 = 193844.604 \text{ GHz}$ , which corresponds to the injected bias current  $i_0$ . At  $t_2$ , when the current step occurs, a sudden blue-shift of about  $+7.2 \text{ GHz}$  is observed, followed by a fast frequency decrease until  $+1.8 \text{ GHz}$  at  $t_3$ . Delaying the chop window to start at  $t_4$ , the decrease in optical frequency slows down extending from a blue shift  $+1.0 \text{ GHz}$  at  $t_4$  to a red shift  $-2.5 \text{ GHz}$  at  $t_5$ . In the next third and fourth time delayed chop windows the chirp is

small enough to consider only the optical frequency at the window midpoint, -4.1 GHz at  $t_6$ , and -6.2 GHz, at  $t_7$ , respectively. The optical frequency was measured at the window midpoint for further delays up to 50  $\mu\text{s}$ .

The acquisition procedure described above was performed for a square modulation current pulse from  $i_0 = 20$  to  $i_1 = 80$  mA. The measured current input and its spectrum response are presented in Fig. 4.4 (top) and (bottom), respectively. As expected, a blue shift is observed at the pulse rise, and a red shift governed by thermal effects is observed throughout the rest of the pulse.

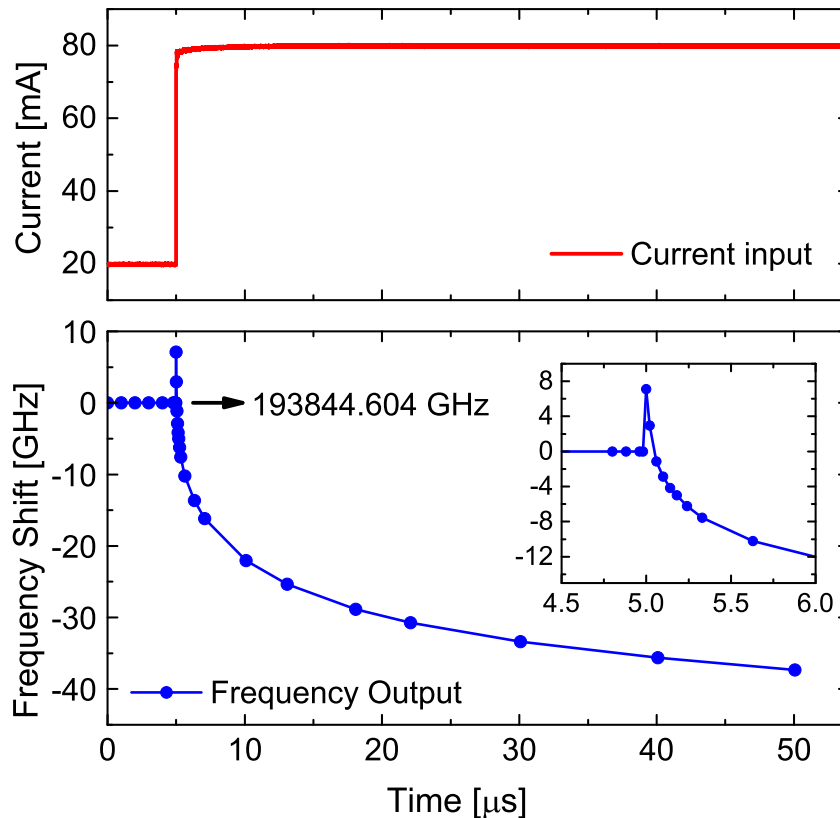


Figure 4.4: DFB-LD Frequency response to a step modulation current. The in-set shows a detailed optical frequency shifts near the pulse step edge.

Though not plotted in Fig. 4.4, the measured optical frequency at the end of the pulse (at 100  $\mu\text{s}$ ) was 193802 GHz, which is still above the expected value of 193781 GHz according to the thermal chirp measurement of Fig. 2.10. The reason for this 21 GHz difference is twofold: first, despite the theoretical  $\sim 91$   $\mu\text{s}$  necessary for laser stabilization, 100  $\mu\text{s}$  was still not enough time for a complete thermal stabilization; second, when the DFB-LD is under pulse modulation, its average temperature increases, what also changes the emitting optical frequency. The latter effect is more relevant when the duty cycle gets higher, so the former effect governs the optical frequency under the 0.33 kHz repetition rate. In order to quantify the overall frequency shift, the optical

frequency at the end of 100  $\mu\text{s}$  modulation pulses was measured for pulse amplitudes varying from 20 to 96 mA. The measurement result is shown in Fig. 4.5, which also displays the thermal chirp measurement for comparison.

From the results shown in Figs. 4.4 and 4.5, it is evident that there are time constants related to the thermal stabilization time of DFB-LDs. These time constants are a fundamental part of the DFB-LD chirp modelling, which will be discussed in the next section.

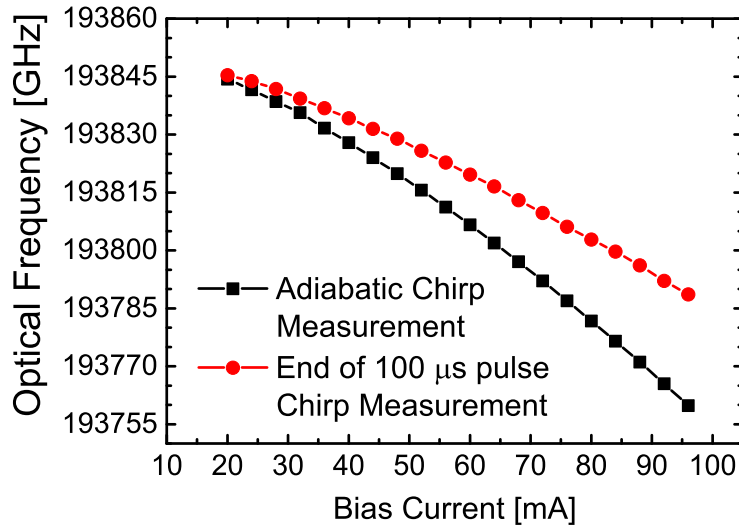


Figure 4.5: Comparison between the thermal chirp and the chirp measured at the end of a 100  $\mu\text{s}$  pulse with a repetition rate of 0.33 kHz.

### 4.3 Laser chirp modelling

It is well known that any linear time-invariant system can be modelled by its corresponding transfer function. In this section, the DFB-LD chirp is modelled as an LTI system for electric current,  $i(t)$ , as the input, and optical frequency,  $\nu(t)$ , as the output. In theory, once identified the laser's transfer function,  $H(s)$ , any arbitrary  $\nu(t)$  could be achieved by simple dividing  $N(s)/H(s)$  to obtain the necessary input  $i(t)$ , which in turn generates the desired  $\nu(t)$ , where  $N(s) = \mathcal{L}\{\nu(t)\}$ .

A step current function is used as the stimulus for transfer function determination. Note that a step function contains high and low frequency components, which are ideal for the characterization of dynamic and thermal effects, respectively. Also, the step function has a simple Laplace Transform and, as shown in Fig. 4.4, its response can be easily measured through the time-resolved optical spectroscopy technique.

The relaxed state of the DFB-LD is assumed to be biased at 20 mA, which is above the threshold current  $I_{th}$  of 18 mA. Hence, for simulation purposes, the inputs were current variations above 20 mA (or  $\Delta i$ ). Similarly, the outputs were the optical frequency variations (or  $\Delta\nu$ ) with respect to 193844.604 GHz, which, from Fig. 4.4, is the output optical frequency in a continuous-wave condition for the 20 mA injected current.

Assuming that the current variation of Fig. 4.4,  $\Delta i = 80 - 20 = 60$  mA, occurred at  $t = 0 \mu s$ , then the output optical frequency would be the curve in Fig. 4.4 (bottom), but left shifted in time by  $\sim 5 \mu s$ . Both the time-domain and Laplace transform of the input step function are known to be:  $\Delta i(t) = 60 \cdot \text{step}(t)$  and  $\Delta I(s) = 60 s^{-1}$ , respectively. To calculate the Laplace transform of the output, first, the optical frequency variations,  $\Delta\nu$ , were fitted from 4.4 with exponentials to find  $\Delta\nu(t)$ . Three exponentials were necessary for a curve fit with a reduced chi-squared error of  $\sim 1\%$ :

$$\Delta\nu(t) = A_1 e^{-t/\tau_1} + A_2 e^{-t/\tau_2} + A_3 e^{-t/\tau_3} + \Delta\nu_0 \quad (4-1)$$

The shortest time constant found,  $\tau_1 = 53$  ns, corresponds to the fast thermal effect at the DFB-LD chip junction. The other two,  $\tau_2 = 1.2 \mu s$  and  $\tau_3 = 16.1 \mu s$  are related to the temperature response time of the substrate and of the laser submount, respectively. The Laplace transform of the optical frequency variations is:

$$\Delta N(s) = \frac{A_1}{s + 1/\tau_1} + \frac{A_2}{s + 1/\tau_2} + \frac{A_3}{s + 1/\tau_3} + \frac{\Delta\nu_0}{s} \quad (4-2)$$

In equations 4-1 and 4-2,  $A_1$ ,  $A_2$  and  $A_3$  were found to be 12.5, 21.8 and 10.7 GHz respectively, while  $\Delta\nu_0 = -38.3$  GHz. With knowledge on  $\Delta N(s)$  and  $\Delta I(s)$ ,  $H(s)$  was calculated:

$$\begin{aligned} H(s) &= \frac{\Delta N(s)}{\Delta I(s)} \\ &= \frac{2.27 s^3 - 15.08 s^2 - 84.86 s - 10.84}{s^3 + 18.52 s^2 + 14.81 s + 0.85} \end{aligned} \quad (4-3)$$

At this point, it is important to identify if the system is linear and time-invariant, otherwise this transfer function could not be used as a tool for generation of arbitrary chirped microwaves. One way to validate the properties of linearity and time-invariance of a system is to verify if the same transfer function is found for two different inputs/outputs. This validation method was applied using a different step current as the input.

The step input current used for LTI validation rise from 20 to 50 mA, ( $\Delta i = 30$  mA). Again, the time-resolved optical spectroscopy method was used for

the measurement of  $\nu(t)$ . The measurement result is plotted in Fig. 4.6 together with previous result of  $\Delta i = 60$  mA for comparison purpose.

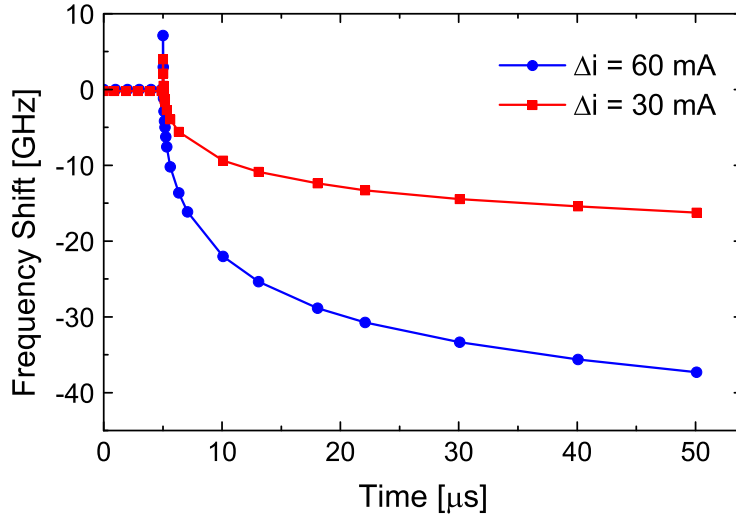


Figure 4.6: Comparison between two instantaneous frequency drift originated from two different step input modulation currents:  $\Delta i = 60$  mA (blue);  $\Delta i = 30$  mA (red).

From the result of Fig. 4.6, it is interesting to notice that a higher current variation implied in both a higher blue shift at pulse rise, and a higher red shift throughout the pulse, thus, reaching a lower optical frequency at  $t = 50$   $\mu$ s. Nevertheless, the fit of the red curve in Fig. 4.6 also resulted in a function of three exponentials, which were used to calculate a new transfer function  $H_2(s)$ , which is displayed in equation 4-4.

$$H_2(s) = \frac{2.57 s^3 - 11.16 s^2 - 78.15 s - 10.2}{s^3 + 18.53 s^2 + 16.22 s + 0.91} \quad (4-4)$$

By comparing the results of equations 4-3 and 4-4, despite some minor differences originated from measurement approximation errors, it is reasonable to assume that  $H_2(s) \approx H(s)$ , therefore, the DFB-LD chirp system can be considered as LTI.

#### 4.4 System Simulation

The knowledge on  $H(s)$ , presented in equation 4-3, represents theoretically the capacity to generate any desired  $\nu(t)$ , and hence, any arbitrary chirped microwave pulse could be obtained through self-heterodyning. Unfortunately, there are some physical restraints that limit this arbitrariness to a minor group of possibilities. The reason for this limitation is given by the lasers' time con-

stants, which slow down a fast conversion of current into optical frequency. Thereby, a too fast and large chirp ( $\sim$  tens GHz/ $\mu$ s) would demand an extremely high current to compensate  $\tau_1$ ,  $\tau_2$  and  $\tau_3$ , which would cause permanent damage to the laser diode.

This limitation can be better understood by examining Figs. 4.7 and 4.8, where  $H(s)$  was used in a numerical simulation to find the necessary  $i(t)$  for a parabolic and linear output optical chirp, respectively. These waveforms were selected by taking into account that  $\nu(t)$  will be used in a self-heterodyne scheme with a time-delay  $\tau$  to generate  $f_{RF}(t)$ , which, for a parabolic  $\nu(t)$  results in a linearly chirped microwave, and for a linear  $\nu(t)$ , results in a microwave tone. The parabolic and linear outputs were written as  $at^2$  and  $at$ , and the parameter  $a$  was selected as follows. For the parabolic optical chirp, the expression  $at^2 - a(t - \tau)^2$  dictates the linear growth of  $f_{RF}(t)$ , and it can be easily reduced to:

$$2a\tau t - a\tau^2. \quad (4-5)$$

The term on the right of 4-5 is a constant term, while  $2a\tau$  is the function's slope. Four linear chirp cases were selected for the slope of  $f_{RF}(t)$ : 1, 2, 5 and 10 GHz/ $\mu$ s, which, for the same  $\tau$  of  $\sim 1.5 \mu$ s used in section 3.3, demands  $a = 1/3, 2/3, 5/3$  and  $10/3$  GHz/ $\mu$ s, respectively. The chosen output,  $\Delta\nu(t)$ , is plotted in Fig. 4.7a, and the obtained input,  $\Delta i(t)$ , is plotted in Fig. 4.7b.

The same procedure was employed for the linear optical chirp scenario, where the frequency of the microwave tone is straightforwardly determined by the product  $a \cdot \tau$ . Again, four cases were selected for the generated microwave tones: 1, 2, 5 and 10 GHz, corresponding to  $a = 1/1.5, 2/1.5, 5/1.5$  and  $10/1.5$  GHz/ $\mu$ s, respectively. Figs. 4.8a shows the chosen output,  $\Delta\nu(t)$ , and Fig. 4.8b shows the obtained input  $\Delta i(t)$ .

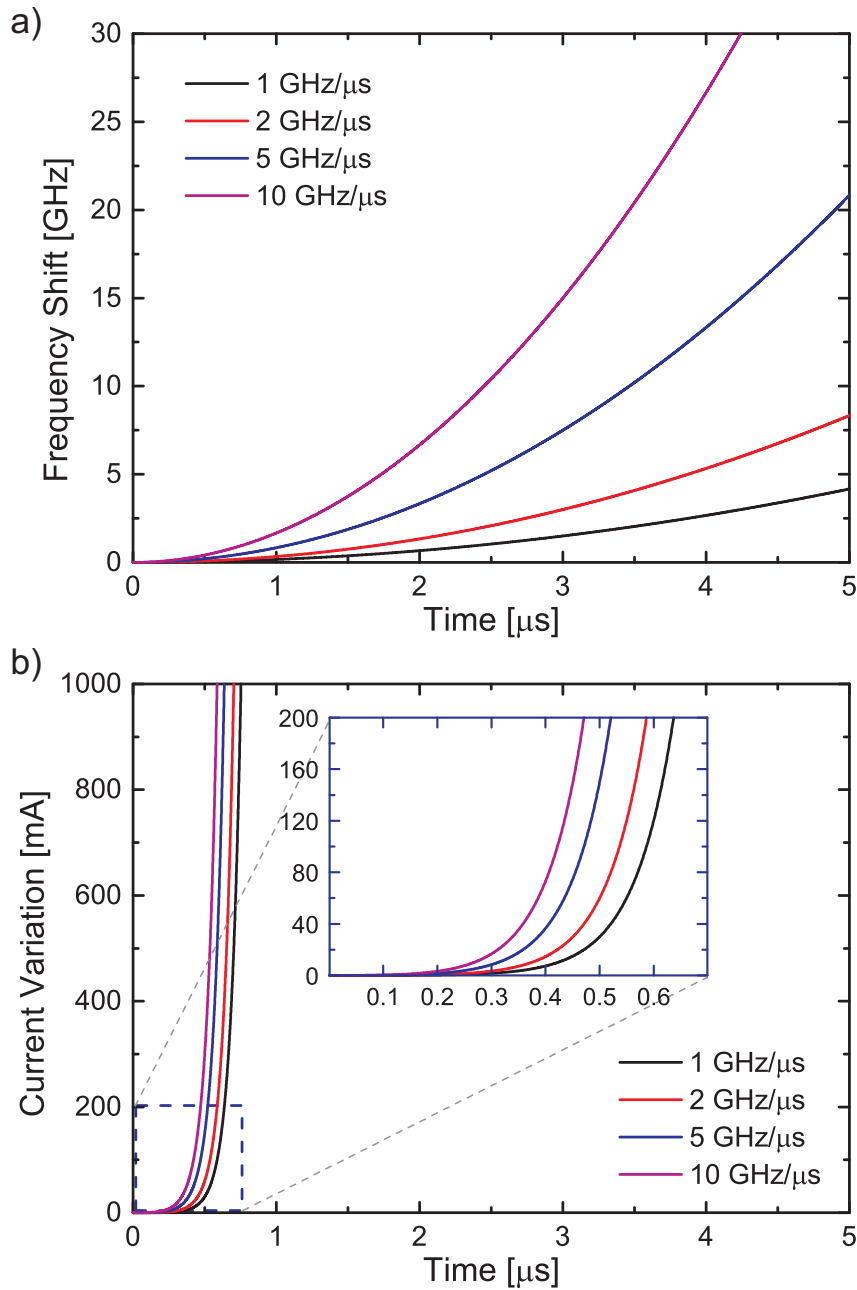


Figure 4.7: Simulation results of the obtained current inputs (b) required for the parabolic optical chirp outputs (a). As the self-heterodyne beating ( $\tau = 1.5\mu\text{s}$ ) of parabolic optical chirp signals originates LFM microwave waveforms with chirp rate depending on the parabola slope, four chirp rates ( $\propto$  parabola slope) were analysed: 1, 2, 5 and 10 GHz/ $\mu\text{s}$ .

According to Figs. 4.7 and 4.8, to generate a linear or parabolic chirp along 5  $\mu\text{s}$ , a huge amount of current is required. Note that, the current variations reached 1 A before 1  $\mu\text{s}$  for both scenarios, which is a much higher current than the maximum operating current of 130 mA recommended by the DFB-LD datasheet [19]. This effect is a result of the slow time constants of the DFB-LD, which retard the conversion of injected current into optical

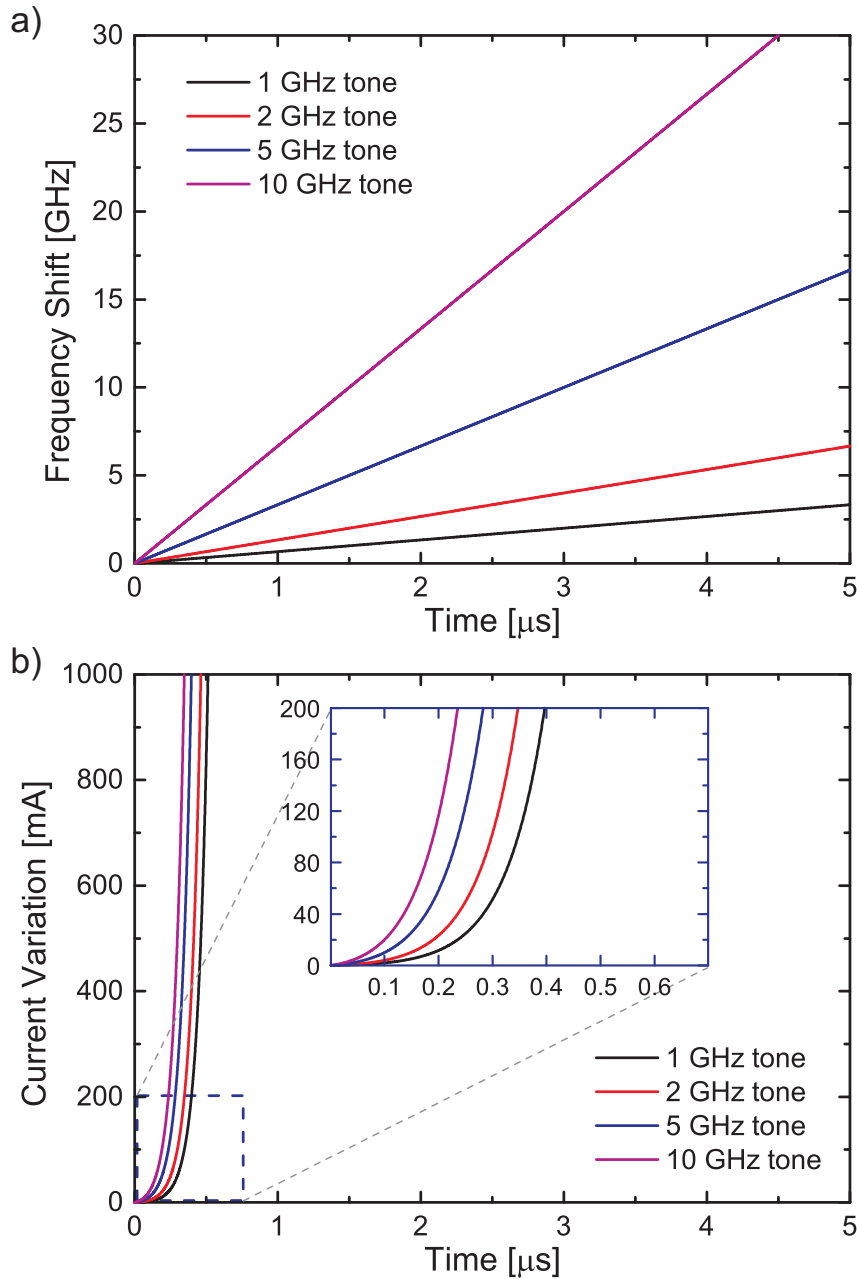


Figure 4.8: Simulation results of the obtained current inputs (b) required for the linear optical chirp outputs (a). As the self-heterodyne beating ( $\tau = 1.5\mu\text{s}$ ) of linear optical chirp signals originates microwave tones, four microwave tones were analysed: 1, 2, 5 and 10 GHz.

frequency. For instance, when a linear current variation is applied to the DFB-LD, the natural tendency of the optical frequency is to move toward the optical frequency correspondent to the instantaneous injected current according to Fig. 2.10, but in a slower pace than the current variation. Therefore, to keep up with the desired  $\nu(t)$ , a much higher current is required, as shown in Figs. 4.7 and 4.8.

Although not plotted in Figs. 4.7 and 4.8, the maximum simulated

current variations to achieve a parabolic and linear optical chirp reached the absurd values of  $2.5 \times 10^{29}$  and  $6.9 \times 10^{30}$  mA, respectively, what shows the physical limitation for a perfect parabolic and linear optical chirp. However, as the parameter  $a$  decreases, a more comfortable current is required. Thus, an investigation on the threshold case that allows a parabolic optical chirp with a physically possible injected current has been done. The result shows that a slow parabolic frequency chirp at a rate of 1 Hz/s can be achieved with a pulse duration of 3  $\mu$ s. This gives a bandwidth of 3  $\mu$ Hz, which is much narrower than the laser's linewidth, thus, could not be seen in an ESA equipment, and also, could not be used in radar systems.

As mentioned above, it is evident that attempts to force a desired  $\nu(t)$  would result in absurd injected currents that cannot be applied in a real DFB-LD. A different approach is henceforth taken to obtain the desired  $f_{RF}(t)$  at the photodetector. Instead of forcing a desired chirped output and go against the natural tendency of  $\nu(t)$ , a new simulation was set to predict  $f_{RF}(t)$  given a suitable  $i(t)$ .

Given the importance of NLFM waveforms for pulse compression in radar technologies as presented in section 2.1.4, the simulation was set in order to generate this type of microwave pulses: a sharper frequency change at the ends, and a more moderate change throughout the middle (see Fig. 2.8). In this way,  $\nu(t)$  should be such that  $f_{RF}(t)$  presents apodized like pulses (or NLFM pulses).

As shown in Fig. 4.4, a step input current results in an abrupt blue-shift followed by an exponential red-shift. This exponential decay can be used to generate the sharp frequency change at the leading edge of the apodized microwave pulse. The moderate change throughout the middle of the pulse is obtained by an exponential growth of  $i(t)$ , which straightens the optical frequency exponential decay resultant from the step input current. For a sharp frequency change at the trailing edge,  $i(t)$  must then drop quickly, but avoiding an abrupt change that could cause a sharp red-shift event due to the carrier population effect.

A simulated current pulse with the aforementioned properties is shown in the top panel of Fig. 4.9. The middle panel shows the simulated output optical frequency variations with respect to 193844.604 GHz ( $\Delta\nu(t)$ ) after both paths of the interferometer. The simulated time delay  $\tau = 1.56 \mu$ s was selected according to the 308 m single mode fiber used in the experiments. The bottom panel shows the simulated optical frequency difference (optical beating) generated in the PD as a function of time, i.e.  $f_{RF}(t)$ .

It can be seen from Fig. 4.9 that a current modulation pulse with

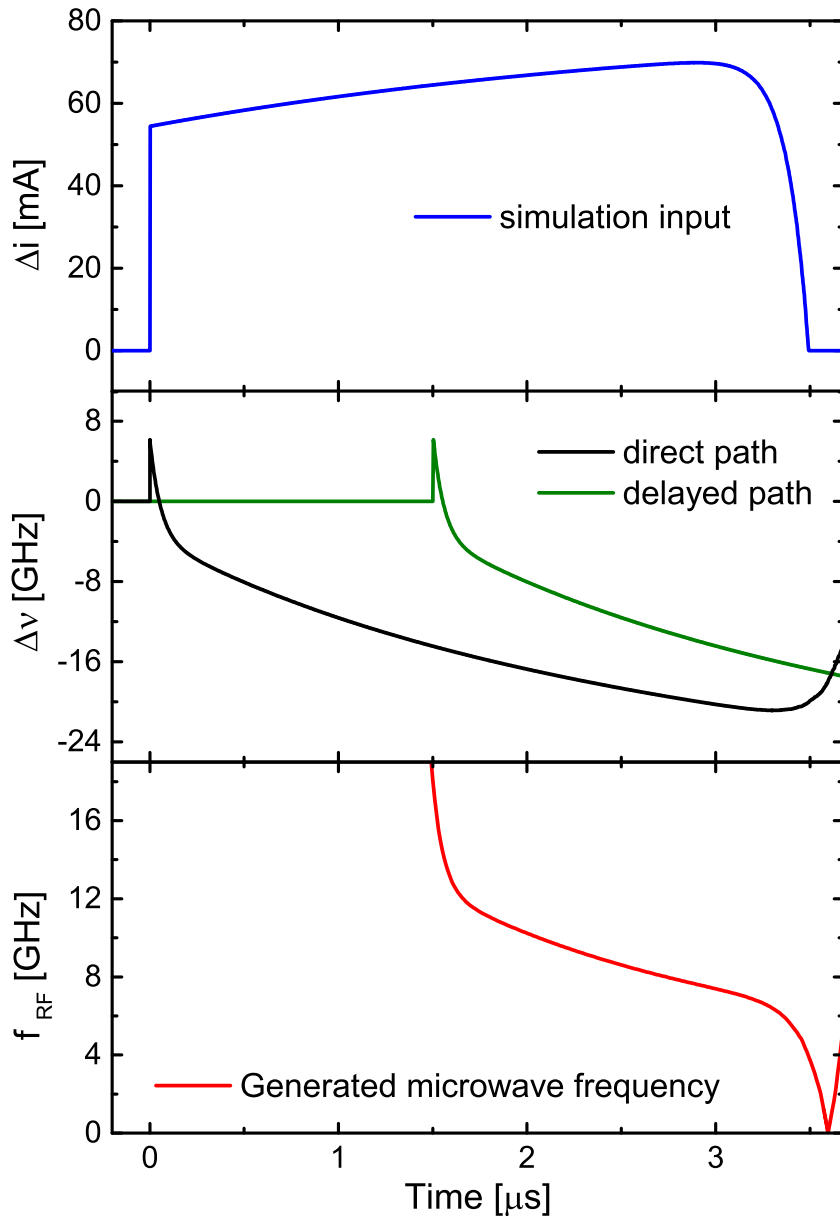


Figure 4.9: Simulation results for photonic generation of an apodized microwave pulse. First panel: input current variations above 20 mA. Second panel: output optical frequency in the two arms of an unbalanced interferometer. Third panel: frequency of the generated microwave.

maximum  $\Delta i$  of  $\sim 70$  mA above the 20 mA bias current would theoretically result in a microwave frequency band in the 0 - 18 GHz range. The apodized microwave pulse band is obtained by proper selection of  $W_C$ . According to the simulation result, by varying the maximum current input, the optical fiber delay and through proper chop time selection, an apodized microwave pulse can be generated at any desired radar band. In a real scenario, higher radar bands would be limited by the maximum allowed current in a DFB-LD and the PD bandwidth.

## 4.5

### Experimental results

The simulated input current ( $\Delta i$ ) shown in Fig. 4.9 was numerically transferred to AFG1, and thus translated into electric current  $i(t)$  for use in the self-heterodyning experimental setup. The input signal was also set to a repetition rate of 0.33 kHz to guarantee a relaxed state condition in the DFB-LD between two consecutive current pulses. Fig. 4.10 shows the direct measurement of the applied current from AFG1, done with the aid of a digital oscilloscope [60].

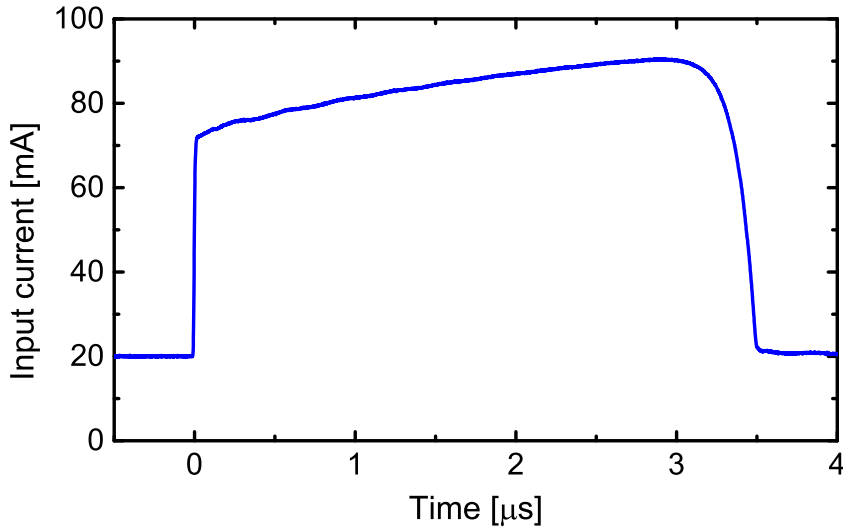


Figure 4.10: Measurement of the input modulation current with a repetition rate of 0.33 kHz.

The input current from Fig. 4.10 was used to modulate the DFB-LD in the experimental setup of Fig. 4.1. At this point, it is necessary to measure the instantaneous frequency time-dependence of the generated microwave in order to verify that an NLFM microwave pulse was obtained.

In order to measure  $f_{RF}(t)$ , the time-resolved optical spectroscopy concept was performed, but in the electrical domain by using the ESA. Particularly, as NLFM pulses have fast frequency variations at the edges, the smallest  $W_C$  of 40 ns will produce a larger bandwidth at the edges (extreme values of  $\delta$ ), and a narrower bandwidth at the center. Therefore, the extreme frequency values of the bandwidth were considered for an appropriate measure at the pulse edges, while the central frequency was considered for frequencies at the center of the pulse. In this way, the experimental parameters were set as follows: chop time  $W_C = 40$  ns and chop time delay  $\delta$  varying from = 1.55 to 3.51  $\mu$ s, thus covering a range of 2  $\mu$ s. For generating the full microwave band,  $\delta$  should remain fixed at 1.55  $\mu$ s while  $W_C$  must be kept at 2  $\mu$ s. The power

spectrum of the full band generated microwave displayed in the ESA screen is presented in Fig. 4.11a. Both the measured and the simulated  $f_{RF}(t)$  are presented in Fig. 4.11b.

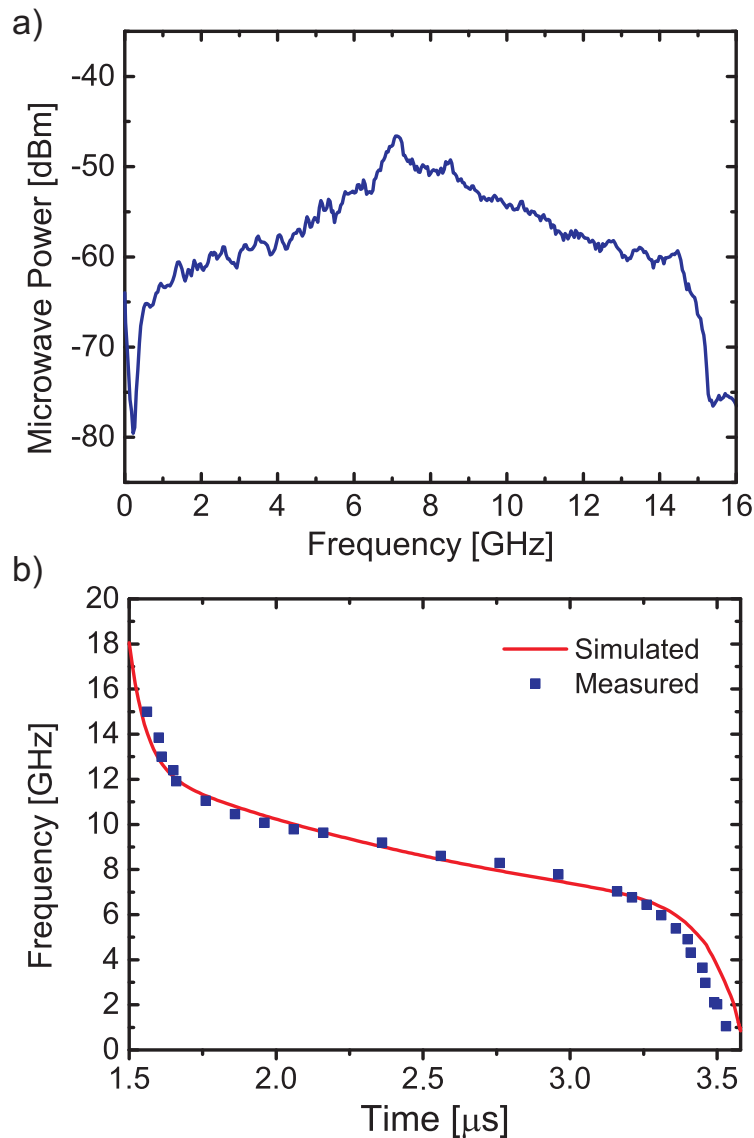


Figure 4.11: Photonic generation of NLFM microwave pulses: (a) Microwave power spectrum; (b) Comparison between the simulated and measured time dependent frequency  $f_{RF}(t)$  of NLFM microwave pulses.

A remarkable agreement between the experimental and simulated curves is observed in Fig. 4.11b, which confirms the effectiveness of the simulation tool. The experimental RF band obtained encompasses the L, S, C, X and part of the Ku radar bands (1 – 15 GHz), the linearly chirped part within the C and X bands. A large TBWP of 28000 ( $2 \mu\text{s} \times 14 \text{ GHz}$ ) was obtained. Moreover, even using an EDFA for power equalization, the power spectrum density shown in Fig. 4.11a is not flat. This effect is expected because more time is spent in the central frequencies in comparison with those at the edges. This

phenomenon was explained in section 2.1.4, and Fig. 2.8 shows the theoretical spectral density of NLFM pulses. Despite the chirp growth behaviour (upchirp or downchirp), great resemblance can be perceived between the theoretical and experimentally obtained NLFM pulses.

## 5 Conclusions

Two experiments were presented in this work. The first has shown the use of self-heterodyning technique to generate highly linear wide bandwidth microwave chirped pulses. Despite the use of low-frequency electronics in the laser control and slow DFB-LD chirp due to thermal effects, a 2–25.2 GHz bandwidth was achieved with 2.95  $\mu$ s time duration pulses, leading to a TBWP of 68400. The generated pulses cover virtually the microwave radar bands from S to K.

Spectrum analysis showed HD of at least -30 dB throughout the entire band, and the electrical power flatness, along the microwave pulses, was better than  $\pm 3$  dB. Furthermore, the chirped waveforms were transmitted along 25 and 41 km length standard optical fiber links without significant distortions. This transmission is potentially useful when the antenna must be placed kilometers detached from the optoelectronic equipment's.

A simple theoretical model showing that the output BW and TBWP can be optimized for fiber delays of  $\tau = W/2$  and  $\tau = W/3$ , respectively, was experimentally checked with good accuracy. In addition, by increasing the current amplitude under delay-optimized condition, a new BW of 2.0 - 28.4 GHz was obtained, resulting in a TBWP of  $\sim 74000$ , although without chirp linearization. To the authors' best knowledge, this is the highest value ever reported using the present technique. A quick evaluation of the pulse temporal compression leads to a theoretical spatial resolution of about 5.7 mm.

The pulse width, central frequency, spectral bandwidth and the chirp's time dependence of the microwave pulses can be easily controlled by adjusting the laser control parameters. Moreover, the simplicity of the technique allows to remotely tune any frequency band by modifying only two parameters:  $W_C$  and  $\delta$ . In fact, since the AFG1 is General Purpose Interface Bus (GPIB) configurable, the desired bandwidth can be readily selected.

The applied parabolic-shaped voltage stimulus on the laser diode was ineffective in achieving linear chirped output waveform, confirming that the chirp parameter  $\alpha_{ch}$  presents current dependence. However, by means of a simple polynomial adjustment, i.e. by adding a cubic term in the original input parabolic-shaped voltage waveform, highly linear chirped pulses could

be achieved.

It is important to note that the third order correction term does not produce a perfectly linear chirp. The difficulty in achieving a perfect linear chirp is studied in the second experiment, which has shown, for the first time, a method for generation of virtually arbitrarily chirped microwave pulses through self-heterodyning technique. The laser source was modelled as an LTI system, which was done with the aid of Time-Resolved Optical Spectroscopy. With knowledge of the transfer function that characterizes the LTI system, and using a numerical simulation, the necessary current input was calculated for a desired chirped microwave output. However, due to the slow time constants of the DFB-LD, perfect linear chirps demand extremely high currents, what limits the arbitrariness of the chirp of the generated RF microwave for real lasers.

Nevertheless, the prediction of the frequency time-dependence of the generated RF microwave for any given input could be determined. This enabled an analysis of the behaviour of  $f_{RF}(t)$  for several input current waveforms, through which an NLFM microwave ranging from 1–15 GHz, encompassing the L, S, C, X and part of the Ku radar bands, was simulated and experimentally generated. The simulation has shown a remarkable agreement with the measured results, and a large TBWP of 28000 was obtained.

## Bibliography

- [1] M. A. Richards, *Fundamentals of Radar Signal Processing*. McGraw-Hill, 2005.
- [2] R. Ghavamirad, H. Babashah, and M. A. Sebt, "Nonlinear FM waveform design to reduction of sidelobe level in autocorrelation function," in *2017 Iranian Conference on Electrical Engineering (ICEE)*, May 2017, pp. 1973–1977.
- [3] N. Levanon and E. Mozeson, *Radar Signals*. John Wiley and Sons, 2004.
- [4] G. P. Agrawal, *Fiber-Optic Communications Systems*, ser. Wiley Series in Microwave and Optical Engineering. John Wiley and Sons, 2002.
- [5] B. E. A. Saleh and M. C. Teich, *Fundamentals of Photonics*, ser. Wiley Series in Pure and Applied Optics. John Wiley and Sons, 2007.
- [6] W. D. Boyer, "Continuous wave radar," Patent US3 155 972A, 11 03, 1964. [Online]. Available: <https://patents.google.com/patent/US3155972A/en>
- [7] C. Wolff. (1997) Radar basics. [Online]. Available: <http://www.radartutorial.eu/index.en.html>
- [8] J. Coales, H. Calpine, and D. Watson, "Naval fire-control radar," *Journal of the Institution of Electrical Engineers - Part IIIA: Radiolocation*, vol. 93, no. 2, pp. 349–379, December 1946.
- [9] *2009 Pioneer Award*. IEEE Trans. Aerosp. Electron. Syst., 2010, 46, 2139–2141.
- [10] I. Intyas, R. Hasanah, M. R. Hidayat, B. Hasanah, A. B. Suskmono, and A. Munir, "Improvement of radar performance using LFM pulse compression technique," Aug 2015, pp. 302–307.
- [11] L. E. Herrera, R. M. Ribeiro, V. Jabulka, P. T. Braga, and J. P. von der Weid, "Photonic generation and transmission of linearly chirped microwave pulses with high TBWP by self-heterodyne technique," *Journal of Lightwave Technology*, pp. 1–1, 2018.

- [12] G. Galati, G. Pavan, and F. De Palo, "Chirp signals and noisy waveforms for solid-state surveillance radars," *Aerospace*, vol. 4, no. 1, pp. 349–379, 2017. [Online]. Available: <http://www.mdpi.com/2226-4310/4/1/15>
- [13] E. D. Witte and H. D. Griffiths, "Improved ultra-low range sidelobe pulse compression waveform design," *Electronics Letters*, vol. 40, no. 22, pp. 1448–1450, Oct 2004.
- [14] T. K. Sarkar and R. D. Brown, "An ultra-low sidelobe pulse compression technique for high performance radar systems," in *Proceedings of the 1997 IEEE National Radar Conference*, May 1997, pp. 111–114.
- [15] S. P. Lohmeier, "Adaptive FIR filtering of range sidelobes for air and spaceborne rain mapping," in *IEEE International Geoscience and Remote Sensing Symposium*, vol. 3, June 2002, pp. 1801–1803 vol.3.
- [16] M. H. Ackroyd and F. Ghani, "Optimum mismatched filters for sidelobe suppression," *IEEE Transactions on Aerospace and Electronic Systems*, vol. AES-9, no. 2, pp. 214–218, March 1973.
- [17] M. Rowe, P. Michler, J. Gutowski, V. Kummler, A. Lell, and V. Harle, "Influence of the carrier density on the optical gain and refractive index change in InGaN laser structures," vol. 200, pp. 135–138, 11 2003.
- [18] G. Kovacs and T. Berceci, "A novel approach for microwave signal generation utilizing DFB-laser wavelength chirp," in *2007 European Microwave Integrated Circuit Conference*, Oct 2007, pp. 528–531.
- [19] *Mitsubishi FU-68PDF-5*, ILX Lightwave Corporation. [Online]. Available: [http://www.glztech.com/product\\_datasheet/OSC-LDPM-C-009C\\_pdf1.pdf](http://www.glztech.com/product_datasheet/OSC-LDPM-C-009C_pdf1.pdf)
- [20] *3040 Temperature Controller*, Newport. [Online]. Available: <ftp://download.newport.com/Photonics/Laser%20Diode%20Control%20Instruments/Manuals/3040%20Temperature%20Controller%20Manual.pdf>
- [21] *505 Laser Diode Driver*, Newport. [Online]. Available: <http://www.spectroscopic.com/Newport/505.pdf>
- [22] *Optical Spectrum Analyzer MS9740A*, Anritsu. [Online]. Available: <https://www.anritsu.com/en-US/test-measurement/products/ms9740a>
- [23] J. M. Wiesenfeld, R. S. Tucker, and P. M. Downey, "Picosecond measurement of chirp in gain-switched, single-mode injection lasers," *Applied Physics Letters*, vol. 51, 8 1987.

- [24] F. Koyama and Y. Suematsu, "Analysis of dynamic spectral width of dynamic-single-mode (DSM) lasers and related transmission bandwidth of single-mode fibers," *IEEE Journal of Quantum Electronics*, vol. 21, no. 4, pp. 292–297, April 1985.
- [25] K. Kishino, S. Aoki, and Y. Suematsu, "Wavelength variation of 1.6  $\mu\text{m}$  wavelength buried heterostructure GaInAsP/InP lasers due to direct modulation," vol. 18, pp. 343 – 351, 04 1982.
- [26] S. Kobayashi, Y. Yamamoto, M. Ito, and T. Kimura, "Direct frequency modulation in AlGaAs semiconductor lasers," *IEEE Journal of Quantum Electronics*, vol. 18, no. 4, pp. 582–595, Apr 1982.
- [27] R. A. Linke, "Transient chirping in single-frequency lasers: lightwave systems consequences," *Electronics Letters*, vol. 20, no. 11, pp. 472–474, May 1984.
- [28] K. Iwashita, K. Nakagawa, Y. Nakano, and Y. Suzuki, "Chirp pulse transmission through a single-mode fibre," *Electronics Letters*, vol. 18, no. 20, pp. 873–874, September 1982.
- [29] A. M. Kawalec, "SAW dispersive delay lines in radar signal processing," in *Proceedings International Radar Conference*, May 1995, pp. 732–736.
- [30] S. M. B. A. W. Doerry, J. M. Andrews, "Digital synthesis of linear-FM chirp waveforms: comments on performance and enhancements," vol. 9077, 2014, pp. 9077 – 9077 – 12. [Online]. Available: <https://doi.org/10.1117/12.2048978>
- [31] J. Yao, "Photonic generation of microwave arbitrary waveforms," in *16th Opto-Electronics and Communications Conference*, July 2011, pp. 356–357.
- [32] Y. Li, A. Dezfouliyan, and A. M. Weiner, "Photonic synthesis of spread spectrum radio frequency waveforms with arbitrarily long time apertures," *Journal of Lightwave Technology*, vol. 32, no. 20, pp. 3580–3587, Oct 2014.
- [33] P. Zhou, F. Zhang, Q. Guo, and S. Pan, "Linearly chirped microwave waveform generation with large time-bandwidth product by optically injected semiconductor laser," *Opt. Express*, vol. 24, no. 16, pp. 18460–18467, Aug 2016. [Online]. Available: <http://www.opticsexpress.org/abstract.cfm?URI=oe-24-16-18460>
- [34] D. Novak, R. B. Waterhouse, A. Nirmalathas, C. Lim, P. A. Gamage, T. R. Clark, M. L. Dennis, and J. A. Nanzer, "Radio-Over-Fiber Technologies for

- Emerging Wireless Systems," *IEEE Journal of Quantum Electronics*, vol. 52, no. 1, pp. 1–11, Jan 2016.
- [35] A. Rashidinejad, Y. Li, and A. M. Weiner, "Recent Advances in Programmable Photonic-Assisted Ultrabroadband Radio-Frequency Arbitrary Waveform Generation," *IEEE Journal of Quantum Electronics*, vol. 52, no. 1, pp. 1–17, Jan 2016.
- [36] J. Capmany, G. Li, C. Lim, and J. Yao, "Microwave photonics: Current challenges towards widespread application," *Opt. Express*, vol. 21, no. 19, pp. 22 862–22 867, Sep 2013. [Online]. Available: <http://www.opticsexpress.org/abstract.cfm?URI=oe-21-19-22862>
- [37] M. A. Bernacil, S. O'Connor, B. Maher, A. Dekelaita, and D. Derickson, "Microwave signal generation using self-heterodyning of a fast wavelength switching SG-DBR laser," in *2008 IEEE MTT-S International Microwave Symposium Digest*, June 2008, pp. 603–606.
- [38] J. D. McKinney, D. E. Leaird, and A. M. Weiner, "Millimeter-wave arbitrary waveform generation with a direct space-to-time pulse shaper," *Opt. Lett.*, vol. 27, no. 15, pp. 1345–1347, Aug 2002. [Online]. Available: <http://ol.osa.org/abstract.cfm?URI=ol-27-15-1345>
- [39] C. Wang and J. Yao, "Photonic generation of chirped microwave pulses using superimposed chirped fiber bragg gratings," *IEEE Photonics Technology Letters*, vol. 20, no. 11, pp. 882–884, June 2008.
- [40] J. J. O'Reilly, P. M. Lane, R. Heidemann, and R. Hofstetter, "Optical generation of very narrow linewidth millimetre wave signals," *Electronics Letters*, vol. 28, no. 25, pp. 2309–2311, Dec 1992.
- [41] Y. Dai and J. Yao, "Nonuniformly spaced photonic microwave delay-line filters and applications," *IEEE Transactions on Microwave Theory and Techniques*, vol. 58, no. 11, pp. 3279–3289, Nov 2010.
- [42] X. Chen, Z. Deng, and J. Yao, "Photonic generation of microwave signal using a dual-wavelength single-longitudinal-mode fiber ring laser," *IEEE Transactions on Microwave Theory and Techniques*, vol. 54, no. 2, pp. 804–809, Feb 2006.
- [43] T. L. Koch and J. E. Bowers, "Nature of wavelength chirping in directly modulated semiconductor lasers," *Electronics Letters*, vol. 20, no. 25, pp. 1038–1040, December 1984.

- [44] O. L. Coutinho, J. Zhang, and J. Yao, "Photonic generation of a linearly chirped microwave waveform with a large time-bandwidth product based on self-heterodyne technique," in *2015 International Topical Meeting on Microwave Photonics (MWP)*, Oct 2015, pp. 1–4.
- [45] L. Goldberg, J. F. Weller, and H. F. Taylor, "Microwave signal generation using an optical self-heterodyne technique," *Electronics Letters*, vol. 18, no. 8, pp. 317–319, April 1982.
- [46] L. E. Y. Herrera, R. M. Ribeiro, V. B. Jabulka, and J. P. von der Weid, "Optical generation and transmission of linearly chirped microwave pulses with high time-bandwidth product," in *Optical Fiber Communication Conference*. Optical Society of America, 2018, p. M1H.2. [Online]. Available: <http://www.osapublishing.org/abstract.cfm?URI=OFC-2018-M1H.2>
- [47] H. Deng, J. Zhang, X. Chen, and J. Yao, "Photonic Generation of a Phase-Coded Chirp Microwave Waveform With Increased TBWP," *IEEE Photonics Technology Letters*, vol. 29, no. 17, pp. 1420–1423, Sept 2017.
- [48] W. V. Sorin and D. M. Baney, *High resolution optical frequency analysis*, in *Fiber Optic Test and Measurement* by D. Derickson, Upper Saddle River, New Jersey, USA, Prentice-Hall, Inc. 1998, Ch. 5, pp. 169-219.
- [49] R. Devlen and E. Schiff, "Optically detected photocarrier transport in amorphous silicon: a review," *Journal of Non-Crystalline Solids*, vol. 141, pp. 106 – 118, 1992. [Online]. Available: <http://www.sciencedirect.com/science/article/pii/S0022309305805241>
- [50] S. Diez, C. Schmidt, R. Ludwig, H. G. Weber, K. Obermann, S. Kindt, I. Koltchanov, and K. Petermann, "Four-wave mixing in semiconductor optical amplifiers for frequency conversion and fast optical switching," *IEEE Journal of Selected Topics in Quantum Electronics*, vol. 3, no. 5, pp. 1131–1145, Oct 1997.
- [51] *Arbitrary/Function Generators-3000 series*, Tektronix. [Online]. Available: [http://www.testequipmentdepot.com/tektronix/pdf/afg3000c-series\\_datasheet.pdf](http://www.testequipmentdepot.com/tektronix/pdf/afg3000c-series_datasheet.pdf)
- [52] *Erbium Doped Fiber Amplifier 1550nm*, Tuolima. [Online]. Available: <http://www.tuolima.com/uploads/edfa-1550.pdf>
- [53] *MS2668C Spectrum Analyzer*, Anritsu. [Online]. Available: <https://www.anritsu.com/en-US/test-measurement/products/MS2668C>

- [54] *DSC 30S Wide Bandwidth High Power Low Distortion PIN Diodes*, Discovery Semiconductors Inc. [Online]. Available: <http://chandra.berkeley.edu/~plambeck/CARMAdocs/LabIFbox/DSC50S>
- [55] *Semiconductor Optical Amplifier - SOA1013SXS*, Thorlabs. [Online]. Available: <https://www.thorlabs.com/thorproduct.cfm?partnumber=SOA1013SXS>
- [56] *MN9610B Programmable Optical Attenuator*, Anristu. [Online]. Available: <https://testmart.com/sp.cfm/OPTCOM/ANRI/MN9610B.html>
- [57] A. K. Rutkowski, "Measurement of microwave signals intrapulse parameters by means of ifm methods," in *MIKON 2008 - 17th International Conference on Microwaves, Radar and Wireless Communications*, May 2008, pp. 1–4.
- [58] P. Ghelfi, F. Laghezza, F. Scotti, D. Onori, and A. Bogoni, "Photonics for radars operating on multiple coherent bands," *Journal of Lightwave Technology*, vol. 34, no. 2, pp. 500–507, Jan 2016.
- [59] *AP2050A High Resolution Optical Spectrum Analyzer*, Apex. [Online]. Available: <http://www.apex-t.com/optical-spectrum-analyzer>
- [60] *Digital Phosphor Oscilloscope - DPO7354*, Tektronix. [Online]. Available: <https://www.tek.com/oscilloscope/dpo7000-digital-phosphor-oscilloscope>